Scholars' Mine

Doctoral Dissertations | Student Theses and Dissertations

Summer 2020

Characterization of neutron irradiated accident tolerant nuclear fuel cladding silicon carbide & radiation detector deadtime

Bader Almutairi

Recommended Citation

CHARACTERIZATION OF NEUTRON IRRADIATED ACCIDENT TOLERANT

NUCLEAR FUEL CLADDING SILICON CARBIDE & RADIATION DETECTOR

DEADTIME

by

BADER ALMUTAIRI

A DISSERTATION

Presented to the Faculty of the Graduate School of the

MISSOURI UNIVERSITY OF SCIENCE AND TECHNOLOGY

In Partial Fulfillment of the Requirements for the Degree

DOCTOR OF PHILOSOPHY

in

NUCLEAR ENGINEERING

2020

Approved by:

Shoaib Usman, Advisor
Syed Alam
Ayodeji B. Alajo
Cameron Goodwin
Carlos H. Castano
Xin Liu

PUBLICATION DISSERTATION OPTION

This dissertation has been prepared in the form of four papers for publication as follows:

Paper I: Pages 6-33 have been published to the Journal of Nuclear Engineering and Technology.

Paper II: Pages 34-71 have been accepted with minor revision in Nature Scientific Reports.

Paper III: Pages 72-101 have been submitted in Nature Scientific Reports.

Paper IV: Pages 102-148 under review in Nature Scientific Reports.

ABSTRACT

In part I, the pulse shape characteristics generated by a Geiger Muller (GM) detector and recorded by an oscilloscope manually, were investigated. The objective of part I was (1) to find a correlation between pulse shape and the operating voltage; and (2) to assess if pulse shape properties followed distinct patterns comparable to detector deadtime findings reported by a previous study. It was observed that (1) there is a strong correlation between pulse shape and operating voltage, and (2) pulse shape falls in three distinct regions similar to detector deadtime. Furthermore, parts II and III are companions and share the same experimental setup designed to simultaneously measure the GM detector's deadtime, and capture and record the generated pulses by an oscilloscope automatically. Four different pairs of radioactive sources (^{204}Tl, ^{137}Cs, ^{22}Na, ^{54}Mn) were used. For part II, it was observed that deadtime dependence on operating voltage followed a distinct pattern while using ^{204}Tl, ^{137}Cs, ^{22}Na except for ^{54}Mn. For part III, it was found that there is a strong correlation between deadtime behavior and several pulse shape properties. In addition to part I-III, part IV focused on the characterization of accident tolerant fuel cladding SiC for high burnup SMR core. First, reactor physics modeling for various accident tolerant fuel claddings was performed. It was found that SiC outperforms all other cladding candidates in terms of discharge burnup. Second, an experimental setup was designed to characterize weight loss and mechanical strength of SiC by examining the effects of neutron-irradiation in harsh environments. It was observed that (1) irradiated samples were more prone to material weight loss at higher temperatures, and (2) mechanical strength for control, non-irradiated, and irradiated samples were comparable.

ACKNOWLEDGMENTS

With boundless love, I would like to express my heartful gratitude to all the people who helped and supported me during the five years journey for earning a Ph.D. in nuclear engineering. I would like to express my deepest gratitude to my advisor, Dr. Usman Shoaib, and co-advisor, Dr. Syed Alam, for their valuable support, assistance, and encouragement during my graduate study. I would like to express sincere gratitude to the rest of my advisory committee members, Dr. Ayodeji B. Alajo, Dr. Carlos H. Castano, Dr. Xin Liu, and Dr. Cameron Goodwin, for their endorsement, commitment, and invaluable support to accomplish this thesis. I would like to extend my appreciation to Dr. Safwan Jaradat and Dr. Tayfun Akyurek for their contributions. I am most grateful for the staff, Mr. Paul Martin, Mr. Matthew Marrapese, Mr. Jeff Davis, Mr. Bernard Sirr, Mr. Austin Olsen, Ms. Sophia Lenihan, Mr. Sangho Nam, and Ms. Robin Wheeler, at Rhode Island Nuclear Science Center (RINSC) for their generous help, assistance, and guidance to allow me to get hands-on experience in nuclear research reactor operations and accomplish the SiC cladding project. I am thankful to my colleagues, Dr. Mokhtar Fal, Dr. Abdulaleem Bugis, Dr. Galib Shikaat, and my best friends (Dr. Wael Alrawashdeh, and Mr. Federico Rafanelli). I would like to express sincerest thanks to my coworkers and colleagues in my beloved country of Kuwait: Dr. Naji Almutairi, Dr. Sameer Alzenki, Mr. Mohammed Waheed, Mr. Ahmad Shehab, Mr. Ahmad Alenzi, Dr. Lena Davidsson and Mrs. Mona Alfilchawi. I am incredibly grateful to my family (my wife and three children). Also, I am deeply indebted to my mother for the colossal sacrifices she made during the entire period of my education. I strongly believe that my words of gratitude toward her would not do her enough justice. Simply put, I am fortunate to have a great mother.

TABLE OF CONTENTS

SECTION

LIST OF ILLUSTRATIONS

PAPER IV

LIST OF TABLES

1. INTRODUCTION

1.1. GM DETECTOR AND DEADTIME

Detector deadtime phenomenon has been an interest in the nuclear scientific community for decades. After Geiger and Mueller (GM) introduced the GM detector in 1928, and since then, the GM counter has been widely used in radiation measurement applications due to its simple, ease of operation, inexpensive design. The GM counter operates on the gas multiplication principle [1]. An initial radiation event taking place within the detector creates positive ion pairs and electrons. Applying a high voltage on the detector, electrons are accelerated towards the anode. In contrast, positive ions are accelerated towards the cathode if sufficient kinetic energy gained by the electron leads to the creation of secondary ionization, which leads to the creation of secondary and tertiary ionizations, which ultimately leads to the creation of Townsend avalanche [1].

Under the proper conditions, this avalanche triggers another avalanche leading to a self-propagating chain reaction enveloping the entire anode wire until the avalanche reaches a maximum size. The chain reaction is terminated when the electron strikes the anode wire, it creates a current. This current produces a pulse which is ultimately processed and counted by the pulse processing electronics. Because of the GM counter's underlying principle, the pulses produced by a GM counter are generally believed to have the same size and shape.

For radiation events to be counted as independent events, there has to be a minimum separation time between two radiation incidents. The minimum separation time is known as deadtime, and if any radiation incident takes place before the deadtime lapses, the event will be lost [2]. For any detector system, deadtime depends on the operating conditions,

pulse processing electronics, and its design [3]. Generally, the contributing factors to the deadtime of any detector system can be divided into (a) internal losses within the detector, and (b) count losses from the pulse processing circuitry [4]. In the case of a GM detector, the major contributor of deadtime originates from the processes with the detector itself.

Two idealized models are traditionally used in the industry and academics. These ideal models are known as paralyzing and non-paralyzing models introduced by Feller and Evans [5, 6]. Further research into the deadtime phenomenon resulted in a generalized model introduced by Mueller [7, 8]. A hybrid deadtime model was later introduced by Albert and Nelson [9] and later modified by Lee and Gardner [10] by combining the fundamentals of idealized models. A recent modification of the hybrid model was introduced by Patil and Usman [4] by introducing a paralysis factor into the mathematical expression.

All previous efforts were lacking any phenomenological explanation of deadtime. As a part of this dissertation, a detailed simultaneous observation of detector deadtime and various pulse shape characteristics were made. It was concluded that the common belief that all pulse generated in a GM counter as of the same size and shape is not correct. Moreover, a phenomenological basis of deadtime for a GM counter was developed and tested against the observation made on the pulse shape properties. Results showed that there are three distinct regions of detector deadtime for GM counter depending on the operating voltage. As a result of this experimental campaign three journal articles are produced in additional to 2 conference papers.

Further details are provided in Papers (I, II, III). The code for deadtime modeling using MATLAB in Paper (III) is also provided in Appendix A.

1.2. ACCIDENT TOLERANT FUEL CLADDING: SILICONE CARBIDE

There has been an increased interest in accident tolerant fuel (ATF) cladding concepts after the 2011 Fukushima Daiichi disaster. Since then, much research & development programs have been launched to find a potential ATF cladding to enhance the safety of 4th-generation nuclear reactors as well as to replace the traditional zircaloy cladding. Due to the favorable characteristics of silicon carbide (SiC), such as its low corrosion rate, SiC has been proposed as a potential ATF cladding [11-13]. The low corrosion rate of SiC would make it tolerate high fuel burnups. Therefore, it will enhance uranium utilization. It can also enhance the safety of Light Water Reactors (LWR) and possibly increase its power level.

Since 1950s, zirconium-based (Zr) alloys have been chosen as fuel cladding in LWRs because of Zr's lower neutron absorption cross-section compared with stainless steel [14-16]. Since then, the nuclear industry adopted Zr-based alloys as the cladding of choice in LWRs. Nevertheless, zirconium alloys at high temperatures in water shows accelerated material degradation due to its high corrosion rate. In fact, at high temperatures, the self-accelerating exothermic steam reaction of zirconium ultimately resulted in hydrogen production which led to hydrogen explosions and failure of three containment buildings in the Fukushima nuclear disaster [17-19]. After the accident, the nuclear industry launched serious efforts into finding an alternative ATF and cladding which could tolerate severe accident conditions.

SiC has several superior characteristics over zirconium alloys such as high melting point, high strength at elevated temperatures, heat transfer resistance, lower neutron absorption cross-section, and low corrosion rate. Due to these characteristics, SiC

demonstrates less susceptibility to hydrogen embrittlement and improved corrosion resistance [17-19, 20-22].

Furthermore, due to the added heat transfer resistance of SiC, nuclear fuel temperature can be higher. Along with the fact that Zr-based alloys cannot tolerate high temperatures (>800°C), this would make SiC a cladding material of choice for high burnup applications and Small Modular Reactor (SMR) cores [14, 20, 23-27].

Since Zr cladding can only survive the achievable burnup of 60–70 GWd/tonne [28-30] and long-life high burnup SMR cores would exceed 90 GWd/tonne, Zr cladding would not be a feasible choice [31, 32]. Hence, SiC serves as a potential ATF cladding for long-life high burnup SMR cores. As a part of this dissertation, SiC was examined for its properties in harsh reactor environment for possible application as cladding material for future reactors' fuel. An experimental study was performed to collect data on degradation of mechanical properties of SiC when exposed to steam, high temperature and nuclear radiation. In the initial phase of the research a burnup simulation was performed to predict the higher burnup limits that SiC could withstand. It was demonstrated that SiC has obvious advantage in this regard over other candidate cladding materials. Subsequently, SiC was simultaneously exposed to pure steam and heat to study the endurance of the material against corrosion. In nuclear reactor application, nuclear radiation is also a significant factor which can possibly accelerate the corrosion process. To examine the contribution of nuclear radiation, additional experiments were performed to examine the endurance of SiC under simultaneous exposure to radiation, steam, and heat. In addition to corrosion, mechanical strength post exposure was also testing using burst testing method.

Results obtained in the study are presented in 2 conference papers and 1 (Paper IV) journal article submitted for publication while additional manuscript(s) are under preparation. Paper (IV) provides the following: (1) neutronic analysis utilizing Monte Carlo N-Particle (MCNP), version 6.1; (2) experimental investigation for characterizing SiC in harsh reactor environments.

Furthermore, a sample code for the 2D subassembly lattice core used in MCNP simulations is provided in Appendix B. The output files from the MCNP simulations are substantial and extracting the results of interest is laborious and prone to human error, a Python code was developed to extract the final results of interest and the code is provided in Appendix C.

PAPER

I. VOLTAGE DEPENDENT PULSE SHAPE ANALYSIS OF GEIGER-MÜLLER COUNTER

B. Almutairi [a,c], T. Akyurek [b], and S. Usman[a]

[a] Department of Mining and Nuclear Engineering, Missouri University of Science & Technology, Rolla, MO, 65401, USA

[b] Department of Physics, Faculty of Art and Science, Marmara University, 34722, Kadikoy, Istanbul, TURKEY

[c] Environmental and Life Sciences Center, Kuwait Institute for Scientific Research, Kuwait City 13109, KUWAIT

ABSTRACT

Detailed pulse shape analysis of a Geiger-Müller counter is performed to understand the pulse shape dependence on operating voltage. New data is presented to demonstrate that not all pulses generated in a GM counter are identical. In fact, there is strong correlation between the operating voltage and the pulse shape. Similar to detector deadtime, pulse shapes fall in three distinct regions. For low voltage region, where deadtime was reported to reduce with increasing voltage, pulse generated in this region was observed to have a fixed pulse width with a variable tail. The pulse width and fall time of the tail was observed to be a function of applied voltage; exponentially reducing with increasing voltage with an exponent of negative 6E-04 and 2E-03, respectively. The second region showed a pulse without any significant tail. During this time, the detector deadtime was earlier reported to be at its minimum. The highest voltage region demonstrated a different deadtime mechanism where the second pulse was reduced in width. During this

time, the deadtime seemed to be increasing with increasing voltage. This data allows us to gain some unique insight into the phenomenon of GM detector deadtime not reported thus far. GM detector deadtime not reported thus far.

1. INTRODUCTION

Geiger-Mueller (GM) counter is one of the oldest radiation detectors which was introduced by Geiger and Müller in 1928 [1]. It is widely used in the measurement of radiation due to its inexpensive, simple, rugged design and ease of operation. The GM counter falls under the category of filled gas detectors. It operates on the principle of gas multiplication, i.e., electron and positive ion pairs are created from an initial radiation interaction. Due to high velocity of charged particles, secondary ionization events are produced. If the original ionizing event was caused by beta or alpha particles, then the fill gas is ionized directly; on the other hand, gamma and x-rays ionize the gas indirectly.

When a high voltage is applied to the detector, the electrons are accelerated towards the anode and the positive ions are accelerated towards the cathode due to the potential difference between the anode and cathode. The accelerated electron gains sufficient kinetic energy to produce secondary ionization. In additional to the secondary ionization a large number of atoms/molecules are left in the excited state leading to almost immediate de-excitation of these molecules which produce photons within visible or ultraviolet range. Interaction of these photons with the GM cathode wall or the gas itself causes secondary and tertiary ionizations, eventually leads to the formation of an avalanche of ion pairs commonly known as Townsend avalanche [2]. Under proper conditions, an avalanche can trigger a second avalanche, however, at a different position within the counter. On the

average, each avalanche can trigger at least another avalanche; thus, a self-propagating chain reaction that envelopes the entire anode's wire is induced. The velocity at which the avalanche propagates is approximately 2-4 cm/μs [2]. At higher values of the electric field, within a very short time an exponentially growing number of avalanches are formed. At certain point when the avalanche has reached the maximum size, the chain reaction terminates. Because of that, all pulses produced by the GM counter are generally believed to be of the same amplitude and shape. The GM counter is therefore limited in its application and cannot be used for radiation spectroscopy [2]. Data presented here makes this general assumption that all GM pulses are identical questionable.

Furthermore, the collected negative charges that were produced in the detector results in a pulse that lasts for a few microseconds. The time it takes to collect the charge depends on various factors: temperature, pressure, type of gas in the detector and the applied voltage; whereas the duration of the pulse depends on other factors: detector geometry, initial ionization location within the detector and the applied voltage [3]. The speed at which electrons or positive ions move from their point of origin can be accurately predicted by;

$$v = \frac{\mu . \varepsilon}{p} \tag{1}$$

where v is the drift velocity, μ is the charge mobility, ε is the strength of the electric field and p is the gas pressure. The mobility of free electrons in gases is much larger than that of positive ions; however, at higher electric field values, positive ion's drift velocity increases slowly with the electric field until it reaches a saturation velocity. Any further increase in the electric field will not affect the mobility, it will remain constant over wide ranges of electric field and gas pressure for both the negative electron and the positive ions.

Typical mobility for gases with a medium atomic number falls in the range of 1 to 1.5 x 10^{-4} m^2 atm/V. sec. and a typical drift velocity of 1 m/s occurs at 1 atm pressure and an electric field of 10^4 V/m as reported in the literature [2].

Nevertheless, free electrons and positive ions behave differently under applied voltage in that the former is more mobile than the latter by a factor of 1000 due to their low masses. Therefore, the collection time of free electrons is in the order of microseconds whereas the collection time of ions is in the order of milliseconds [3]. May et al. [4] proposed that the drift velocity of ions is inversely propisitional to temperature. Other studies have confirmed that ion mobility is not only altered by the applied voltage but also by temperature [3]. Preliminary work on temperature dependence of GM counter performance was reported by Akyurek and co-workers [3] and will not be discussed here.

Unlike free electrons which are collected rapidly at the anode, positive ions take a longer time to be collected at the cathode due to their low mobility. Under proper conditions, the positive ions form a sheath around the anode which results in a distortion of the electric field. If the sheath space of positive ions around the anode is not completely removed, any subsequent pulse generated will be reduced in amplitude. If the distorted field lingers and becomes stronger in magnitude, any following radiation interaction within the counter may result in an undetectable pulse [3, 5]. This undetectable pulse is lost in the GM counter. Since radiations incidents are random in nature, it follows that many undetectable pulses are lost in the counter. The undetectable pulses are a consequence of a phenomenon called deadtime which is yet another limitation of the GM counters.

1.1. THE DEADTIME PROBLEM

Deadtime is defined as the minimum time interval required for two consecutive radiation interactions in the counter to be detected as independent events. When two events occur within a short duration of time, less than the minimum time interval, the detector is unresponsive (dead); hence, the event is lost [6]. Detector deadtime had been an active area of research, several theoretical and experimental studies in the 30s and 40s have shown that the GM counter suffers from a long deadtime in the order of a few hundred microseconds to several milliseconds [7, 8]. For low counting rate applications, the GM counter has been extensively used where counting loss is rather easy to correct. On the other hand, for high counting rate applications, scintillation or solid-state detectors are better suited to perform the task because they suffer from a shorter deadtime [9]. It is for that reason that correction of deadtime of GM counters for high counting rate applications has been largely neglected until the late 1990s where the problem was reinvestigated by a group of researchers [10, 11]. In general, for various radiation detectors, deadtime phenomenon is significant at high intensity radiation applications such as in Positron Emission Tomography (PET) and spent fuel scanning. For gas-filled detectors, the investigation further continued to extend the useful counting rate range of GM counters [9, 12, 13].

It is important to recognize that deadtime is added at all stages of signal processing. As can be seen in Figure 1, radiation detection system consists of a detector that produces the initial pulse and passes it to a series of electronic pulse processing instruments; preamplifier, amplifier, single channel analyzer (SCA), and then either a multichannel channel analyzer (MCA) or a counter records the pulse [14]. In a typical radiation detection

system, there are two elements that contribute to total deadtime. First, the inherent deadtime produced by the detector's physical process and electric circuitry. Second, the characteristic deadtime contributed by each electronic instrument in the system. The deadtime from the modern electronics is negligible as compared to the long deadtime that GM detectors suffer from [14, 15]. Therefore, pulse processing deadtime can be neglected and only the inherent deadtime of the detector is sufficient for count rate correction consideration.
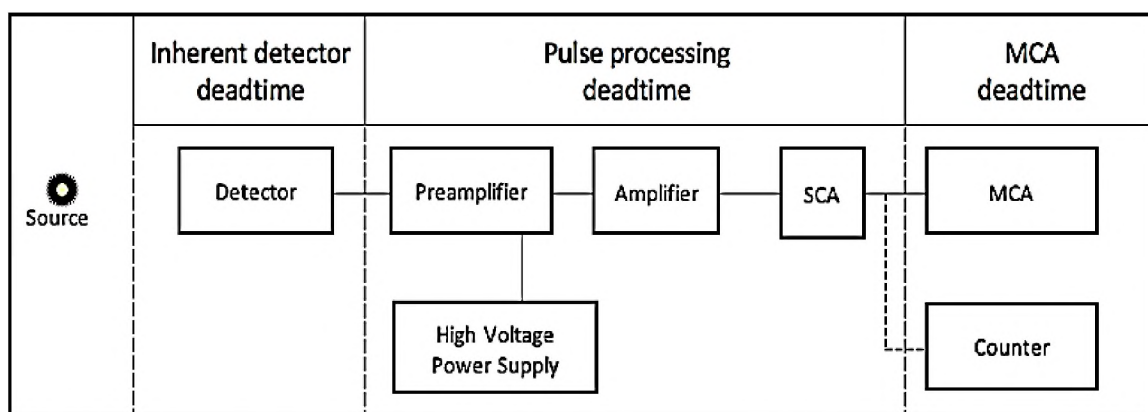
Figure 1. Radiation detection system in a laboratory.

1.2. DETECTOR DEADTIME MODELS

There are two widely used models for deadtime behavior in counting systems: the paralyzing model also known as the extending type; and the non-paralyzing model also refer to as non-extending type. These are ideal models and were first proposed by Feller [16] and Evans [17]. The paralyzing model assumes that after the first pulse is generated, any radiation incident that occurs during the resolving time (deadtime) will result in losing the subsequent pulse and it will reset the deadtime time; thus, the deadtime is extended. The system, therefore, suffers from continuous paralysis until at least a duration equal to

or greater than the deadtime lapses without the occurrence of any radiation event. The mathematical description derived by Feller and Evans for the paralyzing model is given by;

$$m = n. e^{-n.\tau} \qquad (2)$$

where, m is the observed or measured count rate, n is the true count rate and τ is the detector deadtime. The paralyzing model therefore sets the lower limit of deadtime behavior in counting systems. For the non-paralyzing model, any radiation event that occurs during the deadtime will be lost but the deadtime does not extend. In this model, the detector is assumed to be dead for a fixed time τ following each recorded radiation event. The mathematical description for the relation between observed and true counts for the non-paralyzing model is given by;

$$m = \frac{n}{1+n.\tau} \qquad (3)$$

where definitions of m, n and τ are the same as in Eq. (2). The non-paralyzing model therefore sets the upper limit of deadtime behavior for counting systems. These ideal models have been used extensively with success; however, in a limited fashion. In reality, true deadtime characteristics fall somewhere in between these extreme limits because real detectors do not follow these ideal models [6, 11, 14].

In 2000, Lee and Gardner [11] in an effort to extend the counting range of the GM detector proposed a hybrid model that combines both ideal models into one analytical expression. Mathematically, the hybrid model is given by;

$$m = \frac{n.e^{-n.\tau_p}}{1+n.\tau_{np}} \qquad (4)$$

where τ_p is the paralyzing deadtime and τ_{np} is the non-paralyzing deadtime. In this hybrid model, Lee and Gardner assumed that the non-paralyzing deadtime depends on the physical

characteristics of the detector itself. Based on this assumption, they proposed that paralyzing deadtime follows the non-paralyzing deadtime until a recorded amplitude is produced. However, they did not provide any justification for their assumption. In an effort to better represent the deadtime phenomenon, another hybrid model was proposed by Patil and Usman [12]. It was a based on single deadtime and a fixed paralysis factor f, mathematically;

$$m = \frac{n.e^{-n.\tau.f}}{1+n.\tau.(1-f)} \qquad (5)$$

where τ is the total deadtime and f is the paralysis factor. This fixed f is based on a probability that lies between 0 and 1. If the f is 1, then the hybrid model reduces to the ideal paralyzing model, while if f is 0, then the hybrid model reduces to the ideal non-paralyzing model. The hybrid models have successfully extended the useful counting range of the GM detector but only in a limited fashion. None of the models mentioned above have a phenomenological explanation of the deadtime; they are a mere mathematical convenience.

Recently, Usman and co-workers [18] demonstrated dependence of Geiger-Müller counter's deadtime on operating conditions. Their phenomenological model is based on a large amount of data on deadtime and pulse shape properties for GM counter at varying operating voltages reported by Akyurek et al. [3]. The data demonstrate three different regions of detector deadtime with varying operating voltages, as shown in Figure 2. In the low voltage deadtime region, the pulse width and tail duration were monotonically decreasing with increasing voltage. The occurrence of long exponentially decaying tail at the end of the pulse is believed to be due to the existence of some stray charge carriers in areas of weak potential. Those stray charge carriers take a longer time to be fully collected

by the cathode due to the existence of space charge. If another radiation event takes place during this period, it will be lost; however, the system may or may not get paralyzed. Hence, paralysis depends on physical location of the second radiation event within the counter in relation to the stray charge. Since the exact location of the second radiation event within the counter is a random process and cannot be determined, a stochastic approach would be needed. It was therefore concluded that the paralysis factor, should be an exponentially decreasing function of the applied voltage between the time of onset of the tail and the occurrence of the second event, unlike the fixed value proposed by Patil and Usman [12].

In the plateau deadtime region (middle region), it was observed that there is a fixed deadtime independent of the applied voltage; hence, the GM counter behaves as a non-paralyzing detector and Eq. (3) can be used for that entire region. In the high voltage deadtime region, the occurrence of high concentrations of positive ions around the anode results in reduced electric field further which results in a weak second pulse. Because of the presence of higher space charge at higher voltages, longer deadtime durations were observed as experimental data from Akyurek et al. [3] confirmed. Therefore, GM counter in this region behaves as a non-paralyzing detector with deadtime monotonically increasing with increasing voltage. It reinforces the assumption that the GM counter is non-paralyzing in nature as previous studies have suggested [3, 11, 12].

Akyurek et al. [3] have shown that GM's deadtime phenomenon is dependent not only on applied voltages but also on operating temperatures and fatigues which ultimately result in alteration of the pulse shape properties. It is therefore concluded that a single deadtime model is not adequate for any detector under all operating conditions, and a

careful selection of deadtime model under certain operating conditions is essential for the correction of observed count rates.
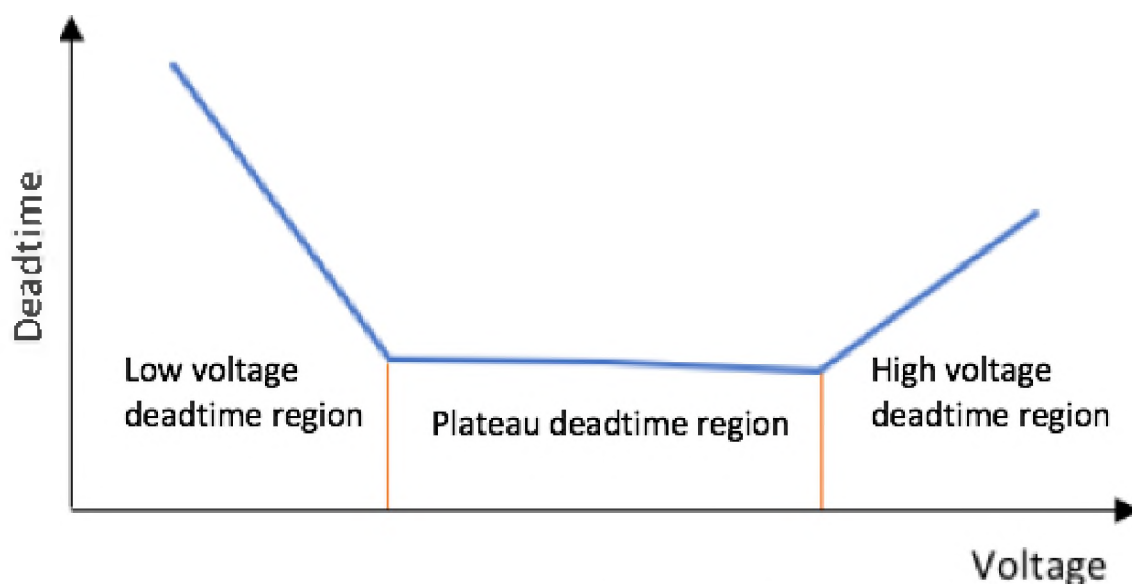
Figure 2. Detector deadtime regions with voltage dependence.

Current study present additional data on GM-counter deadtime and pulse shape for a wide range of operating voltages using ^{60}Co and ^{137}Cs sources. Raw data are provided, and the analysis of result is shared with discussion on the variation of deadtime with operating voltage and pulse shape.

2. MATERIALS AND METHOD

The experimental set-up included: two sources, GM counter, preamplifier, high-voltage power supply, and an oscilloscope. ^{60}Co and ^{137}Cs were both used separately. Both

sources were produced in February 2013 as 1 μCi strength and distributed by Spectrum Techniques, LLC [19].

The GM counter (Ludlum, model 133-2) was used for detecting radiation incidents [20]. Ludlum GM is a halogen quenched, stainless steel, windowless type detector which is more sensitive to gamma and x-ray radiations; alpha and beta particles are mostly blocked by the detector's thick walls. The typical deadtime value of this detector is reported by the manufacturer to fall in 50 μs range. A charge-sensitive preamplifier (Ortec, model 142A) was connected to the connector series "C" of the GM counter through a coaxial cable. The preamplifier's main function is to extract signals from the detector without degrading the intrinsic signal-to-noise ratio; therefore, caution was exercised to ensure extracting low signal-to-noise ratio by placing the preamplifier as close to the detector as possible [21]. For high-voltage power supply, Ortec, model 556 was used and connected to the bias input of the preamplifier through a coaxial cable [22]. The Ortec 556 model was housed in a nuclear instrumentation module (NIM) and it provides noise-free, very stable high voltage necessary for proper operation of the GM counter. The input voltage can be controlled from an adjustable ± 10 to ± 3000 Volts knob. The input power is connected directly from the AC line. Finally, Oscilloscope (Tektronix, model DPO3032) was connected to the output of the preamplifier through a coaxial cable [23]. The oscilloscope was connected to the PC through a USB cable and the oscilloscope's screen image of pulses was saved directly to the PC. The DPO3032 has an automatic measurements mode and it was utilized to acquire and record train of pulses. The automatic measurements mode is divided into two categories: time and amplitude measurements. Table 1 lists the illustration of various pulse shapes and pulse characteristics definitions observed during the

experiments. Pulse characteristics were recorded using automatic measurement capabilities

of the oscilloscope.

Table 1. Each automatic measurement illustration of pulse definition. The rise and fall
time along with the pulse width are time measurements while others are amplitude in the
units of volts.
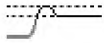
#	Illustration	Measurement	Definition
1		Rise Time	It is the time required for the leading edge to rise from the low reference value (10%) to the high reference value (90%) of the final value.
2		Fall Time	It is the time required for the falling edge to fall from the high reference value (90%) to the low reference value (10%) of the final value. The fall time is known as tail of the pulse.
3		Pulse Width	It is the time between the mid reference (50%) amplitude point of the pulse.
4		Positive Overshoot	Positive overshoot = (Max – High) / amplitude x 100%.
5		Negative Overshoot	Negative overshoot = (Low – Min) / amplitude x 100%.
6		Pk-Pk	It is the absolute difference between Max and Min amplitude of the pulse.
7		Amplitude	It is the high value less the low value measured over the entire pulse.
8		High	This value used as 100% whenever high reference, mid reference, or low reference values are needed of the entire pulse.
9		Low	This value used as 0% whenever high reference, mid reference, or low reference values are needed of the entire pulse.
10		Max	It is the most positive peak voltage over the entire pulse.

Table 1. Each automatic measurement illustration of pulse definition. The rise and fall time along with the pulse width are time measurements while others are amplitude in the units of volts (cont.).

#	Illustration	Measurement	Definition
11		Min	It is the most negative peak voltage over the entire pulse.
12		RMS	The true Root Mean Square voltage over the entire pulse.
13		Area	It is a voltage over time measurement where the area over the pulse is expressed in volt-seconds. The area above the baseline is positive and negative under the baseline.

The experiment was conducted in three parts. In the first part, the GM counter was used to detect radiation incidents from background radiation. The voltage was set at 370 V because at that voltage the GM counter started to register the radiation incidents which were displayed simultaneously on the oscilloscope's screen. Subsequently, starting with 400V, measurements were taken at various voltages with a 50 V increment until 1000 V. The pulse/s on the screen were captured using the oscilloscope's run/stop option for a duration of 100 ms. Each pulse shape characteristics was analyzed individually using the auto-measurement option. The data obtained from the pulse shape characteristics were entered manually in Microsoft Excel for further analysis; and the image of the observed pulse/s were saved to the PC, as shown in Figure 3. For each of the tested voltage, 15 independent observations were made for pulse size and shape analysis.
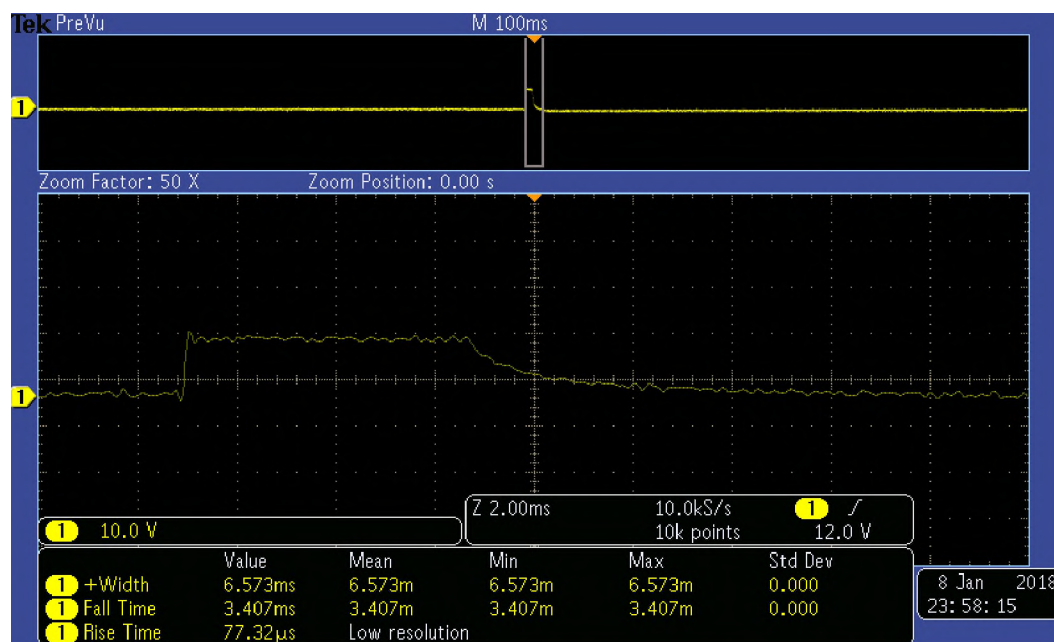
Figure 3. A pulse from background radiation is shown on the oscilloscope's screen. There is only one pulse observed during the whole 100 ms duration.

The second part of the experiment followed the same procedure with ^{60}Co source. The source was placed on a transparent plastic tray 3 cm away from the GM counter. Unlike background radiation where only one pulse at a time was observed on the oscilloscope's screen due to the low number of radiation incidents, the ^{60}Co source had ensued multiple pulses which were simultaneously observed on the oscilloscope's screen, as illustrated in Figure 4. To be consistent across all measurements of the second and third part of the experiment, we decided to capture a train of three pulses or more at a time on the oscilloscope screen to investigate the effect of pulse lapse time on the second pulse characteristics. In addition, the time between the onset of the first and second pulse was measured manually using the two cursors (a and b) knobs on the oscilloscope. The measurement started from the rising edge of the first pulse and ended at the rising edge of the second pulse. The time measured between the two pulses was defined as lapse time.

The lapse time between the second and third pulse was also recorded. The train of three pulses that were captured was assigned as one trail. Again, a total of 15 trails were recorded for the ^{60}Co source. In the third part, the same procedure was followed using ^{137}Cs source.
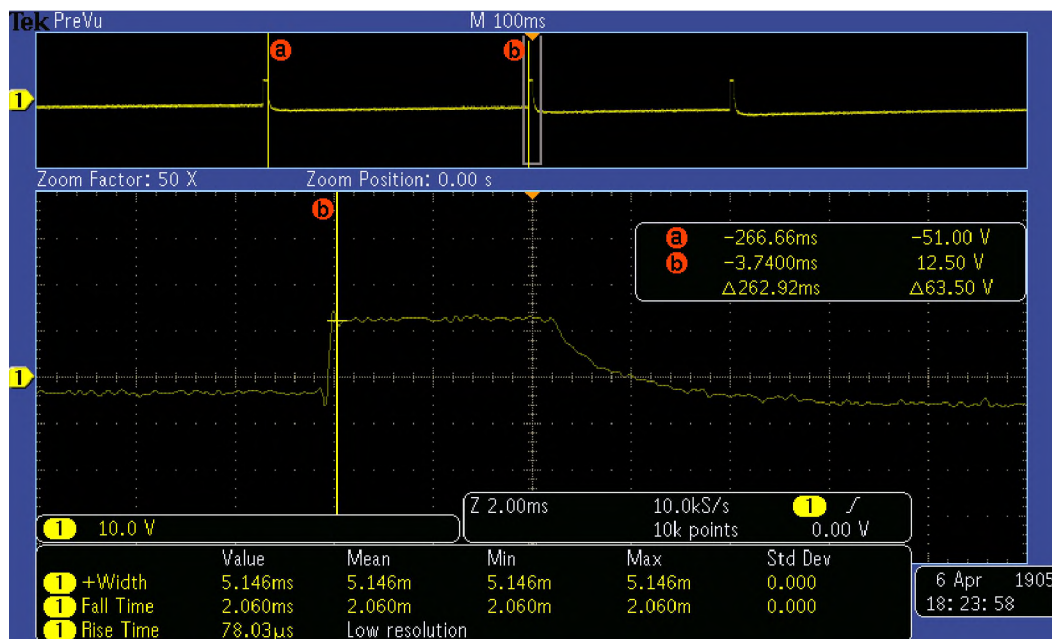
Figure 4. A train of three pulses were captured in a 100ms duration for ^{60}Co. Cursors a and b, on the top of the screen, show the measurement of lapse time between the first and second pulse. The lapse time is 262.92ms. The second pulse on the bottom of the screen was zoomed to 2ms for detailed analysis.

3. RESULTS

All the pulses recorded were analyzed using the pulse characteristics described in Table 1. As an example, Table 2 shows pulse properties for 370V and above while recording background radiation. No pulses were registered by the detection system below 370V. Fall time (row 2, Table 1), pulse width (row 3, Table 1), peak to peak (row 6, Table

1), area (row 13, Table 1), and negative overshoot (row 5, Table 1) for each pulse was recorded and averaged for the applied voltage for 15 independent measurements.

3.1. BACKGROUND RADIATION

First, pulses due to background radiation from the GM counter were captured and analyzed. Table 2 displays the averages for the pulse properties as observed experimentally. Figure 5(a) shows the pulse width dependence on the operating voltage, pulse width seems to drop exponentially with increasing voltage. While for this limited data set, linear fit was also good but the R^2 value for the exponential fit was better. The exponential dependence of the pulse fall time (row 2) is apparent in Figure 5(b) suggesting a reduced charge collection time at high operating voltage. Pulse height or peak-to-peak voltage as shown in Figure 5(c) seems to have a linear relationship (for background data only, when there is no discrete gamma energy is involved) with the operating voltage with a $R^2 = 0.99$. As seen in Figure 5(d), pulse area (row 13, Table 1) for the low background count rate was mostly positive except for the two highest operating voltages. The relationship between the operating voltage and the pulse area seems to be linear with $R^2 = 0.985$. For low count rates, the negative overshoot was also observed to be linearly dependent on the operating voltage as can be seen in Figure 5(e). After collecting the data on the background pulses, two sources, ^{137}Cs and ^{60}Co were introduced independently to investigate the effect of gamma energy on the pulse characteristics. Generally, it is believed that all pulses from a GM counter are identical in all their characteristics, independent of the radiation type and energy. We wanted to show some fine differences in the pulse characteristics depending on the initiating radiation energy.

Each average is taking over 15 independently observed pulses. The background pulses were captured because in the measurement of deadtime, background counts are also collected and subtracted from the final calculations. Due to the low intensity of background radiation in comparison with the ^{137}Cs and ^{60}Co sources, only negative overshoot showed a linear fit as can be seen in Figure 5(e). Nevertheless, negative overshoot of the ^{137}Cs and ^{60}Co sources showed no relationship because of the high intensity of the sources that resulted in high count rates. Hence, negative overshoot data were not included in the analysis of ^{137}Cs and ^{60}Co pulse characteristics.

Table 2. Background radiation and its pulse shape measurements using GM counter at different applied voltages.

Voltage (V)	Pulse Width (ms)	Fall Time (ms)	PK-PK (V)	Area (mVs)	Negative overshoot (%)
370	6.473	3.674	13.467	89.459	8.658
400	6.322	3.245	14.213	83.330	9.504
450	6.224	3.110	14.800	76.899	14.391
500	5.945	2.692	15.387	67.165	18.998
550	5.750	2.017	15.813	62.712	26.075
600	5.557	1.791	16.453	55.083	33.121
650	5.260	1.525	18.080	32.684	40.445
700	5.194	1.422	18.213	33.971	44.595
750	5.049	1.270	19.093	21.918	50.541
800	4.897	1.184	19.680	15.384	56.090
850	4.814	1.083	20.107	11.894	60.904
900	4.666	1.012	20.747	5.362	66.419

Table 2. Background radiation and its pulse shape measurements using GM counter at different applied voltages (cont.).

Voltage (V)	Pulse Width (ms)	Fall Time (ms)	PK-PK (V)	Area (mVs)	Negative overshoot (%)
950	4.562	0.924	21.360	-3.411	67.621
1000	4.311	0.805	22.587	-23.056	71.857
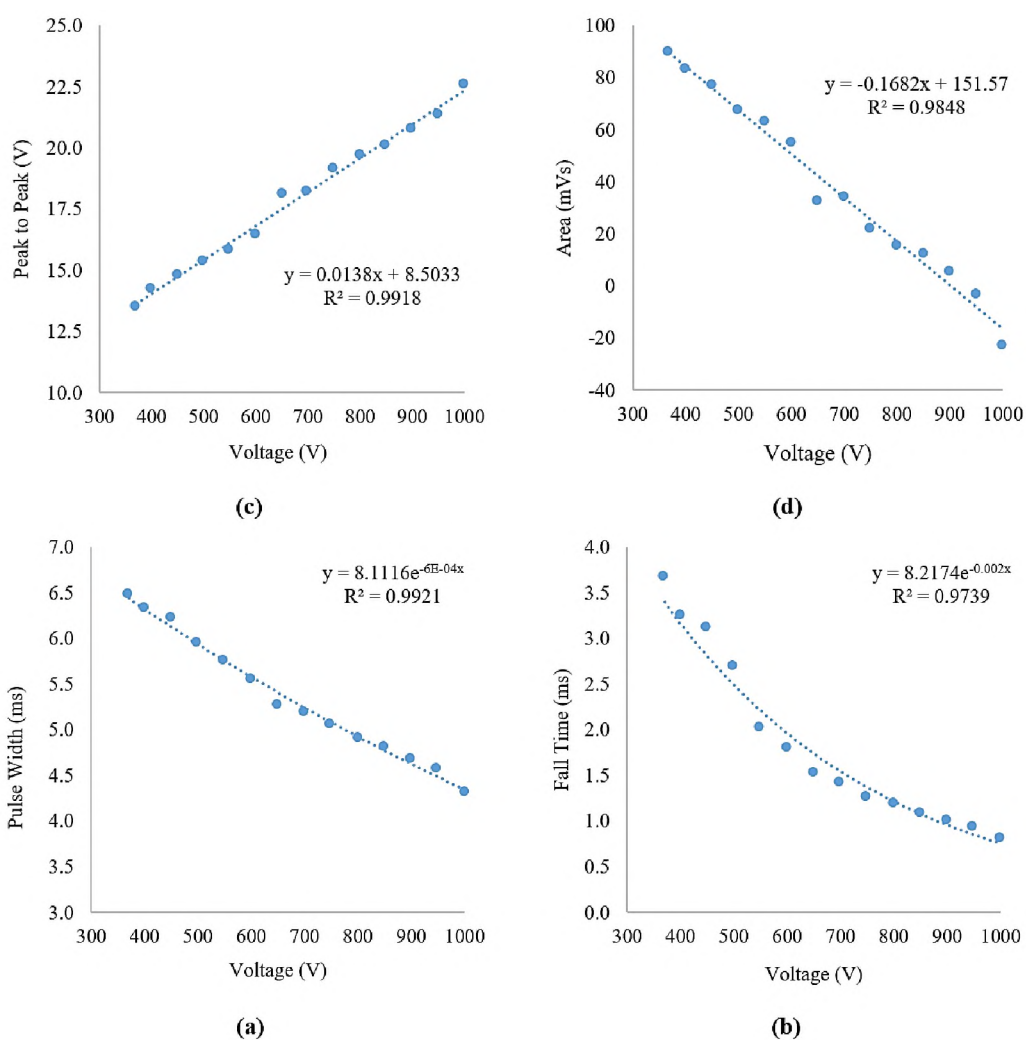
Figure 5. Pulse shape measurements for background radiation using GM counter at different applied voltages: (a) pulse width measurements vs. voltage; (b) fall time vs. voltage; (c) Peak to Peak vs. voltage; (d) area of each recorded pulse vs. voltage; and (e) negative overshoot vs. voltage.
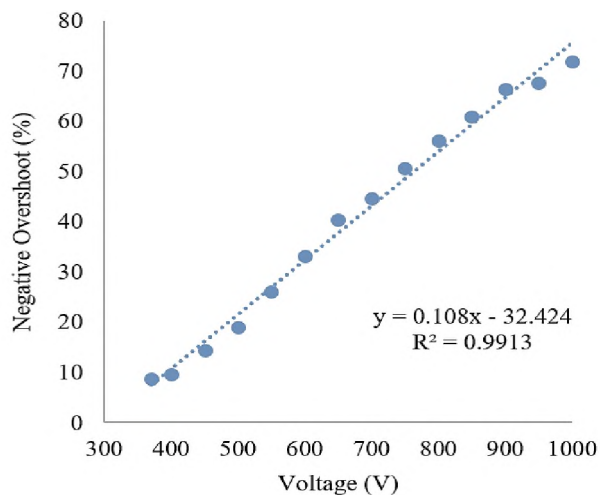
(e)

Figure 5. Pulse shape measurements for background radiation using GM counter at different applied voltages: (a) pulse width measurements vs. voltage; (b) fall time vs. voltage; (c) Peak to Peak vs. voltage; (d) area of each recorded pulse vs. voltage; and (e) negative overshoot vs. voltage (cont.).

3.2. ^{60}CO SOURCE

Second, ^{60}Co pulses from the GM counter were analyzed. ^{60}Co decays with a half-life of 5.272 years emitting two discrete gammas; 1.1732 MeV (99.85%) and 1.3324 MeV (99.98%) [24]. Averages of pulse characteristics for 15 pulses observed with ^{60}Co is shown in Table 3. Generally, data follows the similar behavior as the background except for peak to peak voltages. For ^{60}Co, peak-to-peak data do seem to deviate from the linear fit, and it appears to show an asymptotic peak-to-peak value for higher operating voltage as shown in Figure 6(c). What it physically means is that, at high operating voltage a maximum peak-to-peak is reached and increasing operating voltage further will not impact the pulse peak-to-peak height. Data collection was restricted to 1000 V to avoid any permanent damage to the detector. The area under the curve also showed a linear dependence on the applied voltage. These results are quite revealing for the inside working of the GM counter and

careful data analysis would help the radiation measurement community to gain insight on

GM operation.
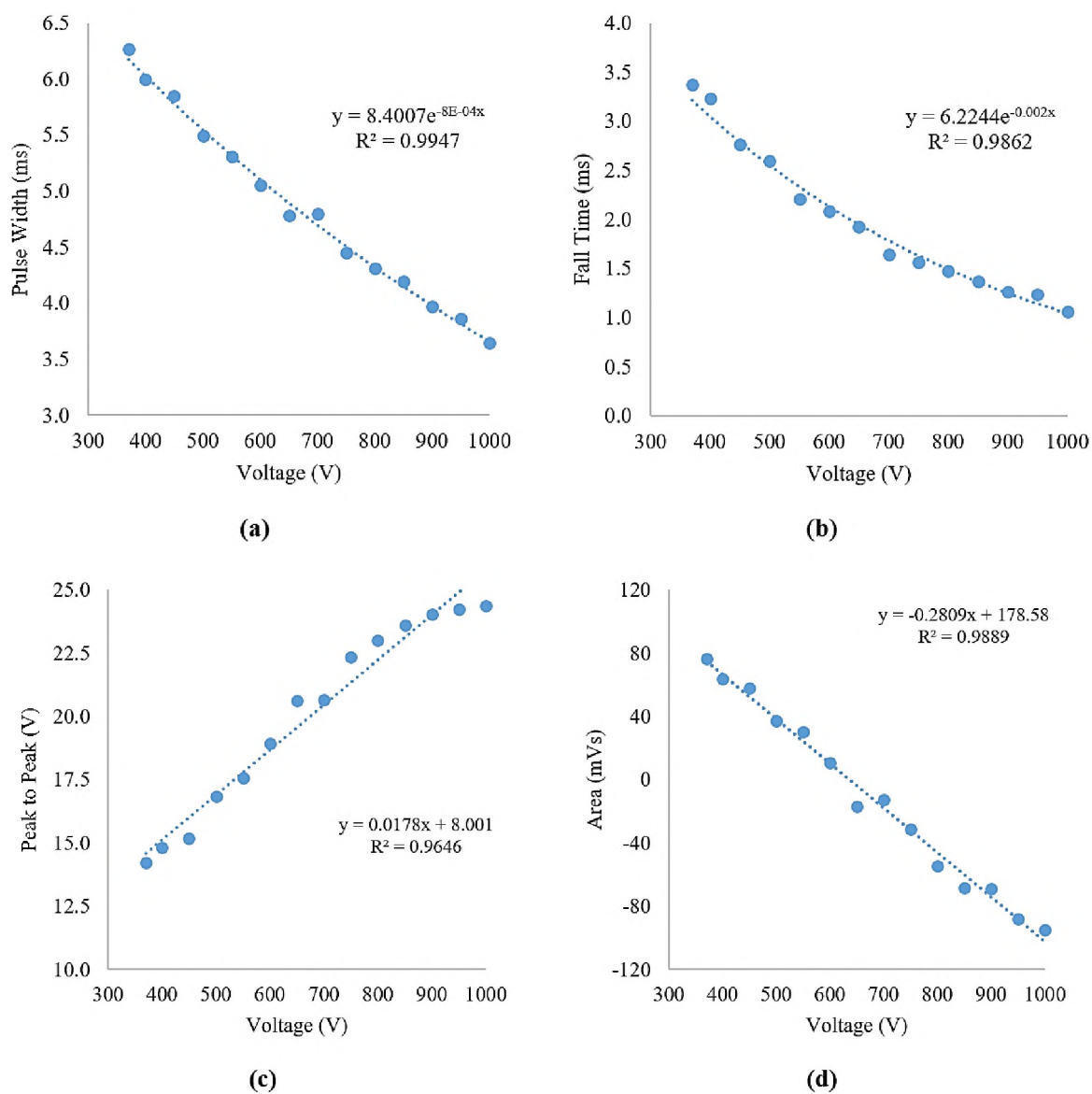
Figure 6. Pulse shape measurements for Co-60 source using GM counter at different applied voltages: (a) pulse width measurements vs. voltage; (b) fall time vs. voltage; (c) Peak to Peak vs. voltage; and (d) area of each recorded pulse vs. voltage.

Table 3. Pulse shape data for Co-60 source using GM counter at different applied voltages.

Voltage (V)	Pulse Width (ms)	Fall Time (ms)	PK-PK (V)	Area (mVs)
370	6.267	3.367	14.213	76.541
400	5.999	3.230	14.827	63.550
450	5.851	2.765	15.173	57.649
500	5.492	2.595	16.827	36.994
550	5.305	2.207	17.573	30.140
600	5.055	2.087	18.933	10.502
650	4.778	1.927	20.613	-16.890
700	4.798	1.642	20.640	-12.466
750	4.450	1.563	22.347	-31.318
800	4.309	1.473	23.013	-54.687
850	4.190	1.368	23.600	-68.173
900	3.969	1.263	24.027	-69.202
950	3.859	1.234	24.240	-87.987
1000	3.646	1.059	24.373	-94.982

3.3. ^{137}CS SOURCE

Lastly, ^{137}Cs's pulses from the GM counter were analyzed. ^{137}Cs has a half-life of 30.08 years and it emits one discrete gamma at 0.661 MeV (85.1%) [25]. Pulse characteristics averaged for 15 pulses observed with ^{137}Cs are shown in Table 4. Generally, data follows the similar behavior as ^{60}Co. However, there are some subtle differences between the pulses from the two gamma sources. For example, ^{60}Co, peak-to-peak data seem to reach an asymptotic value which is higher than ^{137}Cs asymptotic value. The other

significant difference was the poor linear relationship between the pulse area and the operating voltage. As seen in Figure 7(d), the linear fit is perhaps not the best description of the data. These fine differences will be discussed in the conclusion section of the manuscript.

Table 4. Pulse shape data for Cs-137 source using GM counter at different applied voltages.

Voltage (V)	Pulse Width (ms)	Fall Time (ms)	PK-PK (V)	Area (mVs)
370	6.328	3.328	13.920	81.557
400	6.125	3.273	14.693	68.735
450	5.818	3.220	16.107	49.635
500	5.693	2.650	16.533	47.731
550	5.407	2.134	17.387	36.883
600	5.040	2.068	19.200	3.707
650	4.920	1.795	20.187	-7.141
700	4.810	1.596	20.453	-18.212
750	4.466	1.518	22.347	-46.443
800	4.275	1.439	22.827	-53.130
850	4.219	1.387	23.387	-58.021
900	4.124	1.156	23.493	-61.792
950	4.082	1.177	23.520	-62.491
1000	3.981	1.038	23.547	-67.129
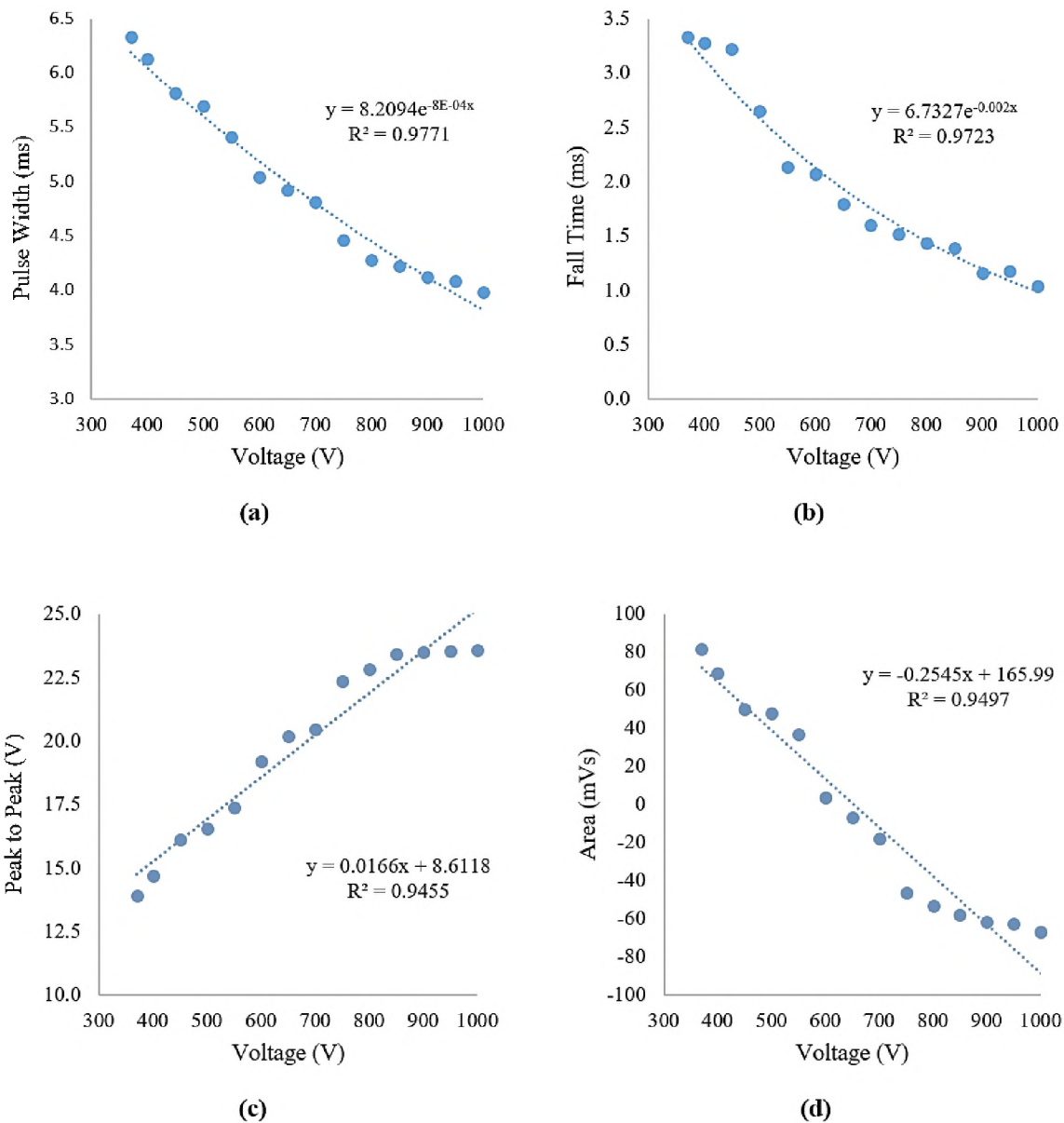
Figure 7. Pulse shape measurements for Cs-137 source using GM counter at different applied voltages: (a) pulse width measurements vs. voltage; (b) fall time vs. voltage; (c) Peak to Peak vs. voltage; and (d) area of each recorded pulse vs. voltage.

4. CONCLUSION & DISCUSSION

Based on the data collected, the general belief that all pulses from a GM counter from any intensity, type and/or energy of radiation source are identical is questionable.

While the pulse shape does not carry any important information for simple count rate application, it does have an impact on the detector deadtime behavior. When comparing the peak-to-peak pulse height, it is evident that both ^{60}Co and ^{137}Cs have an asymptote as shown in Figure 8. It is also difficult to draw a conclusion about the energy dependence of the asymptote with only two radiation sources. However, one is compelled to notice that ^{60}Co (with higher gamma energy) has asymptote which is higher than that of ^{137}Cs (with lower gamma energy). If more data becomes available with a wide spectrum of gamma energies, one would be able to develop a relationship between the asymptote peak-to-peak voltage and gamma energy.
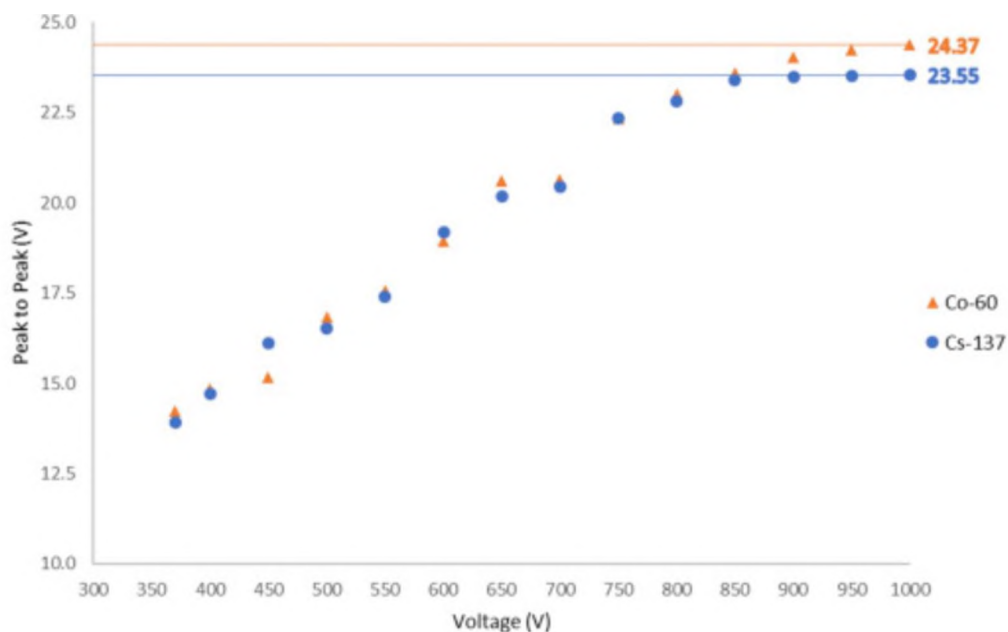
Figure 8. Comparison of Peak to Peak dependence of voltage for ^{60}Co and ^{137}Cs.

Similarly, one is bound to notice that the exponent for the pulse fall time (-0.002) is independent of the source of radiation. For all three cases, background, ^{60}Co and ^{137}Cs the pulse fall time dependence on voltage remains unchanged. The other interesting

observation the slower/weaker voltage dependence of the pulse width as compared to the pulse fall time. The exponent for pulse width was found to be -6.0E-4 for the background measurement while it is -8.0E-4 for both ^{60}Co and ^{137}Cs which is smaller than -2.0E-3 for the pulse fall time. What is means is that the main body of the pulse is weakly dependent on the applied voltage than the pulse tail.
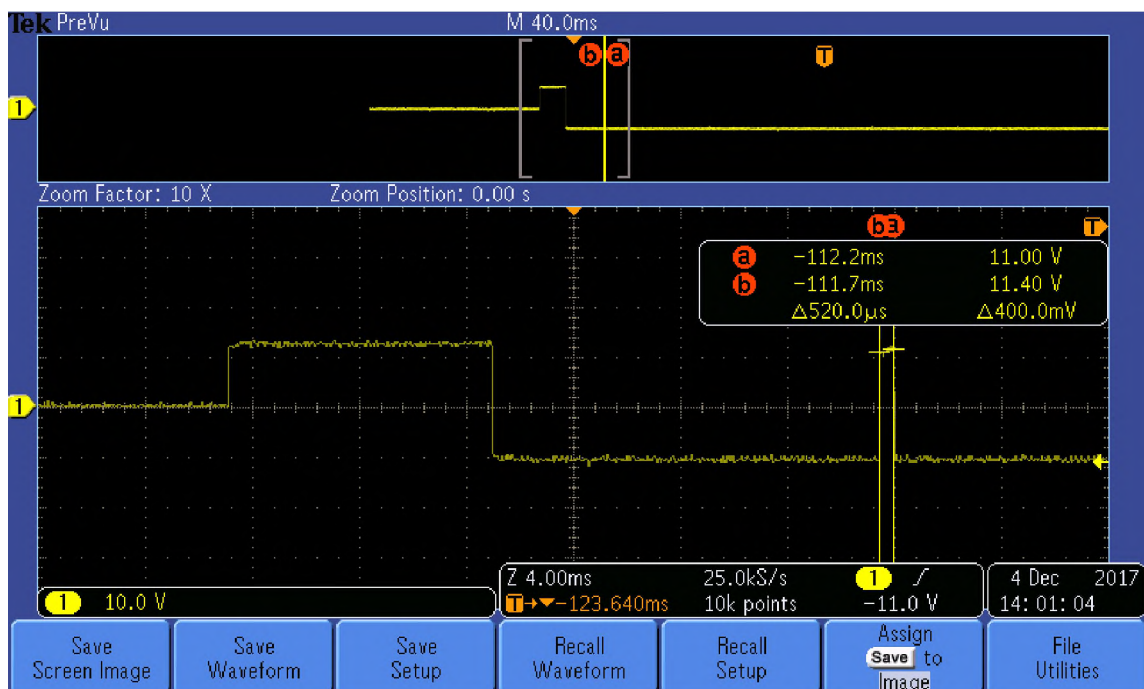
Figure 9. Second pulse width reductions.

Furthermore, detector deadtime was earlier reported to depend on applied voltage [3]. As discussed earlier [3], there are three distinct regions of detector deadtime. At lower voltages, the deadtime reduced with increasing voltage. In this region, as the data presented here suggests, the pulse duration (pulse width plus fall time) is also decreasing with increasing voltage. Consequently, the deadtime decreases with reducing pulse duration. This is because there is a lower probability of overlapping pulses with reduced pulse

duration. The next region is the region of minimum constant deadtime. During this region, pulse tail has completely vanished, and the pulse width was observed to be its minimum. The lower end of this plateau region is best for GM counter operations. Increasing the voltage further will result in second pulse (after an initial pulse) width reduction. The second pulse duration reduction depends not only on the applied voltage but also on the time lapse between the two pulses. Figure 9 shows the screenshot of the reduced second pulse width, 520 μs. Based on the new data presented here there is a strong possibility that one could develop a pulse shape correlation for the detector deadtime.

NOMENCLATURE

GM	Geiger-Mueller
v	Drift Velocity
μ	Mobility
E	Strength of Electric Field
p	Pressure
m	Observed or Measured Count Rate
n	True Count Rate
τ	Deadtime
τ_p	Paralyzing Deadtime
τ_{np}	Non-Paralyzing Deadtime
f	Paralysis Factor

REFERENCES

[1]   Geiger, H., Müller, W. Electron counting tube for the measurement of the weakest radioactivities, The Sciences. 16 (1928) 617–618.

[2]   G.F. Knoll, Radiation Detection and Measurement, third ed., John Willey & Sons Inc., USA, 2000.

[3]   T. Akyurek, M. Yousaf, X. Liu, and S. Usman, GM counter deadtime dependence on applied voltage, operating temperature and fatigue. Progress in Nuclear Energy. 73 (2015) 26-35.

[4]   J.C. May, D.H. J. Russell, A Mass-Selective Variable-Temperature Drift Tube Ion Mobility-Mass Spectrometer for Temperature Dependent Ion Mobility Studies, Journal of the American Society for Mass Spectrometry. 22 (2011) 1134-1145.

[5]   H.G. Stever, The discharge mechanism of fast G–M counters from the deadtime experiment, Phys. Rev. 61 (1942) 38-52.

[6]   J.W. Müller, Dead-time problems, Nucl. Instrum. Methods. 112 (1973) 47-57.

[7]   S.M. Skinner, The efficiency of the tube counter, Phys. Rev. 48 (1935) 438-447.

[8]   L. Costrell, Accurate determination of the deadtime and recovery characteristics of Geiger-Muller counters, Journal of Research of the National Bureau of Standards, 42-3 (1949) 241-249.

[9]   J.H. Lee, I. J. Kim, H.D. Choi, On the dead time problem of a GM counter, Appl. Radiat. and Isot., 67-6 (2009) 1094-1098.

[10] R.P. Gardner, L. Liu, On extending the accurate and useful counting rate range of GM counter detector system, Appl. Radiat. Isot. 48 (1997) 1605-1615.

[11] S.H. Lee, R.P. Gardner, A new G–M counter dead time model, Appl. Radiat. Isot., 53 (2000) 731.

[12] A. Patil, S. Usman, Measurement and application of paralysis factor for improved detector dead time characterization. Nucl. Technol. 165(2) (2009) 249-256.

[13] T. Akyurek, L.P. Tucker, X Liu, S. Usman, Portable spectroscopic fast neutron probe and 3He detector dead-time measurements, Progress in Nuclear Energy, 92 (2016) 15-21.

[14] M. Yousaf, T. Akyurek, S. Usman, A comparison of traditional and hybrid radiation detector dead-time models and detector behavior, Progress in Nuclear Energy, 83 (2015) 177-185.

[15] N. Tsoulfanidis, S. Landsberger, Measurement and Detection of Radiation, third ed. CRC Press, New York, 2012.

[16] W. Feller, On probability problems in the theory of counters. In: R. Courant Anniversary Volume, Studies and Essays. Interscience, New York, (1948) 105-115.

[17] R. D. Evans, The Atomic Nucleus, McGraw-Hill, New York, 1955.

[18] S. Usman, B. Almutairi, T. Akyurek, A new phenomenological model for Geiger-Müller deadtime, Transactions of the American Nuclear Society, 117 (2017) 496-498.

[19] Cesium-137 Source, http://www.spectrumtechniques.com/wp-content/uploads /2016 /12/Cesium-137-Information-Sheet.pdf.

[20] G-M counter, https://ludlums.com/products/all-products/product/model-133-2.

[21] Ortec 142A/B/C Preamplifiers, https://www.ortec-online.com/-/media/ametekortec /brochures/142abc.pdf.

[22] Ortec High-Voltage Power Supply, https://www.ortec-online.com/-/media/ameteko rtec/brochures/556-556h.pdf.

[23] Tektronix Digital Phosphor Oscilloscopes, https://www.tek.com/bench-oscilloscopes /mso3000-dpo3000-manual/mso3000-and-dpo3000-series.

[24] E. Browne, J.K Tuli, Table of Nuclides for Co-60, ENSDF, International Atomic Energy Agency. Nuclear Data Sheets 114, 1849 (2013).

[25] E. Browne, J.K Tuli, Table of Nuclides for Cs-137, ENSDF, International Atomic Energy Agency. Nuclear Data Sheets 108, 2173 (2007).

II. EXPERIMENTAL EVALUATION OF THE DEADTIME PHENOMENON FOR GM DETECTOR: DEADTIME DEPENDENCE ON OPERATING VOLTAGES

Bader Almutairi[1,3,4], Syed Bahauddin Alam[1], Tayfun Akyurek[2], Cameron S. Goodwin[3], Shoaib Usman[1]

[1]Mining and Nuclear Engineering, Missouri University of Science & Technology, Rolla, MO, 65401, USA, email:usmans@mst.edu

[2]Department of Physics, Faculty of Art and Science, Marmara University, 34722, Kadikoy, Istanbul, TURKEY

[3]Rhode Island Atomic Energy Commission, 16 Reactor Rd., Narragansett, RI, 02882, USA

[4]Environment and Life Sciences Center, Kuwait Institute for Scientific Research, Kuwait City 13109, KUWAIT

ABSTRACT

A detailed analysis of Geiger Mueller (GM) counter deadtime dependence on operating voltage is presented in the manuscript using four pairs of radiation sources. Based on two-source method, detector deadtime is calculated for a wide range of operating voltages which revealed a peculiar relationship between the operating voltage and the detector deadtime. In the low voltage range, a distinct drop in deadtime was observed where deadtime reached a value as low as a few microseconds (22 μs for ^{204}Tl, 26 μs for ^{137}Cs, 9 μs for ^{22}Na). This sharp drop in the deadtime is possibly due to reduced recombination with increasing voltage. After the lowest point, the deadtime generally increased rapidly to reach a maximum (292 μs for ^{204}Tl, 277 μs for ^{137}Cs, 258 μs for ^{22}Na). This rapid increase in the deadtime is mainly due to the on-set of charge multiplication. After the maximum deadtime values, there was an exponential decrease in the deadtime

reaching an asymptotic low where the manufacturer recommended voltage for operation falls. This pattern of deadtime voltage dependence was repeated for all sources tested with the exception of ^{54}Mn. Low count rates leading to a negative deadtime suggested poor statistical nature of the data collected for ^{54}Mn and the data while being presented here is not used for any inference.

1. INTRODUCTION

Radiation detector deadtime has been a phenomenon of interest for scientists and engineers for decades. For any detector system, two events must be separated by a minimum time interval for these events to be recorded as independent. This minimum separation time is called the detector deadtime.[1, 2, 3] Deadtime depends on the detector's design, operating conditions, and the pulse processing circuitry.[4] The combined deadtime of a measurement system is the sum of all contributing factors, including the detector's intrinsic deadtime, pulse shaping time associated with the preamplifier and the amplifier, analog to digital conversion time, and the data sorting time (MCA) and storage time.[5] A detailed description of the various contributors to total deadtime is included in radiation detector deadtime review article by Usman and Patil.[5] Generally speaking, the system's deadtime can be divided into two parts: 1) the internal losses in the detector itself, 2) count losses in the system circuitry, and pulse processing. In many cases, the deadtime is mostly caused by the associated electronics. However, for the case of a GM counter, the processes within the detector itself are the major contributors to the deadtime.

There are two idealized deadtime models: paralyzing and non-paralyzing. These deadtime models are traditionally used in the industry as well as in academia. According

to the paralyzing deadtime model, each radiation event will be followed by an extendable deadtime. Unless the time gap between the two sequential events is greater than the deadtime, the subsequent event will not be recorded. In this case, the true count rate (n) is related to the observed or measured count rate (m) by the following expression:

$$m = n \ e^{-n\tau} \tag{1.1}$$

where m is the measured or observed count rate, n is the true count rate, and τ is deadtime. On the other hand, for the non-paralyzing model, each radiation event will not be followed by an extendable deadtime; instead, it will reset to zero. The true count rate for the non-paralyzable model is expressed as follows:

$$m = \frac{n}{(1 + n\,\tau)} \tag{1.2}$$

These simple, yet useful models have been extensively discussed and utilized.[1, 6] In 1978, Muller[7, 8] provided a rather simplified and generalized deadtime model. Another hybrid deadtime model was proposed by Albert and Nelson.[9] This hybrid model was further developed by Lee and Gardner.[10] This model uses two independent deadtimes combined in one equation as follows:

$$m = \frac{n \ e^{-n\,\tau_P}}{1 + n\,\tau_N} \tag{1.3}$$

where τ_P is the paralyzable deadtime, and τ_N is the non-paralyzable deadtime. Lee and Gardner[10] were able to find the values of their deadtimes by using the least square fitting of decaying of ^{56}Mn source. Hou and Gardner proposed an improved version of these deadtime models[11] by further dividing the paralyzing and non-paralyzing components into three subcomponents. In 2009, another deadtime hybrid model was proposed by Patil and Usman.[12] The hybrid model is mathematically expressed as follows:

$$m = \frac{n\,e^{-nf\tau}}{1 + n\,\tau\,(1-f)} \qquad (1.4)$$

where τ is the total deadtime, and it is used with a probability-based paralysis factor, f. The paralysis factor value can be any value between 0 and 1. If the paralysis factor is 0, then the hybrid model reduces to a non-paralyzing model. However, if the paralysis factor is 1, then the hybrid model reduces to a paralyzing model. A graphical technique is proposed with a decaying source data to obtain the parameters needed for the model use.[12]

None of these researchers have investigated deadtime dependence on the operating conditions and how, if any impact aging would have on detector deadtime. Akyurek et al.[4] provided some preliminary data on deadtime dependence on operating conditions and aging. Literature has also been limited to the relationship between pulse shape and detector deadtime. While various regions of operation for gas-filled detectors are well documented,[1, 6] not much is available in the literature, establishing a relationship between detector deadtime and the operating voltage. Likewise, the dependence of pulse shape on the operating voltage of a gas-filled detector is not sufficiently discussed in the literature. Another important area of detector deadtime research missing in the literature is the performance of proportional counter in current mode and the impact of deadtime on observed current. All these areas of research are important for the radiation measurement community and any effort in any of these areas will be welcome by the community.

Any detailed analysis of deadtime dependence on the operating voltage is likely to help the community develop a better understating of the fundamental phenomenon of deadtime and its behavior. Here we present detailed data on detector deadtime dependence on the operating voltage. In this research, all data was collected using four different radioactive sources according to the two-source method. The data collected in the current

study shows a clear deadtime dependence on the applied voltage. Three of the radioactive sources showed similar pattern on voltage dependence, hinting to a possible phenomenological basis of this behavior. Nonetheless, the fourth radioactive source showed a different behavior and will be discussed further in the results and discussion section.

2. MATERIALS AND METHODS

2.1. MATERIALS

Figure 1a illustrates the basic experimental setup of the radiation detection system used to evaluate deadtime in this study. The radiation detection system encompasses; a pair of radioactive sources, GM counter, high voltage power supply, pre-amplifier, oscilloscope, amplifier, discriminator, and dual counter/timer.

Radioactive sources of each element consisted of two split sources (the shape of each split source is a half-circle). Four sets of radioactive sources were used in the current study: First, Thallium-204 (^{204}Tl)—produced in February 2019. Second, Cesium-137 (^{137}Cs), Third, Sodium-22 (^{22}Na, and Fourth, Manganese-54 (^{54}Mn). The ^{137}Cs, ^{22}Na, and ^{54}Mn sources were all produced in May 2019. Spectrum Techniques specifically produced the ^{137}Cs, ^{22}Na, and ^{54}Mn split sources upon our request for conducting this study. Each split source has an initial activity of 5 µCi.[13] All experiments were conducted in June and July of 2019 during this time the respective source strength were approximately ^{204}Tl=4.63 µCi, ^{137}Cs=4.98 µCi, ^{22}Na=4.78 µCi and ^{54}Mn=4.37 µCi. Nonetheless, the uncertainties of the initial activities of the split sources in this study did not inflict significant measurement or statistical errors. This can be confirmed by the fact that each radioactive split source,

when measured individually, resulted in a similar number of registered counts by the GM

detector. All sources used in this study had the same size and geometry. Figure 1b-e show

the radioactive sources of each element.

A GM detector (Ludlum, model 44-7) was used to detect radiation events. The GM

counter is a halogen quenched, end window (a thin mica window) type detector. The

counter is able to detect alpha, beta, and gamma radiations. According to the manufacturer

of the detector, the typical deadtime of this model is 200 μs at the recommended operating

voltage of 900 V. The sensitivity of the detector for ^{137}Cs is 2100 cpm/mR/hr.[14] A charge-

sensitive pre-amplifier (Ortec, model 142A) was used to extract the signals from the

detector without degradation of the signal-to-noise ratio. The pre-amplifier was placed as

close as possible to the detector to keep the signal degradation at its lowest. The pre-

amplifier was connected to the GM detector through a connector series "C" with a coaxial

cable.[15] A high voltage (HV) power supply (Canberra, model 3125) was connected directly

to the AC line. The HV is capable of providing 0 to 5000 V bias voltage with 0 to 300 μA

output current. The HV is housed in the nuclear instrumentation module (NIM) along with

the amplifier, discriminator, and dual counter/timer. The HV was connected to the input

bias of the pre-amplifier through a coaxial cable.[16] An oscilloscope (Tektronix, model

TBS2000) was connected directly to the pre-amplifier through a "T" connector.[17] The

oscilloscope was used to record all properties of the generated pulses by the GM counter

after being processed by the pre-amplifier. The generated pulses recorded by the

oscilloscope are discussed in detail in a companion paper.[18] An amplifier (Ortec, model

570) was used to magnify the amplitude of the pre-amplifier output pulse. The amplifier

was connected to the pre-amplifier through a "T" connector and to the discriminator

through a coaxial cable. The direct-reading gain factor of the amplifier is adjustable from X1 to X1500. In addition, the coarse gain has six-position for selecting the feedback resistors for the gain factor of 20, 50, 100, 200, 500, and 1K. The amplifier has a shaping time capability that selects the time constant for an active filter network in which the selections are 0.5, 1, 2, 3, 6, and 10 μs.[19] An integral discriminator (Canberra, model 832) was utilized to produce logic output pulses when the linear input pulses amplitude from the amplifier exceeded a threshold. The discriminator level is adjustable from 0 to 10 V.[20] The discriminator is connected to the counter/timer through a coaxial cable. A counter/timer (Ortec, model 994) was used in order to set the timer and display the number of radiation incidents taking place in the GM counter. The counter has a time-base option where time can be specified by a preset value and can range from 0.01 seconds to 990,000 seconds or 0.01 to 990,000 minutes.[21]
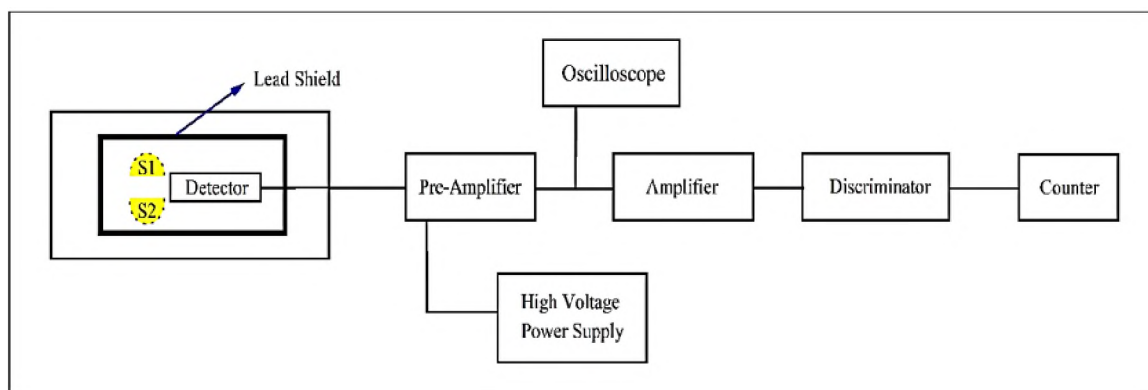
(a)

Figure 1. a) Experimental setup for the radiation detection system. b) Thallium-204 split sources used in the experiments. c) Cesium-137 split sources with blank disk. The blank disk filled the position of the second split source when counts were performed to ensure that scattering was unchanged. d) Sodium-22 split sources. e) Manganese-54 split sources.
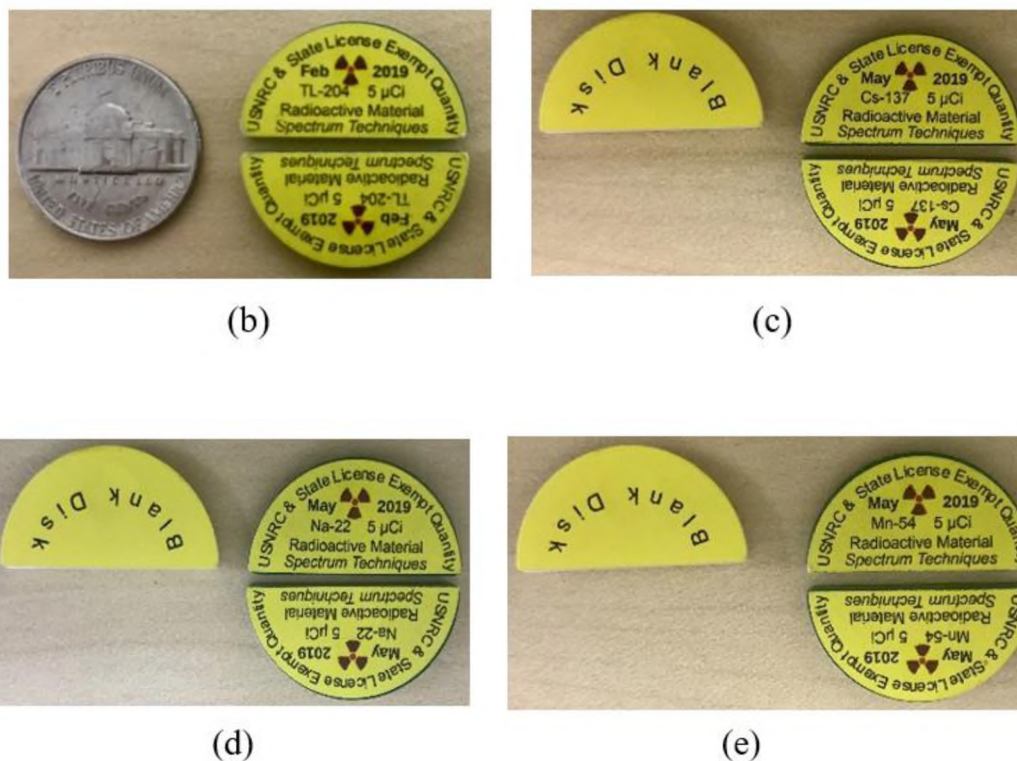
Figure 1. a) Experimental setup for the radiation detection system. b) Thallium-204 split sources used in the experiments. c) Cesium-137 split sources with blank disk. The blank disk filled the position of the second split source when counts were performed to ensure that scattering was unchanged. d) Sodium-22 split sources. e) Manganese-54 split sources (cont).

2.2. METHODS

The standard two-source measurement method was utilized for deadtime-voltage dependence measurements throughout this study. This method is based on measuring count rates at an applied voltage over three parts while using: the split sources individually; and a combination of the split sources. Since count losses are nonlinear in this type of experiment, the measured count rates of the combined sources should result in fewer measured counts than if split sources 1 & 2 were summed up individually. For brevity, split

source one and split source two are called S1 and S2, respectively, while split sources 1 & 2 combined are called S12.

Previous studies have reported that a GM counter suffers 5% or less paralysis factor; henceforth, the assumption of using a non-paralyzing model while using the simple two-source measurement method for the GM counter is justifiable.[4, 5, 10] The method's details are outlined in the Knoll's textbook.[1] Deadtime was calculated for each applied voltage using the non-paralyzing model based on the following equations:

$$X = s_1 s_2 - BKG s_{12} \tag{2.2.a}$$

$$Y = s_1 s_2 . (s_{12} + BKG) - BKG . s_{12} . (s_1 + s_2) \tag{2.2.b}$$

$$Z = \frac{Y(s_1 + s_2 - s_{12} - BKG)}{X^2} \tag{2.2.c}$$

$$\tau = \frac{X(1 - \sqrt{1 - Z})}{Y} \tag{2.2.d}$$

where s_1, s_2, s_{12} are measured count rates of split source 1, split source 2, and split sources 1 & 2 combined, respectively. BKG stands for the background counting rate measurement and τ stands for deadtime. Since the two-source method depends on observing the difference between large numbers of s_1 and s_2, careful measurements were carried out. A series of experiments were conducted using ^{204}Tl split sources at the early stage of this study to optimize each instrument in the detection system. The optimization is based on manipulating the instruments over the GM voltage range region in order to achieve a fractional deadtime of S12 of at least 20% and not exceeding 40%. The only instruments manipulated during this optimization effort were the amplifier and the discriminator. Pulse shape setting controlled by the amplifier exhibited the most profound impact. This was

performed because the calculated true count rates and deadtimes become sensitive to small variations in measured count rates.

In this section, the details of the experimental method are presented. The split sources were placed on a paper on a tray in a rack (the rack—holds the radioactive sources and GM detector on position inside the lead shield). The position of the split sources was marked on the paper for the subsequent measurements. This step was performed to ensure that the split sources of the various elements during each experiment have the same location and geometry. Hence, the same solid angle applied to all of the duplicated experiments. In order to obtain the optimal results of deadtime, a fractional deadtime ($s_{12} \tau$) of at least 20% was designed to achieve in the GM operating range.[1] Based on the results of multiple repeated experiments to obtain the desired fractional deadtime, it was determined that the optimal shelf level to hold the tray with the radioactive sources for all experiments was the second from the top of the rack. When the source is placed on the second shelf level, the distance between the source and the detector end-window is 20.65 mm. However, this was not the case with Manganese-54 (Mn-54) because it resulted in fewer observed count rates. Nevertheless, Mn-54 radioactive split sources were also placed on the second shelf in order to be consistent and comparable to the other utilized sources.

To attain the fractional deadtime of 20%, each instrument in the detection system was adjusted. Consequently, the amplifier's gain was set at 0.5, while the coarse gain at 1K. Even though the GM detector and radioactive sources were housed inside a lead shield to reduce the background radiation, the discriminator was used to reduce the background noise further. The discriminator level was set at 5 V. The timer was set for 30 minutes for each experiment. The 30 minutes duration was sufficient time for counting for our purposes

in order not to get negative deadtime values (Mn-54 did produce two negative deadtime and the reasoning behind will be discussed further in the next section). The lowest applied voltage was 570 V for all radioactive sources because it was the operating voltage where the GM counter started to register radiation events. However, the counts were low at 570 V, which resulted in attaining negative deadtimes; thus, data collection started at 600 V. According to the manufacturer of the GM detector, the detector is prone to damage at higher voltages; therefore, 1200 V was the highest applied voltage investigated. This limited was set solely to ensure the safe operation of the GM counter for the subsequent experiments. Due to this high voltage limit of 1200 V, the discharge region was not observed where the deadtime starts to increase rapidly. The observation of discharge region is beyond the scope of this study.

After the radiation detection system was optimized, background radiation events were measured and recorded at each operating voltage from 600 to 1200 V. In order to investigate the deadtime-voltage relationship in detail, the applied voltages were increased incrementally by 50 V for all experiments. For each applied voltage, the timer was set for 30 minutes. Background radiation incidents were also counted for 30 minutes at different operating voltages from 600 to 750 V with 10 V increments. These latter measurements were carried out after observing the unusual behavior of deadtime-voltage dependence measurements for the ^{204}Tl, ^{137}Cs, and ^{22}Na sources at the lower applied voltage range.

Counting measurements using the radioactive sources were performed, and the counting rates due to the ^{204}Tl split source were recorded. S1 was measured only with the blank disk. The same process was repeated using S2 with the blank disk. S1 and S2 were combined for the final counting measurement. The series of counting measurements (S1,

S2, and S12) were repeated for each operating voltage from 600 to 1200 V with 50 V increments, and from 600 to 700 V with 10 V increments. All the data was recorded and entered manually in origin software for further data processing and analysis.

Similar procedures were followed methodically using the ^{137}Cs and ^{22}Na sources. However, for ^{22}Na sources, operating voltages from 650 to 750 V with 10 V increments were taken instead of 600 to 700 V. The different applied voltages for ^{22}Na sources were based on the shift of observed deadtime behavior at these low voltages. For the ^{54}Mn sources, the same methodology was followed; however, only measurements from 600 to 1200 V were conducted. This is because there was no noticeable deadtime behavior at lower operating voltages. The reason behind the difference in the applied voltage range for the ^{137}Cs, ^{22}Na, and ^{54}Mn sources is discussed in the next section.

3. RESULTS AND DISCUSSION

3.1. THALLIUM-204 SOURCE

^{204}Tl sources were used for the measurement of deadtime at different applied voltages. ^{204}Tl decays with a half-life of 3.783 years. The probability mode of decay is 97.08% by beta emission with decay energy of 763.4 KeV while 2.92% by electron capture (EC) with 344.3 KeV.[22] Figure 2 shows the decay scheme of ^{204}Tl.

Figure 3a shows voltage vs. deadtime from 600 to 1200 V, while the raw data plus the calculated deadtime can be seen in Table 1. At 600 V, deadtime was 200.56 μs. Above the initial voltage, deadtime decreased rapidly to 83.78μs at 650 V. It was noted that above 650 V, there was a sharp increase in deadtime at 700 V with 291.53 μs. Increasing the

voltage further showed a decrease in deadtimes until a plateau was reached from about 1050 V to 1200 V.
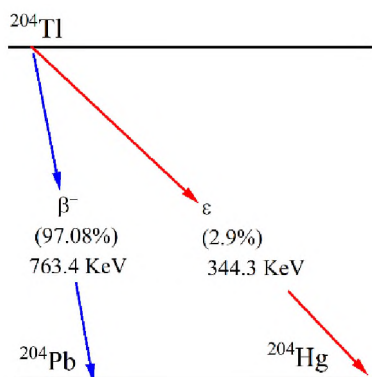
Figure 2. A schematic of the ^{204}Tl decay.

Furthermore, based on the data collected from 750 to 1050 V, it is observed that there is an exponential decrease. An exponential fit of this range shows a coefficient of determination (R^2=0.98462). These findings reveal a different deadtime relationship behavior than that observed by a previous study conducted by Akyurek et al.[4] In their study, deadtimes were measured at different operating voltages. But Akyurek et al. only investigated voltages at a narrow range— within 200 V with 10 V increments. According to their study, deadtime showed a linear decrease at low voltages while it plateaued in middle voltages only to linearly increase at higher voltages. Our detailed analysis showed a non-linear behavior suggesting that earlier reported linear behavior could very well be due to limited data points and short range of observation. This deadtime-voltage-dependence linear relationship was not observed in our study. This might be because, in our study, a more extensive range of voltages were investigated with increments of 50 V. It is worth mentioning that the operating voltage was not increased beyond 1200 V because

the detector would be damaged; therefore, 1200 V was the highest applied voltage for all the experiments.

Table 1. Deadtime results at different operating voltages from 600 V to 1200 V. s_1, s_{12}, s_2 are split source 1, split sources 1 & 2 and split source 2 of Thallium-204, respectively. CPS stands for counts per second whereas BKG stands for background radiation. Deadtime was calculated using the non-paralyzing model.

VOL-TAGE (V)	S1 (CPS)	S12 (CPS)	S2 (CPS)	BKG (CPS)	DEADTIME (S)
600	598.14 ± 0.57	1067.33 ± 0.77	597.23 ± 0.57	0.14 ± 0.00	2.00e-04 ± 7.88e-07
610	645.02 ± 0.59	1128.46 ± 0.79	627.04 ± 0.59	0.17 ± 0.00	1.99e-04 ± 7.36e-07
620	865.17 ± 0.69	1492.02 ± 0.91	882.30 ± 0.70	0.24 ± 0.01	1.95e-04 ± 5.34e-07
630	884.64 ± 0.70	1530.54 ± 0.92	899.36 ± 0.70	0.29 ± 0.01	1.85e-04 ± 5.07e-07
640	885.14 ± 0.70	1596.81 ± 0.94	880.69 ± 0.69	0.31 ± 0.01	1.19e-04 ± 4.16e-07
650	870.36 ± 0.69	1617.07 ± 0.94	864.50 ± 0.69	0.32 ± 0.01	8.37e-05 ± 3.78e-07
660	818.16 ± 0.67	1606.33 ± 0.94	844.49 ± 0.68	0.31 ± 0.01	4.19e-05 ± 3.51e-07
670	815.44 ± 0.67	1586.81 ± 0.93	800.42 ± 0.66	0.32 ± 0.01	2.24e-05 ± 3.46e-07
680	796.17 ± 0.66	1466.09 ± 0.90	791.46 ± 0.66	0.32 ± 0.01	1.04e-04 ± 4.47e-07
690	793.72 ± 0.66	1378.83 ± 0.87	815.62 ± 0.67	0.32 ± 0.01	2.07e-04 ± 5.95e-07
700	829.44 ± 0.67	1343.46 ± 0.86	841.35 ± 0.68	0.34 ± 0.01	2.91e-04 ± 7.25e-07
750	979.92 ± 0.73	1524.16 ± 0.92	971.86 ± 0.73	0.39 ± 0.01	2.87e-04 ± 6.44e-07
800	1023.18 ± 0.75	1683.34 ± 0.96	1041.96 ± 0.76	0.39 ± 0.01	2.19e-04 ± 5.00e-07
850	1107.85 ± 0.78	1801.61 ± 1.00	1083.49 ± 0.77	0.42 ± 0.01	1.97e-04 ± 4.42e-07
900	1130.41 ± 0.79	1881.12 ± 1.02	1121.53 ± 0.78	0.50 ± 0.01	1.74e-04 ± 3.98e-07
950	1146.96 ± 0.79	1920.77 ± 1.03	1161.72 ± 0.80	2.70 ± 0.03	1.74e-04 ± 3.84e-07
1000	1191.06 ± 0.81	2014.12 ± 1.05	1194.91 ± 0.81	2.02 ± 0.03	1.54e-04 ± 3.46e-07
1050	1208.53 ± 0.81	2041.47 ± 1.06	1254.10 ± 0.83	10.65 ± 0.07	1.65e-04 ± 3.47e-07

Table 1. Deadtime results at different operating voltages from 600 V to 1200 V. s_1, s_{12}, s_2 are split source 1, split sources 1 & 2 and split source 2 of Thallium-204, respectively. CPS stands for counts per second whereas BKG stands for background radiation. Deadtime was calculated using the non-paralyzing model (cont.).

VOL-TAGE (V)	S1 (CPS)	S12 (CPS)	S2 (CPS)	BKG (CPS)	DEADTIME (S)
1100	1223.97 ± 0.82	2081.71 ± 1.07	1270.07 ± 0.84	13.62 ± 0.08	$1.56e\text{-}04 \pm 3.30e\text{-}07$
1150	1254.76 ± 0.83	2092.49 ± 1.07	1290.33 ± 0.84	13.99 ± 0.08	$1.67e\text{-}04 \pm 3.41e\text{-}07$
1200	1258.86 ± 0.83	2123.45 ± 1.08	1287.81 ± 0.84	12.75 ± 0.08	$1.53e\text{-}04 \pm 3.21e\text{-}07$

Next, deadtime between 600 V and 670 V with 10 V increments showed a rapid decrease and followed by a rapid increase from 670 to 700 V. This rapid decrease and increase of deadtime is not reported in the literature. Therefore, we investigated this range more in detail from 600-700 V, as can be seen in Figure 3c. Count rates in this voltage range is shown in Figure 3d. From 600 to 630, deadtime showed a slight decrease, followed by a rapid decrease from 630-670 V, where it showed the lowest calculated deadtime of 22.43 μs. Next, deadtime started to increase to its highest value at 700 V.

Figure 3b shows count rates vs. voltage. Split sources 1 & 2 (S12) combined produced more radiation events than if only one split source is used; hence, we will discuss S12 throughout this study. At 600 V, S12 resulted in 1067 counts/sec. However, at 650 V, the count rate increased significantly, with a total of 1617 counts/sec. This rather high-count rate at a low voltage is mainly due to the fact that observed deadtime was very low, which means that the detector was able to count more radiation events.

Similar to the observed exponential behavior of the deadtime curve between 750-1050 V, count rates also showed an exponential behavior; however, it was increasing with

increasing applied voltages. The exponential fits can be seen in Figure 3b, while the parameters for S1, S12, S2 are shown in Table 2. As voltages increased further, count rates increased correspondingly.

The increasing exponential count rate behavior is observed only at higher applied voltages. Nonetheless, the count rate showed different behavior in the narrow range (600 to 700 V). Count rates increased from 600 V to 620 V and plateaued until 670 V, and then it slightly decreased.

(a)

(b)

Figure 3. a) Deadtime vs. voltage for the ^{204}Tl source for the wider range of voltages. Also, the parameters of the exponential fit are shown in the table under the deadtime curve. b) Count rate vs. voltage with exponential fits imposed on the curves. c) Deadtime vs. voltage for the ^{204}Tl source for the narrow voltages range. d) Counts vs. voltage for the ^{204}Tl for low voltages.

(c)

(d)

Figure 3. a) Deadtime vs. voltage for the ^{204}Tl source for the wider range of voltages. Also, the parameters of the exponential fit are shown in the table under the deadtime curve. b) Count rate vs. voltage with exponential fits imposed on the curves. c) Deadtime vs. voltage for the ^{204}Tl source for the narrow voltages range. d) Counts vs. voltage for the ^{204}Tl for low voltages (cont.).

Table 2. Parameters of the exponential model fit of Figure 3b using Thallium-204 split sources S1, S12, and S2. The table was generated through exponential curve fitting analysis using Origin software version (2019b).

MODEL	EXPONENTIAL		
EQUATION	$y = y_0 + A * e^{(R_0 * x)}$		
SOURCE #	S1	S12	S2
Y0	1288.32 ± 66.78	2170.03 ± 55.72	1905.53 ± 757.71
A	-9035.23 ± 10164.42	-34160.91 ± 21091.19	-2142.82 ± 99.87

Table 2. Parameters of the exponential model fit of Figure 3b using Thallium-204 split sources S1, S12, and S2. The table was generated through exponential curve fitting analysis using Origin software version (2019b) (cont.).

MODEL	EXPONENTIAL		
R0	-0.004 ± 0.001	-0.005 ± 9.16e-4	-0.0011 ± 0.001
R-SQUARE	0.98026	0.99472	0.9914
ADJ. R-SQUARE	0.97039	0.99208	0.9871

3.2. CESIUM-137 SOURCE

^{137}Cs sources were used to measure deadtime at a wide range of operating voltages—600 to 1200 V. ^{137}Cs is produced by nuclear fission in a nuclear reactor. It has a half-life of 30.08 years, and it is both a beta emitter and gamma emitter. The probability mode of decays is the following: A) about 94.7% by beta emission to ^{137m}Ba with decay energy of 514.03 KeV. B) ^{137m}Ba has a half-life of 153 seconds, and it decays into the ground state ^{137}Ba about 85.1% with 661.659 KeV.[22] Figure 4 shows the decay scheme of ^{137}Cs.

Figure 5a shows the deadtime vs. voltage measurements using ^{137}Cs sources for the wider range of voltages—600 to 1200 V. It is clearly seen that deadtime due to ^{137}Cs sources revealed similar behavior as measured from ^{204}Tl sources, though with different deadtime values. Table 3 shows the split sources and the calculated deadtime for the different applied voltage using ^{137}Cs. At 600 V, 650 V, 750 V, deadtimes were 190 μs, 105.45 μs, and 277.49 μs, respectively. Deadtime at 600 V using ^{137}Cs sources was 5% higher than the measured deadtime at 600 V using the ^{204}Tl sources; on the other hand, at 650 V deadtime using ^{137}Cs sources was significantly higher with 20.5%. At 700 V,

deadtime using ^{137}Cs sources was 5% lower than deadtime using ^{204}Tl sources. From 750 to 1050 V, it is observed that the decrease in deadtime revealed an exponential similar to ^{204}Tl sources experiments. The exponential fit at this range shows a coefficient of determination (R^2=0.98454). As the applied voltages were increased further, deadtime plateaued.
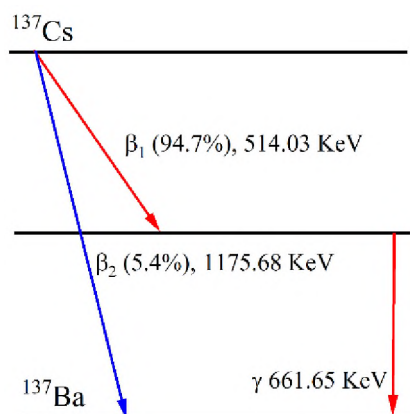
Figure 4. A schematic of the ^{137}Cs decay.

Table 3. Deadtime results for the applied voltages 600 to 1200 V. S1, S12, S2 are Source 1, Source 1 & 2 and Source 2 of Cesium-137, respectively. Deadtime was calculated using the non-paralyzing model.

VOL- TAGE (V)	S1 (CPS)	S12 (CPS)	S2 (CPS)	BKG (CPS)	DEADTIME (S)
600	591.39 ± 0.57	1089.86 ± 0.77	624.35 ± 0.58	0.14 ± 0.00	1.90e-04 ± 7.56e-07
610	605.16 ± 0.57	1115.29 ± 0.78	646.64 ± 0.59	0.17 ± 0.00	1.95e-04 ± 7.42e-07
620	715.18 ± 0.63	1257.70 ± 0.83	728.45 ± 0.63	0.24 ± 0.01	2.04e-04 ± 6.55e-07
630	987.75 ± 0.74	1662.10 ± 0.96	936.74 ± 0.72	0.29 ± 0.01	1.64e-04 ± 4.41e-07
640	990.67 ± 0.74	1686.28 ± 0.96	930.96 ± 0.71	0.31 ± 0.01	1.45e-04 ± 4.14e-07
650	924.31 ± 0.71	1707.70 ± 0.97	952.59 ± 0.72	0.32 ± 0.01	1.05e-04 ± 3.70e-07

Table 3. Deadtime results for the applied voltages 600 to 1200 V. S1, S12, S2 are Source 1, Source 1 & 2 and Source 2 of Cesium-137, respectively. Deadtime was calculated using the non-paralyzing model (cont.).

VOL-TAGE (V)	S1 (CPS)	S12 (CPS)	S2 (CPS)	BKG (CPS)	DEADTIME (S)
660	944.41 ± 0.72	1724.72 ± 0.97	888.21 ± 0.70	0.31 ± 0.01	6.81e-05 ± 3.35e-07
670	935.35 ± 0.72	1705.71 ± 0.97	869.93 ± 0.69	0.32 ± 0.01	6.45e-05 ± 3.38e-07
680	869.93 ± 0.69	1651.37 ± 0.95	818.53 ± 0.67	0.32 ± 0.01	2.64e-05 ± 3.29e-07
690	849.92 ± 0.68	1607.71 ± 0.94	814.24 ± 0.67	0.32 ± 0.01	4.20e-05 ± 3.51e-07
700	855.42 ± 0.68	1399.72 ± 0.88	881.72 ± 0.69	0.34 ± 0.01	2.77e-04 ± 6.79e-07
750	959.95 ± 0.73	1557.57 ± 0.93	989.98 ± 0.74	0.39 ± 0.01	2.58e-04 ± 5.90e-07
800	1058.15 ± 0.76	1743.53 ± 0.98	1076.19 ± 0.77	0.39 ± 0.01	2.09e-04 ± 4.72e-07
850	1112.75 ± 0.78	1880.39 ± 1.02	1134.34 ± 0.79	0.42 ± 0.01	1.73e-04 ± 3.97e-07
900	1165.28 ± 0.80	1971.50 ± 1.04	1179.11 ± 0.80	0.50 ± 0.01	1.61e-04 ± 3.65e-07
950	1199.31 ± 0.81	2012.33 ± 1.05	1219.45 ± 0.82	2.70 ± 0.03	1.66e-04 ± 3.59e-07
1000	1230.46 ± 0.82	2079.25 ± 1.07	1256.23 ± 0.83	2.02 ± 0.03	1.57e-04 ± 3.38e-07
1050	1254.48 ± 0.83	2118.65 ± 1.08	1305.68 ± 0.85	10.65 ± 0.07	1.60e-04 ± 3.30e-07
1100	1288.00 ± 0.84	2156.02 ± 1.09	1333.43 ± 0.86	13.62 ± 0.08	1.62e-04 ± 3.26e-07
1150	1319.07 ± 0.85	2209.92 ± 1.10	1359.38 ± 0.86	13.99 ± 0.08	1.55e-04 ± 3.11e-07
1200	1339.27 ± 0.86	2215.37 ± 1.10	1365.60 ± 0.87	12.75 ± 0.08	1.61e-04 ± 3.17e-07

Next, the differences in deadtime results, specifically at 650 V between ^{137}Cs sources and [204]Tl sources, prompted us to investigate this range in more detail. Figure 5c shows that deadtime from 600 to 620 V increased slightly and then dropped sharply to reach the lowest deadtime of 26.41 μs at 680 V. It is worth noting that the lowest deadtime for [204]Tl sources was at 670 V, while for the ^{137}Cs sources, lowest was at 680 V. This small shift can be attributed to the fact that ^{137}Cs is both a beta and gamma emitter. After 680 V,

deadtime increased slightly to 42.01 μs at 690 V. Further, deadtime increased significantly at 700 V to reach 277.49 μs, which is the highest observed deadtime for the ^{137}Cs experiment. It is also worth noting that deadtimes for 680 and 690 V were below 50 μs unlike with ^{204}Tl sources where deadtimes were above 100 μs for the same applied voltages.

Henceforth, it is concluded that there are three distinct deadtime regions in the examined broad range of voltages: I) Region 1: lower voltages (600 to 700 V) where deadtime decreases rapidly then increases. II) Region 2: middle voltages (750 to 1050 V) where deadtime shows a decreasing exponential behavior. III) Region 3: higher voltages (1100 to 1200 V) where deadtime reveals a plateau behavior, as shown in Figure 5a. On the other hand, count rates showed the opposite behavior to deadtime in region 1 & 2, increasing rather than decreasing with increasing voltages. Nonetheless, count rates in region 3 showed a slight increase rather than a plateau, as indicated in Figure 5b. Furthermore, the exponential fits and the parameters for S1, S12, S2 in region two are presented in Table 4

Figure 5d shows counts vs. voltage for region 1. One can notice that there is a slight increase in the number of counts from 600 V to 620 V, followed by a significant increase at 630 V and then it plateaued up to 670 V. In the plateau region, a higher number of counts were recorded using ^{137}Cs sources compared to ^{204}Tl sources. A decrease in observed counts followed the plateau region where the calculated deadtime was at a maximum at 700 V for the ^{137}Cs sources.
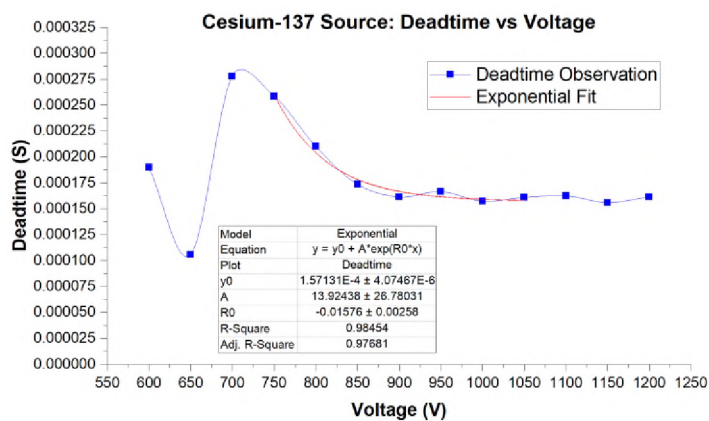
(a)
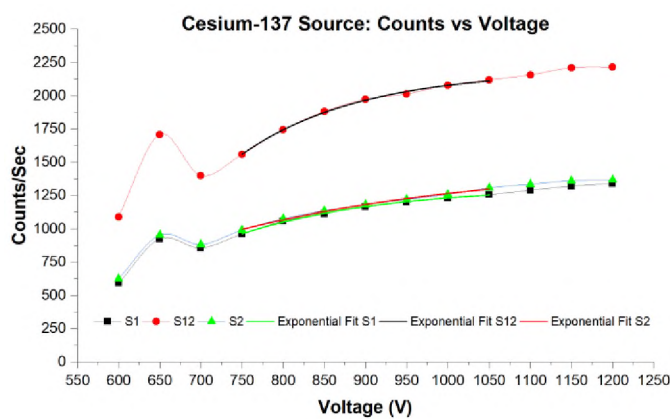
(b)
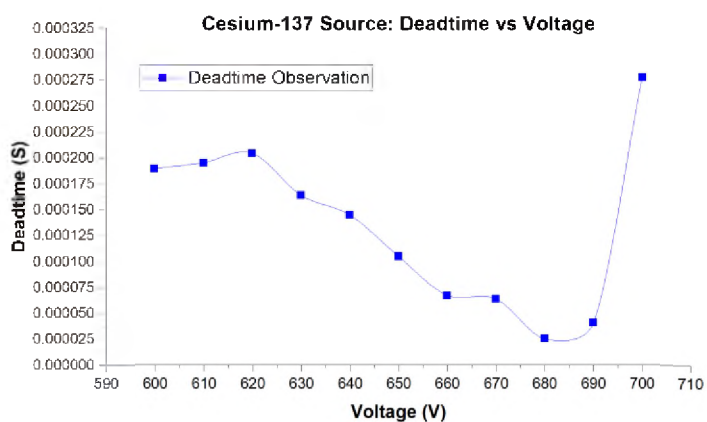
(c)

Figure 5. a) Deadtime vs. voltage for the ^{137}Cs source for the broad range of voltages. Parameters of the exponential fit are shown in the table under the deadtime curve. The parameters were generated using Origin software version (2019b). b) Counts vs. voltage with exponential fits imposed on the curves. c) Deadtime vs. voltage from 600-700 V range. d) Counts vs. voltage for the ^{137}Cs for the narrow voltages range.
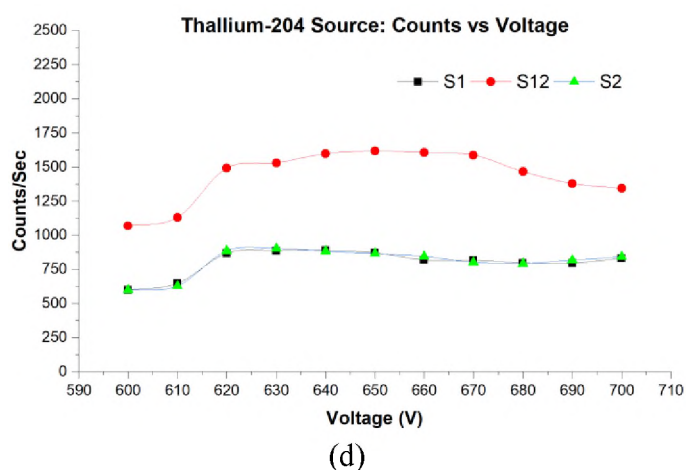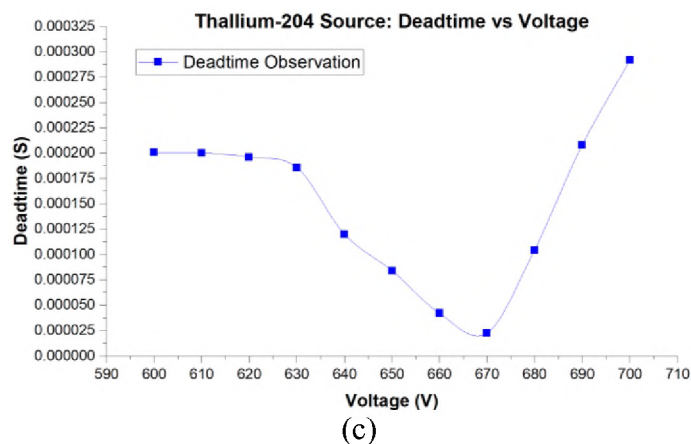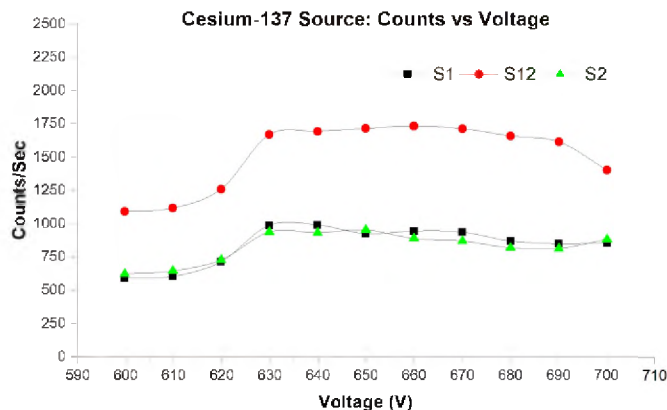
(d)

Figure 5. a) Deadtime vs. voltage for the ^{137}Cs source for the broad range of voltages. Parameters of the exponential fit are shown in the table under the deadtime curve. The parameters were generated using Origin software version (2019b). b) Counts vs. voltage with exponential fits imposed on the curves. c) Deadtime vs. voltage from 600-700 V range. d) Counts vs. voltage for the ^{137}Cs for the narrow voltages range (cont.).

Table 4. Parameters of the exponential model fit of Figure 5b using Cesium-137 S1, S12, S2. The table was generated through exponential curve fitting analysis using Origin software version (2019b).

MODEL	EXPONENTIAL		
EQUATION	$y = y_0 + A * e^{(R_0 * x)}$		
SOURCE	S1	S12	S2
Y0	1316.135 ± 14.99	2191.399 ± 24.16447	1486.62 ± 81.33
A	-24934.86 ± 8515.02	$-109809.37 \pm 47646.2833$	-5255.24 ± 2394.57
R0	$-0.0056 \pm 4.99e\text{-}4$	$-0.00688 \pm 6.143e\text{-}4$	$-0.0031 \pm 8.117e\text{-}4$
R-SQUARE	0.99846	0.99787	0.99538
ADJ. R-SQUARE	0.9977	0.9968	0.99307

3.3. SODIUM-22 SOURCE

^{22}Na sources were used to measure deadtime at a wide range of voltages—600 to 1150 V. Again operating voltages above 1200 V were not investigated to prevent any permanent damage to the GM, hence, 1150 V was the last investigated voltage for ^{22}Na. Sodium-22 has a half-life of 2.6018 years, and it is a positron-emitting isotope. ^{22}Na is a human-made isotope by the bombardment of aluminum target or high purity magnesium with protons.[23] ^{22}Na decays to an excited state of neon with a 9.5% probability via electron capture (EC) with a decay energy of 1567.67 KeV. However, it decays mainly via positron emission (90.33%) with decay energy of 545.67 KeV, as can be seen in Figure 6. After only 3.7 picoseconds, the excited neon decays by emitting a 1274.54 KeV gamma.

Figure 7a shows the deadtime vs. voltage measurements using ^{22}Na sources for the wider range of voltages of 600 to 1200 V. Additionally, the exponential model fit parameters are provided under the curve. Table 5 shows CPS for each source and the calculated deadtime at each applied voltage. The deadtime behavior at the lower voltages for ^{22}Na showed behavior similar ton ^{137}Cs and ^{204}Tl sources. However, there was a minor shift in the outcomes at this range. Contrary to deadtime results of ^{137}Cs and ^{204}Tl where the maximum recorded deadtimes were at 700 V, the maximum calculated deadtime for ^{22}Na in the wider range was 257.98 μs at 750 V. The minor shift in the highest calculated deadtime for ^{22}Na at 750 V can be attributed to the fact that ^{22}Na is a positron-emitting isotope. Since deadtime for ^{22}Na at 700 V was also lower than deadtime at 600 V, we selected to investigate the narrow operating voltages from 650 to 750 V instead of 600 to 700 V.
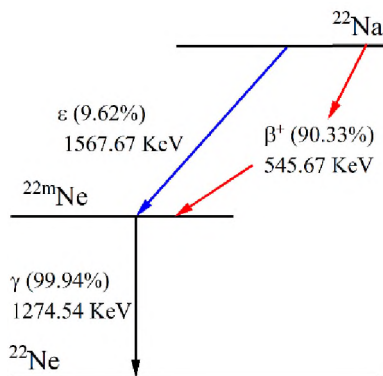
Figure 6. A schematic ^{22}Na decay.

Furthermore, deadtime at the operating voltages of 750 to 1050 V followed the same exponential decrease behavior. The exponential fit exhibited a coefficient of determination (R^2=0.99385), as can be seen in Figure 7b. The R-square of the exponential fit for ^{22}Na was higher than that of ^{137}Cs and ^{204}Tl. This can be explained by the fact that the starting point for the exponential fit was 750 V rather than 700 V. At higher voltages, 1100 and 1150 V, the calculated deadtimes were observed to be steadily increasing rather than showing the plateau behavior comparable to the ^{137}Cs and ^{204}Tl experiments. However, only two measurements are not sufficient to draw a conclusion to whether an increasing or plateau behavior is to be observed. The missing measurement at 1200 V would have confirmed the progressive increasing or plateauing behavior in this region.

Furthermore, it can be seen from Figure 7b that the count rates at each applied voltage using ^{22}Na were higher than the observed count rates using ^{137}Cs and ^{204}Tl. The count rate behavior for ^{22}Na followed the same pattern as for ^{137}Cs and ^{204}Tl. Table 6 shows the parameters of the exponential fits for counts at middle voltages for S1, S12, and S2.

Table 5. Deadtime results at operating voltages from 600 to 1200 V. S1, S12, S2 are Source 1, Source 1 & 2 and Source 2 of Sodium-22, respectively. Deadtime was calculated using the non-paralyzing model.

VOL-TAGE (V)	S1 (CPS)	S12 (CPS)	S2 (CPS)	BKG (CPS)	DEADTIME (S)
600	623.48 ± 0.58	1199.82 ± 0.81	724.41 ± 0.63	0.14 ± 0.00	1.84e-04 ± 6.71e-07
650	959.61 ± 0.73	1816.09 ± 1.00	1097.42 ± 0.78	0.32 ± 0.01	1.29e-04 ± 3.67e-07
660	929.47 ± 0.71	1830.89 ± 1.00	1065.83 ± 0.76	0.17 ± 0.00	9.04e-05 ± 3.29e-07
670	872.54 ± 0.69	1793.95 ± 0.99	996.40 ± 0.74	0.24 ± 0.01	4.48e-05 ± 3.04e-07
680	839.82 ± 0.68	1764.89 ± 0.99	939.34 ± 0.72	0.29 ± 0.01	8.94e-06 ± 2.91e-07
690	832.63 ± 0.68	1596.55 ± 0.94	913.802 ± 0.71	0.31 ± 0.01	1.07e-04 ± 4.05e-07
700	857.24 ± 0.69	1571.25 ± 0.93	908.06 ± 0.71	0.34 ± 0.01	1.39e-04 ± 4.44e-07
710	877.32 ± 0.69	1513.23 ± 0.91	938.18 ± 0.72	0.31 ± 0.01	2.20e-04 ± 5.56e-07
720	907.80 ± 0.71	1505.05 ± 0.91	983.32 ± 0.73	0.32 ± 0.01	2.71e-04 ± 6.29e-07
730	935.71 ± 0.72	1530.81 ± 0.92	1019.66 ± 0.75	0.32 ± 0.01	2.84e-04 ± 6.39e-07
740	955.96 ± 0.72	1568.76 ± 0.93	1044.12 ± 0.76	0.32 ± 0.01	2.75e-04 ± 6.13e-07
750	975.47 ± 0.73	1615.62 ± 0.94	1064.31 ± 0.76	0.39 ± 0.01	2.57e-04 ± 5.72e-07
800	1062.51 ± 0.76	1837.12 ± 1.01	1171.41 ± 0.80	0.39 ± 0.01	1.93e-04 ± 4.31e-07
850	1125.76 ± 0.79	1982.75 ± 1.04	1234.43 ± 0.82	0.42 ± 0.01	1.61e-04 ± 3.64e-07
900	1168.58 ± 0.80	2062.00 ± 1.07	1301.54 ± 0.85	0.50 ± 0.01	1.60e-04 ± 3.49e-07
950	1198.30 ± 0.81	2125.34 ± 1.08	1326.16 ± 0.85	2.70 ± 0.03	1.48e-04 ± 3.22e-07
1000	1238.27 ± 0.82	2187.16 ± 1.10	1379.59 ± 0.87	2.02 ± 0.03	1.50e-04 ± 3.16e-07
1050	1272.30 ± 0.84	2237.94 ± 1.11	1411.80 ± 0.88	10.65 ± 0.07	1.47e-04 ± 3.00e-07
1100	1295.83 ± 0.84	2261.37 ± 1.12	1451.83 ± 0.89	13.62 ± 0.08	1.54e-04 ± 3.04e-07
1150	1317.95 ± 0.85	2278.95 ± 1.12	1467.29 ± 0.90	13.99 ± 0.08	1.57e-04 ± 3.05e-07

Next, Figure 7c shows deadtime vs. voltage for the narrow range—650 to 750 V. It is observed that from 650 to 680 V, deadtime is rapidly decreasing. Similar to the ^{137}Cs experiment, the lowest deadtime was at 680 V with a deadtime of only 8.94 µs. This is the lowest calculated deadtime obtained from using the radioactive sources in this study. After 680 V, deadtime started to increase up to 730 V where deadtime peaked for the [22]Na sources at 284.31 µs. It is noteworthy that the lowest calculated deadtimes for [22]Na compared to ^{137}Cs and [204]Tl were 66.14% and 60.14% lower, respectively, whereas the highest deadtimes were 2.4% higher and 2.53% lower, respectively. It is, therefore, concluded that at lower voltages, the lowest deadtime using [22]Na is significantly lower than that of the calculated deadtimes using ^{137}Cs and [204]Tl.

Lastly, counts at lower applied voltages for [22]Na showed different behavior than for ^{137}Cs and [204]Tl, as can be seen in Figure 7d. From 650 to 680 V, there was slight decrease in count numbers followed by a sharper drop at 690 V. Afterward, there was a steady number of counts from 700 to 750 V.
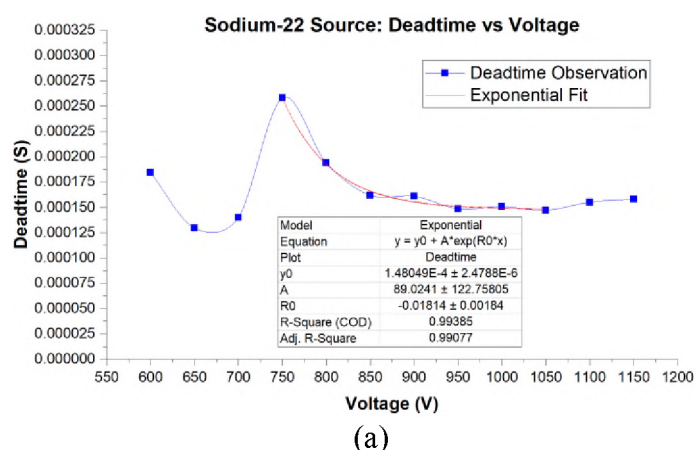
(a)

Figure 7. a) Deadtime vs. voltage for the [22]Na source from 600-1150 V. Parameters of the exponential fit are shown in the table under the deadtime curve. The parameters were generated using Origin software version (2019b). b) Counts vs. voltage with exponential fits imposed on the curves. c) Deadtime vs. voltage for the [22]Na source from 650-750 V range. d) Counts vs. voltage for the [22]Na for the narrow voltages range.
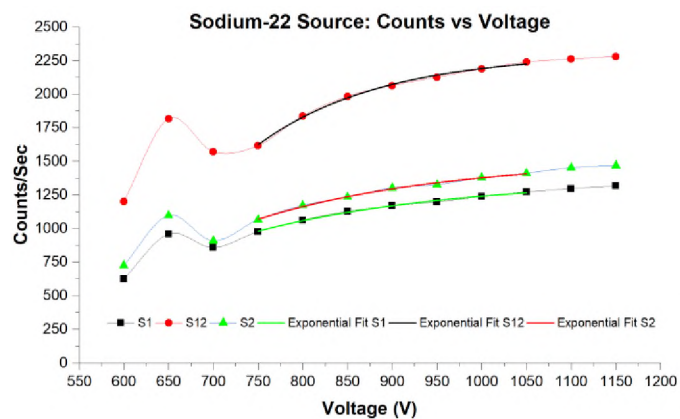
(b)
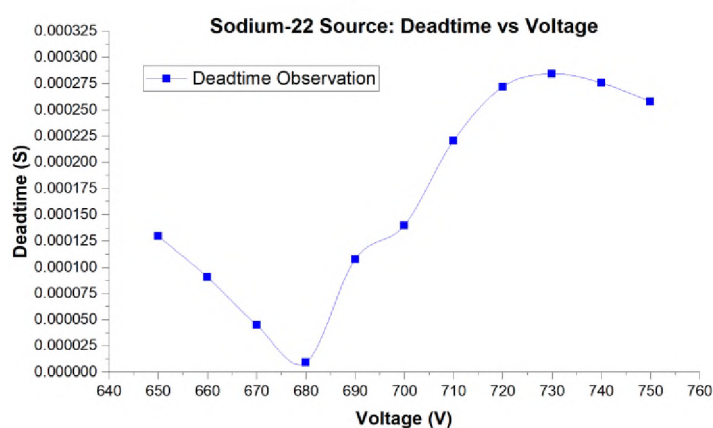
(c)
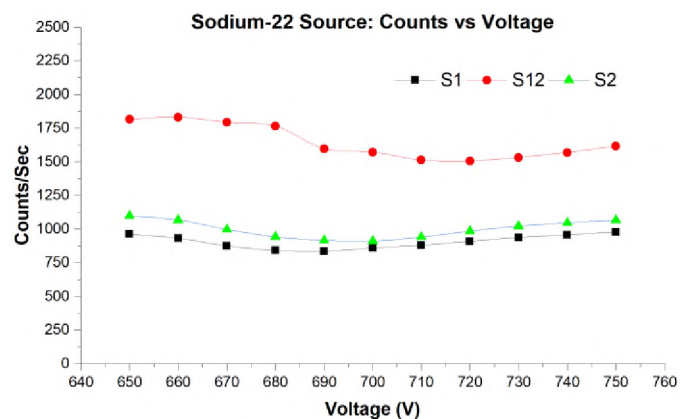
(d)

Figure 7. a) Deadtime vs. voltage for the ^{22}Na source from 600-1150 V. Parameters of the exponential fit are shown in the table under the deadtime curve. The parameters were generated using Origin software version (2019b). b) Counts vs. voltage with exponential fits imposed on the curves. c) Deadtime vs. voltage for the ^{22}Na source from 650-750 V range. d) Counts vs. voltage for the ^{22}Na for the narrow voltages range (cont.).

Table 6. Exponential model fit curve parameters of S1, S12, S2 for Sodium-22 as can be seen from Figure 7b. The table was generated through exponential curve fitting analysis using Origin software version (2019b).

MODEL	EXPONENTIAL		
EQUATION	$y = y_0 + A * e^{(R_0 * x)}$		
SOURCE	S1	S12	S2
Y0	1363.77 ± 34.86	2302.59 ± 28.09	1515.34 ± 42.30
A	-11618.9 ± 5675.0	-150918.7 ± 76795.4	-15297.8 ± 8330.1
R0	$-0.0045 \pm 7.544e\text{-}4$	$-0.0072 \pm 7.158e\text{-}4$	$-0.0047 \pm 8.326e\text{-}4$
R-SQUARE	0.99626	0.99718	0.99549
ADJ. R-SQUARE	0.99439	0.99577	0.99323

3.4. MANGANESE-54 SOURCE

Lastly, ^{54}Mn sources were used to compute deadtime from 600 to 1200 V. ^{54}Mn has a half-life of 312.2 days. The primary decay mode for ^{54}Mn is via EC with a 99.99% probability, followed by photon emission of 834.85 KeV. The daughter isotope is a stable ^{54}Cr. With a lower probability mode of beta decay (0.000093%), ^{54}Mn decays to ^{54}Fe, which is also a stable isotope. Nonetheless, with even lower probability mode of decay (5.7E-7%), ^{54}Mn decays to ^{54}Cr via positron emission.[22, 23, 24] Figure 8 shows the reduced decay scheme of ^{54}Mn.

Table 7 shows the number of counts of S1, S12, and S2 of ^{54}Mn and its calculated deadtimes. It is observed that the number of CPS is significantly lower than the CPS from ^{204}Tl, ^{137}Cs, and ^{22}Na split sources. The lowest CPS of S12 using ^{54}Mn sources at 600 V was 94.55%, 94.66%, 95.15% lower than ^{204}Tl, ^{137}Cs, and ^{22}Na, respectively. At the lower

voltages, the maximum computed deadtime for ^{54}Mn was 1.65 ms at 600 V, followed by an exponential decrease to reach the lowest deadtime of 486 μs at 1050 V. Although the CPS of S12 were steadily increasing at higher voltages, deadtime showed negative values in 1100 to 1150 V range. In addition, at 1200 V, deadtime had a very high value. The reason for the negative and high deadtimes at these high voltages is due to the high number of observed counts due to background radiation. The BKG showed a rapid increase in the number of counts from 1100-1200 V. When the GM counter registered even higher amounts of BKG events at 1200 V, the calculated deadtime showed significantly higher value with 11.1 microseconds. Figure 9a. illustrates the calculated deadtimes of ^{54}Mn radioactive sources as a function of applied voltages.
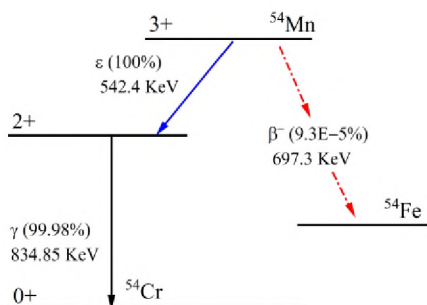
Figure 8. A reduced schematic ^{54}Mn decay.[25]

Table 7. Deadtime results at operating voltages from 600 to 1200 V. S1, S12, S2 are Source 1, Source 1 & 2 and Source 2 of Manganese-22, respectively. Deadtime was calculated using the non-paralyzing model.

VOL-TAGE (V)	S1 (CPS)	S12 (CPS)	S2 (CPS)	BKG (CPS)	DEADTIME (S)
600	29.96 ± 0.12	58.15 ± 0.17	31.27 ± 0.13	0.17 ± 0.01	1.64e-03 ± 5.07e-05
600	29.96 ± 0.12	58.15 ± 0.17	31.27 ± 0.13	0.17 ± 0.01	1.64e-03 ± 5.07e-05

Table 7. Deadtime results at operating voltages from 600 to 1200 V. S1, S12, S2 are Source 1, Source 1 & 2 and Source 2 of Manganese-22, respectively. Deadtime was calculated using the non-paralyzing model (cont.).

VOL-TAGE (V)	S1 (CPS)	S12 (CPS)	S2 (CPS)	BKG (CPS)	DEADTIME (S)
650	67.39 ± 0.19	123.98 ± 0.26	67.24 ± 0.19	0.32 ± 0.01	1.24e-03 ± 1.77e-05
700	74.21 ± 0.20	138.16 ± 0.27	74.91 ± 0.20	0.36 ± 0.01	1.03e-03 ± 1.48e-05
750	78.29 ± 0.20	144.38 ± 0.28	78.23 ± 0.20	0.39 ± 0.01	1.04e-03 ± 1.40e-05
800	80.09 ± 0.21	150.08 ± 0.28	80.22 ± 0.21	0.46 ± 0.01	8.19e-04 ± 1.26e-05
850	83.63 ± 0.21	156.65 ± 0.29	83.49 ± 0.21	0.48 ± 0.01	7.69e-04 ± 1.18e-05
900	86.33 ± 0.21	161.93 ± 0.29	86.36 ± 0.21	0.68 ± 0.01	7.29e-04 ± 1.11e-05
950	86.75 ± 0.21	165.16 ± 0.30	87.62 ± 0.22	0.54 ± 0.01	6.08e-04 ± 1.06e-05
1000	88.50 ± 0.22	167.92 ± 0.30	88.15 ± 0.22	0.89 ± 0.02	5.36e-04 ± 1.01e-05
1050	88.88 ± 0.22	168.36 ± 0.30	88.58 ± 0.22	2.10 ± 0.03	4.85e-04 ± 9.68e-06
1100	89.22 ± 0.22	167.66 ± 0.30	87.58 ± 0.22	11.82 ± 0.08	-2.24e-04
1150	90.18 ± 0.22	169.21 ± 0.30	88.33 ± 0.22	17.28 ± 0.09	-7.38e-04
1200	89.83 ± 0.22	168.22 ± 0.30	90.04 ± 0.22	62.17 ± 0.18	1.11e-02

Next, it is observed from Figure 9b that the number of counts at low voltages showed different behavior than from the other sources. However, in the middle voltages range, counts demonstrated a similar exponential increase behavior to that of the other sources. Table 8 shows the parameters of the exponential model fits. At 600 V, counts for S12 were very low, followed by a significant increase of counts at 650 V. Then counts followed a steady exponential increase until 1050 V. Counts at higher operating voltages plateaued from 1100 to 1200 V; although, deadtimes were out of characteristics at these higher voltages.

(a)

(b)
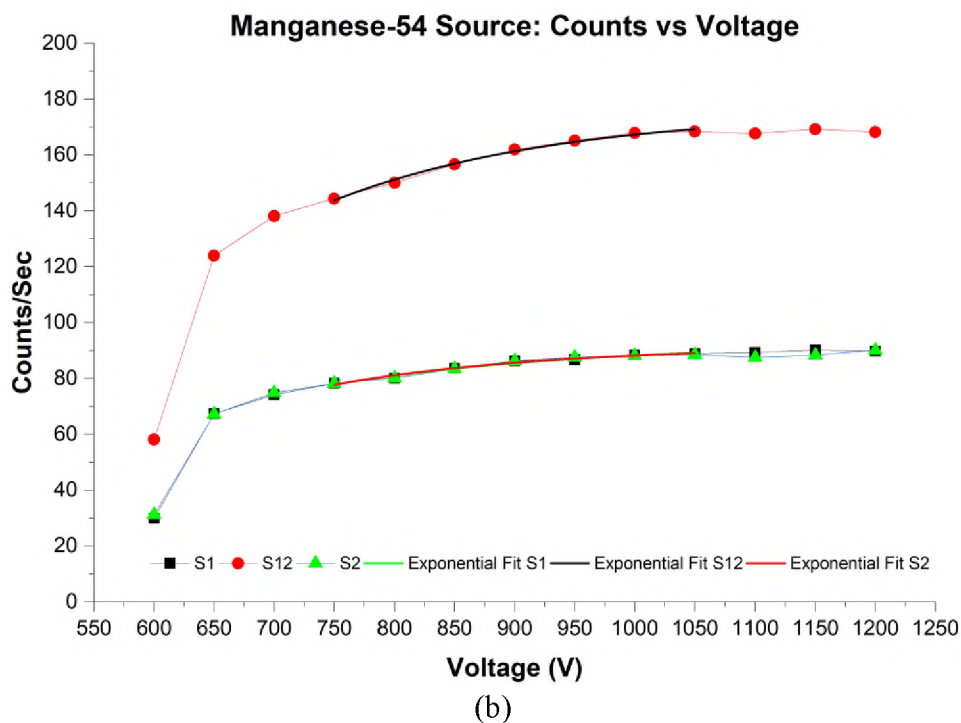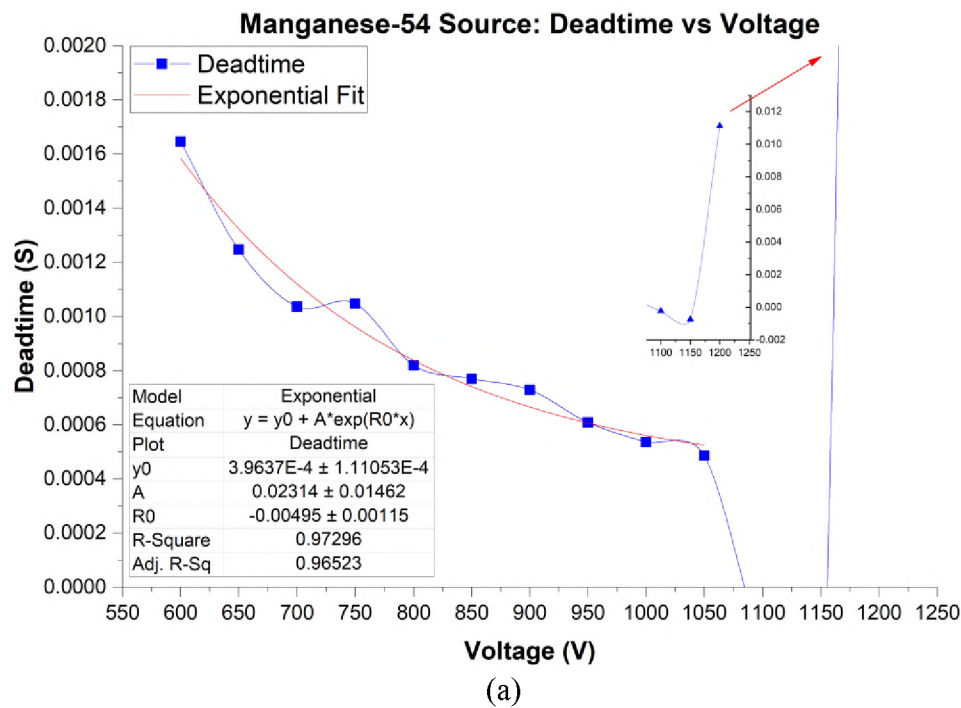
Figure 9. a) Deadtime vs. voltage for the [54]Mn source from 600-1200 V. Parameters of the exponential fit are shown under the deadtime curve. The parameters were generated using Origin software version (2019b). b) Counts vs. voltage with exponential fits being superimposed on the curves.

Table 8. Exponential model fit parameters of S1, S12, S2 for Manganese-54 Source (Figure 9b data). The parameters are generated by curve fitting analysis using Origin software version (2019b).

MODEL	EXPONENTIAL		
EQUATION	$y = y_0 + A * e^{(R_0 * x)}$		
Y0	92.53 ± 2.7589	175.84 ± 3.22	91.49 ± 2.15
A	-588.87 ± 688.42	-1689.72 ± 1200.67	-1007.45 ± 1288.91
R0	-0.0049 ± 0.001	-0.005 ± 0.001	-0.0057 ± 0.001
R-SQUARE	0.98023	0.99301	0.979
ADJ. R-SQUARE	0.97035	0.98951	0.9685

The experiment utilizing the ^{54}Mn sources resulted in negative values for deadtime, at high voltages due to the small number of counts. Deadtime measurements using ^{54}Mn sources could be improved by either using stronger sources by placing the sources on shelf number 1 of the rack instead of shelf number 2. However, for the purpose of evaluating all the sources in similar geometry, the ^{54}Mn sources were placed precisely on the second shelf, where other sources were located while performing the experiments. Figure 10 shows a comparison of fractional deadtimes of the sources used in this study. The ^{204}Tl, ^{137}Cs, and ^{22}Na sources from 800 V and above (including GM operating region) are within the acceptable range of fractional deadtime—at least 20% and does not exceed 40%. However, for the ^{54}Mn sources, fractional deadtimes were always below 20%, excluding the high fractional deadtime at 1200 V of 187%. Hence, it is determined that the data generated using ^{54}Mn sources are not reliable and should not be used to draw further inferences.
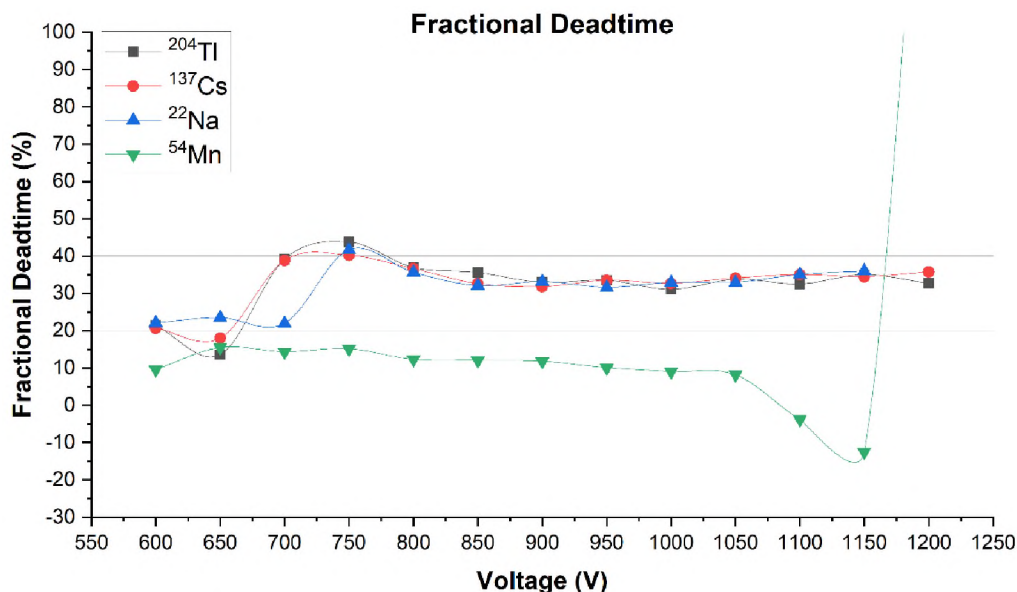
Figure 10. Fractional deadtimes of ^{204}Tl, ^{137}Cs, ^{22}Na, and ^{54}Mn sources as a function of applied voltages with reference lines at 20 and 40%.

4. CONCLUSIONS

The new data collected and reported is quite revealing. It shows a different behavior of deadtime phenomena, which is not previously discussed in the literature. At low voltage range, a peculiar yet repeatable general deadtime behavior was observed for various radiation sources tested in the experimental research for the GM counting system. After a range of almost constant values, deadtime dropped to a minimum at 650-680 V range before increasing back to a maximum value. The observed peak of deadtime value is observed in the range of 700-750 V. Subsequent to the maximum value, there seems to be an exponential drop in the deadtime, reaching a low asymptotic value during the manufacturer's suggested operating voltage range of GM counter use (850-1000 V). Furthermore, we also investigated higher operating voltages (1000-1200 V) but did not surpass 1200 V to ensure the safe operation of the GM detector. Therefore, we did not

observe the discharge region, where counts increase rapidly. Overall, this behavior of the GM detector's deadtime has not been reported earlier in the literature.

The observed fall followed by the rapid rise and final exponential fall of deadtime can have a plausible explanation in light of the general behavior of gas-filled detector's regions of gaseous ionization and charge multiplication.
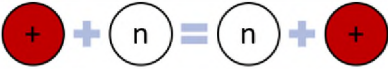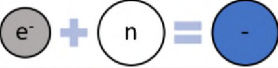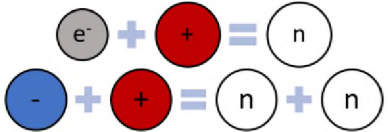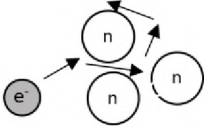
Figure 11. The figure shows different types of interactions of charged species in a gas filled detector. In the left-hand side of the represented equations are the interacting special while the right-hand side are the product of these interactions. The + and − circles represent the positive and negative ions, respectively. The n circles represent a neutral atom or a molecular. The e- circle represents the electrons.[26]

At very low voltage, after initial ionizations take place, free electrons and positive ions drift and diffuse before being collected. At these low voltages, the count rate is low, and not all the events are recorded mainly due to the recombination of positive ions and electrons. Figure 11 shows an illustration of the different types of interactions of charged species. As the voltage increases from these minimal values, there is an observed increase in the count rates and a decrease in the deadtime. The reduced collection time with

increasing voltage is the reason for deadtime reduction. A minimum deadtime is reached at the point when the collection time is minimum without any significant charge multiplication. Increasing the voltage further results in charge multiplication, which is caused by the high drift velocity and consequently impacts the energy of electrons. Since each generated pulse is the sum of a larger number of charge carriers, the collection time increases; therefore, deadtime increases. This positive relationship between the operating voltage and deadtime is observed due to the loss of proportionality. Due to the loss of proportionality, no further increase in deadtime is possible. After the maximum is reached, deadtime starts to decrease with increasing the applied voltages with an exponential behavior. Increasing the voltage further results in no significant additional charge multiplication. On the other hand, increasing the voltage reduces the collection time; therefore, deadtime is reduced. The well-known exponential behavior is observed in this range. At 900 V, which is the recommended operating voltage of the detector, a low asymptotic value of deadtime is observed.

This level of detailed GM deadtime analysis has not been reported in the literature. It is hoped that this work will further enhance the radiation measurement's community understanding of the phenomenon and remedial strategy for dealing with detector deadtime problems.

REFERENCES

[1]   Knoll, G.F. *Radiation Detection and Measurement*. (John Willey & Sons, Ltd, 2010).

[2]   Muller, J.W. Dead-time problems. *Nucl. Instrum. Methods* 112, 47-57 (1973).

[3]   Akyurek, T., Tucker, L.P., Liu, X., Usman, S. Portable spectroscopic fast neutron probe and 3He detector dead-time measurements. *Prog. Nucl. Energy* 92, 15-21 (2016).

[4]   Akyurek, T., Yousaf, M., Liu, X. & Usman, S. GM counter deadtime dependence on applied voltage, operating, temperature and fatigue. Prog. Nucl. Energy 73, 26-35 (2015).

[5]   Usman, S., Patil, A. Radiation detector deadtime and pile up: A review of the status of science, *Nucl. Eng. Tec.* 50, 1006-1016 (2008).

[6]   Tsoulfanidis, N., Landsberger, S. Detector dead-time correction and measurement of dead time. *In Measurement and Detection of Radiation*, 63-66 (CRC Press, 2015).

[7]   Muller, J.W. *A simple derivation of the Takacs formula.* (Bureau International des Poids et Mesures, 1988).

[8]   Muller, J.W. Generalized dead times, *Nucl. Instrum. Methods Phys. Res. Sect. A Accel. Spectrom. Detect. Assoc. Equip.* 301, 543-551 (1991).

[9]   Albert, G.E., Nelson, L. Contributions to the statistical theory of counter data, *Ann. Math. Stat.* 24, 9-22 (1953).

[10]   Lee, S.H., Gardner, R.P. A new G-M counter dead time model, *Appl. Radiat. Isot.* 53, 731-737 (2000).

[11]   Hou, G., Gardner, R.P. A new G-M counter hybrid dead-time correction model, *Radiat. Phys. Chem.* 116, 125-129 (2015).

[12]   Patil, A., Usman, S. Measurement and application of paralysis factor for improved detector dead-time characterization, *Nucl. Technol.* 165, 249-256 (2009).

[13]   Disk Source Sets. www.spectrumtechniques.com (2019).

[14]   Model 44-7 Alpha-Beta-Gamma Detector. www.ludlums.com (2019).

[15]   142A/B/C Preamplifiers. www.ortec-online.com (2019).

[16]   Model 3125 0-2/0-5 kV Dual H.V. Power. www.nuclearphysicslab.com (2019).

[17]   TBS2000 Digital Storage Oscilloscope. www.tek.com (2019).

[18] Almutairi, B., Alam, S., Akyurek, T., Goodwin, C. & Usman, S. Experimental evaluation of the deadtime phenomenon for GM detector: Pulse Shape Analysis. In preparation to be submitted in *Scientific Reports* (2020).

[19] Model 570 Spectroscopy Amplifier. www.ortec-online.com (2019).

[20] Cardoso, J. M., Simões, J.B., Menezes, T., Correia, C.M.B.A. CdZnTe Spectra improvement through digital pulse amplitude correction using the linear sliding method. *Nucl. Intstr. and Meth.* 505, 334-337 (1999).

[21] Model 994 Dual Counter/Timer. www.ortec-online.com (2019).

[22] Table of Nuclides. www.iaea.org (2019).

[23] Radioisotope of Sodium-22. www.isotopes.gov (2019).

[24] Table of Radionuclides. www.nucleide.org (2019).

[25] Radionuclide Manganese-54. www.spectrumtechniques.com (2019).

[26] Knoll, G.F. *Radiation Detection and Measurement*. (John Willey & Sons, Ltd, 2000).

III. EXPERIMENTAL EVALUATION OF THE DEADTIME PHENOMENON FOR GM DETECTOR: PULSE SHAPE ANALYSIS

Bader Almutairi[a,b,c], Syed Alam[a], Cameron S. Goodwin[c], Shoaib Usman[a], Tayfun Akyurek[d]

[a]Mining and Nuclear Engineering, Missouri University of Science & Technology, Rolla, MO, 65401, USA

[b]Environment and Life Sciences Research Center, Kuwait Institute for Scientific Research, Kuwait City 13109, KUWAIT

[c]Rhode Island Atomic Energy Commission, 16 Reactor Rd., Narragansett, RI, 02882, USA

[d]Department of Physics, Faculty of Art and Science, Marmara University, 34722, Kadikoy, Istanbul, TURKEY

ABSTRACT

A detailed analysis of several pulse shape properties generated by a Geiger Mueller (GM) detector and its dependence on applied voltage is examined. The two-source method was utilized to measure deadtime of the counting system while simultaneously capturing pulse shape parameters on an oscilloscope. A wide range of operating voltages (600-1200 V) was investigated using three radioactive sources (^{204}Tl, ^{137}Cs, ^{22}Na). This study aims to investigate the relationship between operating voltage, pulse shape properties, and deadtime of the GM detector. Based on the collected data, it is found that deadtime decreases due to recombination processes while the pulse width increases due to low applied voltages. It is also observed that rise and fall time are at their highest at low voltages. This was due to the applied voltage was not strong enough. Therefore, the collection time and pulse tail are longer, which ultimately resulted in longer deadtime.

Increasing the voltage further would result in gas multiplication, where deadtime and pulse width are observed to be increasing. After reaching the maximum point of deadtime, it starts to exponentially decrease until a plateau is reached. In this region, it is observed that detector deadtime and operating voltage show a strong correlation with positive pulse width, rise and fall time, cycle mean, and area. Therefore, this study confirms the relationship between detector deadtime, operating voltage, and pulse shape properties.

1. INTRODUCTION

In 1908, Ernest Rutherford and Hans Geiger attempted to count the number of alpha particles emitted by a radium sample. To perform the task, they designed a simple apparatus where an individual alpha particle passing through a gas-filled tube (counter) is amplified due to ionization processes. With applying high voltages, a cascade of ions was created due to the passage of alpha particles. The ions are then attracted toward a central wire (anode) in the tube, which produced a pulse of electric charge that is counted by an electrometer.[1] The apparatus they used is now known as a 'proportional counter,' which operates on the gas multiplication principle. After twenty years, Geiger and his undergraduate student, Muller, improved the apparatus, which ultimately led to the invention of the Geiger-Muller (GM) counter. It does not detect only alpha particles but also beta and gamma rays; however, it does not differentiate which type of radiation it is detecting. GM counter has been widely used in radiation measurement applications since then.[2] The abundant use of the GM counter can be attributed to several key features, such as its simple, low-cost design, its ease of operation, and portability.

Furthermore, for the GM counter to detect and record two independent radiation incidents, there has to be a minimum time interval between two radiation events. In this short interval time, the detector is unresponsive (dead). Any radiation event that takes place within this short interval time will be lost (uncounted). Several studies have shown that the GM counter suffers from a large deadtime compared to other radiation detectors such as solid-state detectors and scintillators.[2, 3, 4] The large deadtime that the GM counter suffers from can be from a few microseconds to more than a few milliseconds.[5, 6] Moreover, the deadtime phenomenon in radiation detectors has been studied as early as the 1940s. Research on the deadtime phenomenon since then has recognized several factors that affect phenomenon, such as the detector's specifications and design, pulse processing of the detection measurement system, and operating conditions.[7] Mainly, two factors contribute toward the deadtime of a radiation detection system: (I) the inherent deadtime of the detector itself known as intrinsic deadtime, and (II) the collective deadtime that results from pulse processing instruments.[8]

The pulse processing electronics of a typical radiation detection system include a detector, preamplifier, amplifier, discriminator, counter, and multi-channel analyzer (MCA). Nonetheless, for the GM detector, the contribution factor of deadtime from the pulse processing electronics is negligible compared with the detector's processes. Hence, the intrinsic deadtime is the major contributor to the final deadtime for any GM counting system. Therefore, intrinsic deadtime is sufficient for deadtime correction measurements for the case of GM counter.

Due to the fact that radiation events are random, many radiation incidents go undetected due to the deadtime phenomenon. Subsequently, several deadtime models have been proposed for count rate corrections of the radiation detection system.

1.1. DEADTIME MODELS

For count rate correction consideration, there are two traditional deadtime models: (1) the paralyzing, and (2) non-paralyzing models. These two idealized models are employed extensively in the industry and academia. Both models were derived by Feller[9] and Evans.[10] The paralyzing model assumes that each radiation event taking place within the detector would extend the resolving time (deadtime). If a subsequent radiation event occurs within the extended time, it will not be detected--- the count is lost. For that reason, the paralyzing model is known as an extending type. For a radiation event to be counted, there has to be a minimum gap time between two radiation events so that the continuous paralysis of the detector system has lapsed. The proposed paralyzing model, henceforth, attempts to correct the measured count rates. The mathematical description of the paralyzing model is seen in Eq. (1.1).

$$m = n \ e^{-n\tau} \hspace{2cm} (1.1)$$

where n is the true count rate, m is the measured count rate, τ is deadtime. In contrast, the non-paralyzing model (known as non-extending type) is based on the assumption that each radiation event taking place within the detector will be followed by deadtime. However, when a subsequent interaction takes place during this deadtime, there is no extension of deadtime. Unlike the paralyzing model's assumption of continuous paralysis of the detector when a radiation event is detected, the non-paralyzing model assumes that the detector is

dead only for a fixed time following the detection of a radiation event. The mathematical expression for the non-paralyzing model is given in Eq. (1.2).

$$m = \frac{n}{(1 + n\,\tau)} \tag{1.2}$$

Further investigation of the deadtime phenomenon in 1978 resulted in a generalized deadtime model derived by Muller.[11, 12] By combining the fundamentals of the idealized models, a hybrid deadtime model was later developed by Albert and Nelson,[13] which, in turn, was enhanced by Lee and Gardner[14]. They used Manganese (^{56}Mn) radioactive source method for measuring deadtime. Along with the assumption that the non-paralyzing model precedes the paralyzing model, Lee and Gardner applied the least fitting square method on the data generated from their experiment. The mathematical expression of the hybrid model is given in Eq. (1.3). In an effort to improve the hybrid model further, Patil and Usman[6] proposed another modification by introducing a probability-based paralysis factor (f). The paralysis factor was proposed to be between 0 and unity. Eq. (1.4) shows the mathematical expression of their modified hybrid model.

$$m = \frac{n\,e^{-n\,\tau_P}}{1 + n\,\tau_N} \tag{1.3}$$

$$m = \frac{n\,e^{-n\,f\,\tau}}{1 + n\,\tau\,(1 - f)} \tag{1.4}$$

where τ_p is the paralyzing deadtime, τ_{np} is the non-paralyzing deadtime, τ is the total deadtime, and f is the probability-based paralysis factor. It is worth noting that if the f is set to 0, the modified hybrid model reduces to the non-paralyzing model, while if f is set to 1, equation 1.4 reduces to the paralyzing model. Additionally, if the f is set to 0.5, deadtime behavior will be lying between the paralyzing and non-paralyzing models. In

order to estimate f, Patil and Usman proposed a graphical technique. Details of the graphical technique is beyond the scope of this paper and can be found elsewhere.[6]

1.2. DEADTIME BEHAVIOR

It was pointed out that the two ideal deadtime models (paralyzing and non-paralyzing) are mathematical convenience rather than phenomenologically based.[6, 15] As discussed earlier,[8] non-paralyzing model is merely using the first term(s) of Taylor expansion of the paralyzing model. Yousaf et al.[15] developed a simulation code to test various deadtime models, ideal and hybrid. We programed the same comparison in MATLAB "Sim-Pulse V1.2" (version R2018b), to simulate a short decaying radioactive source (Barium, ^{137m}Ba, with a half-life of 153.12 s) to illustrate the various deadtime behaviors according to the deadtime models discussed in section 1.1. ^{137m}Ba is widely utilized for half-life measurement experiments. To demonstrate that the choice of model is significant only when the true count rate is high or the deadtime is long, three cases were simulated, as shown in Table 1. For GM counters where the deadtime is rather long, the choice of model is significant even at low count rates, but the general consensus is that GM behaves like an ideal non-paralyzing detector.[14] The behavior of other types of detectors must be carefully evaluated at high count rates before applying any count rate correction.

From Figure 1, it can be seen that when deadtime is low, there is little loss of counts (case 1), and the choice of model has no serious consequence. However, when deadtime is higher, all models diverge (Case 2 and 3). The paralyzing and non-paralyzing models always set the lowest and highest limits for count rate measurements, respectively. It is worth addressing that these traditional models have been applied commonly in radiation

detection.[16] Previous studies[6, 17, 18] have shown that true deadtime behavior falls somewhere between the idealized models.

Table 1. Total deadtimes used for simulations for each of the 3 cases. P stands for the Paralyzing model and NP for the non-paralyzing model. In Lee & Gardner's model, NP stands for the non-paralyzing model followed by paralyzing, whereas PN is the opposite.

Model	P	NP	Lee & Gardner (NP, PN)	Patil & Usman (NP, PN) (f =50%)
Case 1				
Total deadtime (μs)	10	10	5 + 5	50%
Case 2				
Total deadtime (μs)	200	200	100 + 100	50%
Case 3				
Total deadtime (μs)	1000	1000	500 + 500	50%
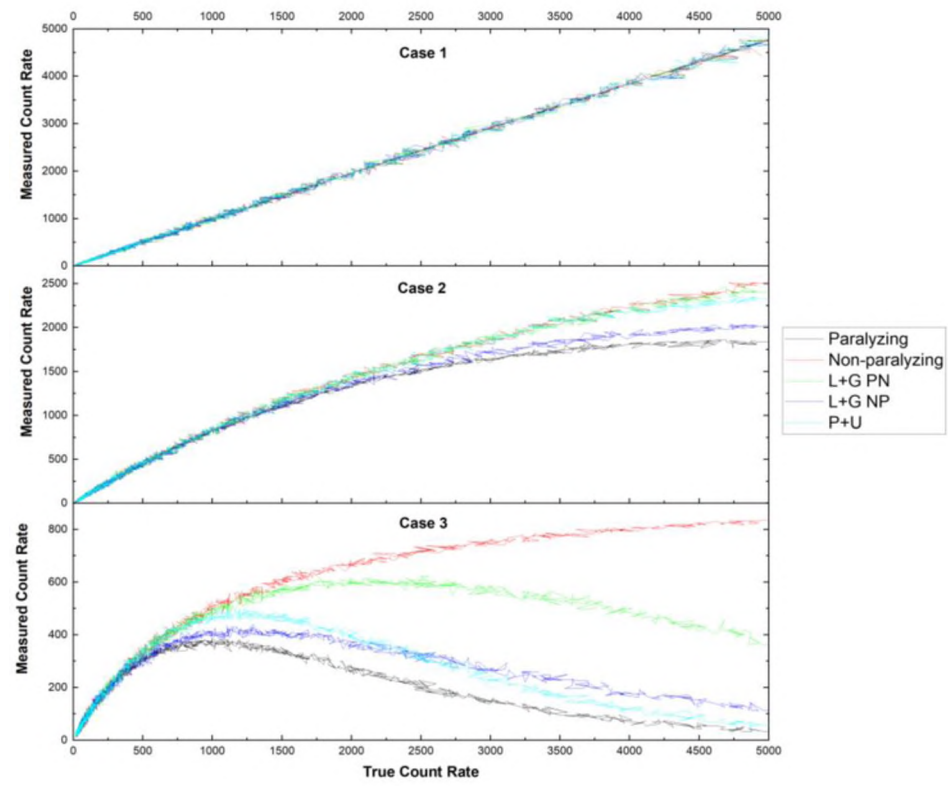
Figure 1. Different deadtime behaviors according to five models.

1.3. PULSE SHAPE CHARACTERISTICS

In the radiation measurement community, it is widely believed that the pulses produced in a GM detector carry no useful information due to the fact that the generated pulses have the same amplitude.[4, 16] However, this belief was recently questioned[7, 19] investigated pulse shape properties while varying applied voltages. It is worth noting that Akyurek and co-worker's[7] investigation of the pulse shape was performed to confirm the hypothesis that at low voltages, deadtime decreases with increasing voltages until a plateau is reached and after that, at higher voltages deadtime increases. Their study focused on pulse duration (pulse width) and the time interval between two pulses (gap time). The investigated operating voltages were in the range of 800 V. It was revealed that at low voltages, pulse width decreases with increasing operating voltage. This reduction of pulse width was attributed to smaller charge collection and hence reduced deadtime. Moreover, at higher operating voltages, the second pulse after a long width pulse was observed to be of short duration. This reduction in the second pulse was attributed to smaller charge production for the second event during the recovery time. Although the initial work by Akyurek and co-worker's[7] was very interesting, it lacked the analysis of several other important pulse shape properties such as amplitude, fall time, rise time, area, and positive pulse width. It is also worth noting that the generated pulses in their study were manually captured using an oscilloscope. The use of automatic measurements offered by an advanced oscilloscope would have shown more details on pulse shape properties.

In an effort to study the generated pulse properties from a GM counter even further, we designed an experiment that used two different radioactive sources: Cobalt-60 (60Co) and Cesium-137 (137Cs). The details of the study were discussed elsewhere.[19] The

recommended operating voltage specified by the manufacturer for that particular GM detector (Ludlum, model 133-2) was 550 V. A wide range of voltages--- 300 V to 1000 V was examined without reaching too high. Nonetheless, we did not examine the pulses at higher voltages due because the high voltage would possibly damage the detector. It was concluded that pulses from both of the radioactive sources behaved similarly in which pulse width and fall time were exponentially decreasing with increasing the operating voltages. In contrast, peak to peak (Pk to Pk) increased with increasing voltages until an asymptote was observed at the highest operating voltages. Pulse shape dependence on operating voltage for a GM counter was discussed in detail, but simultaneous measurement of deadtime and pulse shape was missing for that earlier work. Therefore, no relationship between deadtime and pulse shape could be deduced from the earlier work.[19]

The purpose of this work is to examine pulse shape properties and its relationship with observed deadtime more in-depth. An experiment was designed where deadtime and generated pulses were simultaneously measured and recorded. Four different radioactive sources were used: Thallium-204 (^{204}Tl), ^{137}Cs, ^{22}Na, and Manganese-54 (^{54}Mn). Measurements of deadtime and its associated behavior were discussed in our previous research paper.[20] Based on the findings, the phenomenological basis of deadtime manifestation was presented. Three distinct ranges of deadtime phenomenon depending on the operating voltage were identified, and for each range, a phenomenological model was presented. For the GM detector tested in the study, these regions were: (I) region 1 (600-650 V), (II) region 2 (700-750 V), and (III) region 3 (750-1200 V).

The limited literature is available about deadtime dependence on applied voltages but not much discussion is available about the relationship between pulse shape generated

in a GM counter and detector deadtime. Therefore, this study appears to be the first attempt to present information on correlation between GM deadtime and pulse shape which would be very helpful for the radiation measurement community for better understanding the deadtime phenomenon. The results will validate our hypothesis that deadtime phenomena at different operating voltages are phenomenologically different.

2. MATERIALS AND METHODS

2.1. MATERIALS

Figure 2 shows a schematic of the experimental setup used to measure the deadtime of the GM detector and record the output train of pulses due to radiation incidents. The counting system in this experiment consisted of radioactive half-disk sources, GM detector, high-voltage power supply, preamplifier, oscilloscope, amplifier, integral discriminator, dual counter/timer, and a PC.

The radioactive sources used in this experiment are (a) Thallium-204 (^{204}Tl), (b) Cesium-137 (^{137}Cs), and (c) Sodium-22 (^{22}Na). These sources were designed and produced specifically by Spectrum Techniques LLC. upon our request to conduct this study. ^{204}Tl was produced in February 2019, while the other two radioactive sources were produced in May 2019. Each source consists of two sealed half-disk sources, as can be seen in Figure 2. From now and onward, we will refer to the half-disk source as a split source. The initial activity of each split source was 5 μCi, with ±20% uncertainties.[21] Due to the fact that the radioactive sources are not short-lived isotopes (seconds, minutes, hours) no correction to the deadtime due to decay during measurement was needed.[22] To ensure that the uncertainties associated with each split source do not result in significant statistical errors,

we conducted several evaluations of each split source of the three isotopes. The outcomes showed that each split source resulted in a similar number of observed counts. Hence, the uncertainties did not inflict significant statistical errors. We used the same size and geometry to minimize errors from measuring the radioactive sources.

The GM detector (Ludlum, model 44-7) used in this study is a halogen quenched, end window type detector. The end window is made out of a thin mica layer to detect not only gamma radiation but also alpha and beta rays. The recommended operating voltage of this GM detector is 900 V, while the typical deadtime associated with this model is 200 μs, as specified by the manufacturer.[23] The low-noise charge-sensitive preamplifier (Ortec, model 142A) was connected through "E" input with a connector series "C" with a short coaxial cable to the GM detector.[24] To minimize noise and maintain the preamplifier's stability, it was placed as close as possible to the detector. The preamplifier's capacitor feedback is 1 pF while the pulse tail decays to the baseline in 500 μs. In addition, the preamplifier's bias input was connected to the high-voltage (HV) power supply. Also, the preamplifier was taped to the same location for the subsequent experiments.

The HV power supply (Canberra, model 3125)[25] is housed in the nuclear instrumentation module (NIM), and it is directly connected to the AC line. The oscilloscope (Tektronix, model TBS2000) was connected to the preamplifier through a "T" connector to capture and record the generated pulses directly from the preamplifier.[26] The purpose is to capture and record the pulse shape properties generated from the GM detector without going through the other pulse processing electronics (amplifier, integral discriminator, dual counter/timer). The oscilloscope's output was connected to a PC where an O-scope utility software (provided by Tektronix.inc, version 1.5) was used to record measurements of the

pulse shape properties automatically. The amplifier (Ortec, model 570) was connected to the preamplifier through a "T" connector using a coaxial cable.[27] The amplifier serves two purposes in general: (1) to amplify the pulse coming from the preamplifier, and (2) to shape the pulse and eliminate the long exponential tail of the pulse processed by the preamplifier so that pile up of pulses are reduced. Besides, the amplifier was connected to the integral discriminator (Canberra, model 832).[28] The discriminator was used to produce logic pulses when the linear input pulse's amplitude processed by the amplifier exceeds a threshold. The discriminator was connected directly to the dual counter/timer (Ortec, model 994).[29] The dual counter/timer was used to measure the number of registered counts. The timer was set to 30 minutes for each experiment, and it was used to start and end registering counts from radiation incidents automatically.
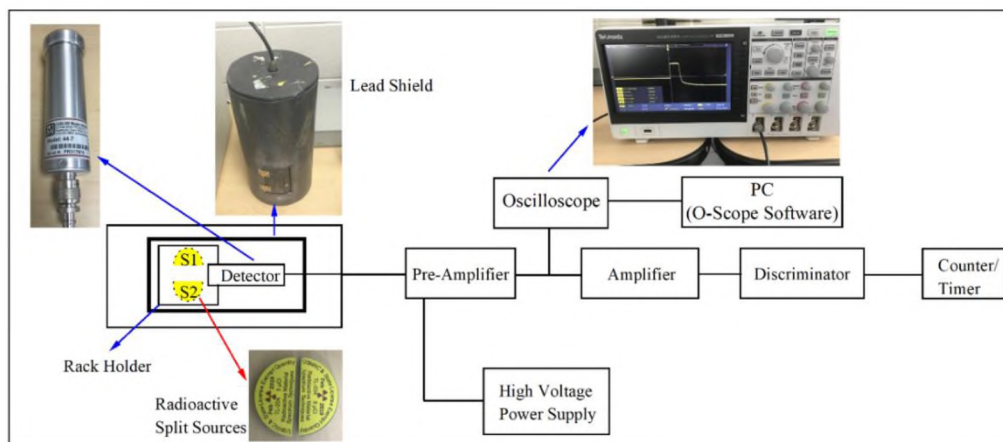
Figure 2. A schematic of the experimental setup for the radiation counting system.

2.2. TWO SOURCE METHOD

In this current study, we utilized the two-source method to measure deadtime dependence on operating voltages. The principle behind this method is that when two

radioactive sources are combined, they will result in fewer observed count rates than if each radioactive source measured individually and summed up. The loss of counts from observing the combined radioactive sources is attributed to deadtime. In our study, we used two split sources for each radioactive isotope. Split source one is referred to as S_1, while split source two is S_2. Combined, they are abbreviated as S_{12}. Since the GM detector is commonly known to behave as non-paralyzable, and it suffers from $\leq 5\%$ of the paralysis factor, applying the non-paralyzable model for calculating deadtime-voltage dependence in our study is, therefore, justified.[6, 8, 14] The derivation of the two-source method is well documented in Knoll's textbook.[4] Since this study focuses on pulse shape analysis, a detailed description of instrumentation optimizations and deadtime measurements are outlined in an earlier paper.[20]

In addition to the three radioactive isotopes ([204]Tl, ^{137}Cs, [22]Na) used in this study, we also examined [54]Mn split sources. However, due to short half-life [54]Mn, the sources seem to have decayed away at a level of unacceptable statistical uncertainty. At high voltages, deadtime measurements for [54]Mn showed negative values. Further, when fractional deadtime ($s_{12}\,\tau$) criterion of between 20% and 40% was used to determine the reliability of deadtime measurements,[19] [54]Mn did not meet the acceptability criterion (exceeding 40%). On the other hand, we found that fractional deadtimes obtained from investigating [204]Tl, ^{137}Cs, and [22]Na sources were within the acceptable range. Hence, the generated pulse shape properties that were acquired from using [54]Mn sources were excluded from this study and should not be used to draw any conclusions.[20]

2.3. OSCILLOSCOPE

The oscilloscope (Tektronix, model TBS2000)[26] was used in this experiment to display and record the train of pulses generated by the GM detector. The oscilloscope's channel one input was connected to the preamplifier through a "T" connector with a coaxial cable. In contrast, the output was connected directly to the PC to process the data in real-time. Table 2 shows the definition for each pulse property collected and analyzed in this study. The bandwidth of the oscilloscope was in full mode. The oscilloscope's probe type was voltage, while the probe's attenuation factor was 10X. The record length for the acquiring option was 20M points, while the sample rate was 500 MS/s. The Horizontal Scale (time per major horizontal division) was set to 200 μs/div while the Vertical Scale was 50 V/div. To automatically record waveform data, we used the triggering mechanism in which the rising edge trigger condition was selected. The trigger delay mode time was set to negative values in order to capture more waveform data. The trigger source was set to channel 1 with a 20V slope. The input signal coupling method for the oscilloscope was (DC), which means it passes both the AC and DC signal components. Besides, it passes the trigger signal without filtering it to the trigger circuit.

Furthermore, the data collection duration for each radioactive split source (S₁ and S₂) was 30 minutes, and 30 minutes for combined sources (S₁₂). Data logging by the O-scope software was set to 15 seconds, which means a total of 120 data points for each pulse property were recorded. It is worth noting that since radiation incidents are random, then random signals must be treated statistically. Hence, each pulse property's averages at the specified operating voltage for each experiment were calculated and analyzed. Figure 3a shows a train of pulses captured while using ^{204}Tl at low operating voltages. It is observed

that the fall time at 600 V is long. However, at higher operating voltages, as shown in

Figure 3b, it is seen that fall time is very short. This behavior is also observed while using

^{137}Cs and ^{22}Na sources. In the subsequent section, we discuss this behavior and its

association with deadtime.

Table 2. Pulse shape measurements with their definitions. These definitions derived from Tektronix's manual for the TBS2000 oscilloscope.

Pulse Property	Definition
Amplitude	It is a measurement over the entire waveform in which it is the average high value of the pulse less the average low value. Its unit is volts.
Area	The area over the entire waveform and measured in volts-seconds. It is positive for measurements above ground and negative below the ground.
Cycle Mean	The arithmetic mean over the first cycle.
Fall Time	Time measurement in seconds that is measured from the high reference value (90%) to the low reference value (10%) of the final value of the pulse. This is known as the tail of the pulse with an exponential decay.
Frequency	The first cycle in a waveform and measured in hertz (Hz).
Positive Pulse Width	The distance (time) between the mid reference (50%) of the pulse.
Positive Duty	This is a calculated measurement and not measured directly. It is the ratio of the positive pulse width to the signal period in percent.
Rise Time	Time measurement where it starts from the low reference value (10%) of the leading edge of the pulse to the high reference value (90%) of the final value.
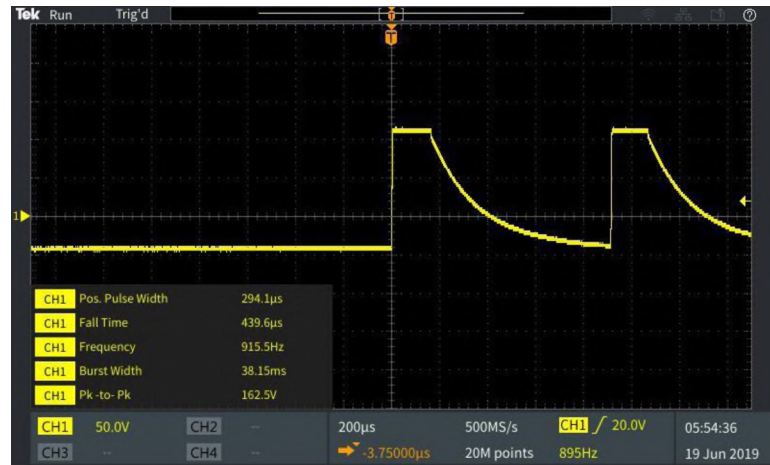
(a)
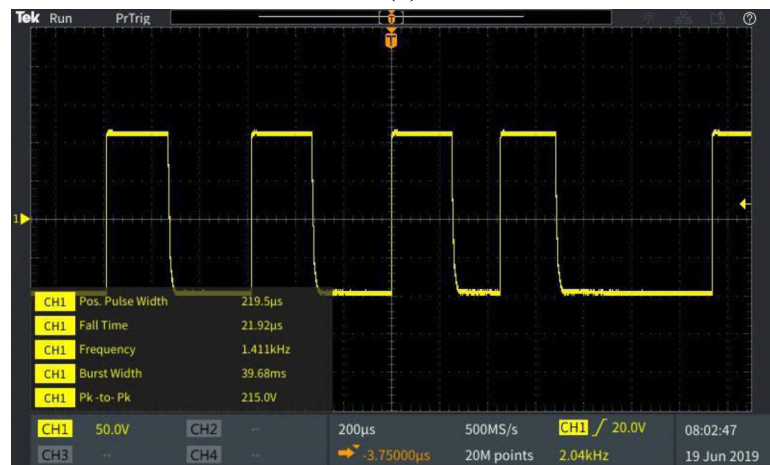
(b)

Figure 3. Train of pulses captured by the oscilloscope using combined sources for: (a) [204]Tl at 600 V; (b) [204]Tl at 1200 V.

3. RESULTS AND DISCUSSION

3.1. PULSE SHAPE ANALYSIS

In an earlier study,[20] a two-source method was used to calculate GM counter deadtime for a wide range of operating voltages. Results showed an interesting relationship between the operating voltage and the detector deadtime for a low operating voltage range.

As the operating voltage was increased further after reaching a minimum value, deadtime started to increase rapidly to reach a maximum. After the maximum value, when the operating voltage was increased further, an exponential decrease in the deadtime was observed, leading to an asymptotic. This behavior of deadtime variation with operating voltage dependence was consistent for three different radiation sources.

Based on these results, three distinct regions of the GM counter deadtime phenomenon were observed. At low operating voltage, the applied voltage is not sufficient to rapidly collect all charges initially produced by the ionization of the gas. Therefore, significant recombination of electrons and positive ions takes place before charge collection. At these low voltages, recorded pulses are weak; hence, not all radiation events are recorded. As the operating voltage is increased in this region, the collection efficiency increases, and collection time reduced. This ultimately leads to a decrease in deadtime while increasing the voltage.

After reaching a minimum deadtime at the highest operating voltage in this region, the operating voltage reaches a point where the velocity of the ions and the election is high enough for charge multiplication. Now a larger number of charge carriers are available, leading to stronger pulses. Since more charge has to be collected, a rapid increase in deadtime is observed in this intermediate operating voltage range. Because increasing voltage in this range increases charge multiplication, deadtime continues to increase with increasing the voltage until the loss of multiplication proportionality. In this intermediate region, the increasing operating voltage is expected to reduce deadtime while increasing the pulse strength until no further increase in deadtime is possible due to the loss of proportionality.

In the high operating voltage range, deadtime starts to exponentially decrease after reaching a maximum value. This exponential decrease in deadtime with increasing operating voltages is because no additional charge multiplication is possible. Hence, the collection time is reduced. The recommended operating voltage GM counter is at the low asymptotic value of deadtime in this region.

Previous studies attempted to obtain a relationship between applied high voltage and deadtime,[7, 19] but the relationship between pulse shape properties and deadtime for GM detector has not been investigated. Therefore, a comprehensive experimental campaign was designed and executed to collect data on deadtime and the various parameters describing the pulse shape. For this study, we only focused on the high voltage/GM region as that is of primary interest to many applications. For this study, ^{204}Tl, ^{137}Cs, ^{22}Na sources were used to examine the relationship between applied high voltage, GM counter deadtime, and pulse shape properties.

Figure 4a shows positive pulse width with respect to applied high voltage. At 600 V, it is seen that the pulse width is at its shortest. As discussed above, in this region, recombination is significant; hence, the charge collection is incomplete, and not many pulses are detected. At 700 V, the ionization process takes place; thus, the generated pulse is larger. From 700 to 750 V, the gas multiplication process took over and resulted in the widest pulse width. As the voltage is increased further, gas multiplications resulted in producing Townsend avalanches; hence, the pulse starts to shrink in width. Furthermore, it can be seen from Eq. (3.1) that the duty cycle depends on the pulse width and the period; henceforth, there is a direct relationship between the period of the pulse and pulse width.

Figure 4(a, h) show that the pulse width decreases while the duty cycle is almost constant after 700 V.

$$Duty\ Cycle = \frac{Pulse\ with}{Period} \qquad (3.1)$$

Furthermore, the pulse at the output of the charge-sensitive preamplifier (such as the preamplifier used in this experiment) is equal to the detector's charge collection time in the ideal case. From Figure 4b, it can be seen that the rise time at low voltages is relatively high. This is because, at these low voltages, recombination processes were prominent, and not many radiation events detected. From 700V and onward, the voltage increase combined with the ionization process resulted in faster collection time. Therefore, it is observed in this region that rise time is exponentially decreasing with increasing operating voltage.

Next, it can be seen from Figure 4c that fall time is at its highest at low voltages. This means that the pulse had a longer tail because the applied voltage is not strong enough. Therefore, the charge collection time is longer, which agrees with the rise time observation. At low voltages, not many radiation incidents are detected, so the overshoot (negative or positive) is too small; hence, the tail is longer. As voltage is increased further, it is observed that fall time is exponentially decreasing because more radiation events are being detected.

Moreover, it can be seen from Figure 4d that amplitude is at its lowest at 600 V. The reason behind this is that recombination processes did not produce a full charge (weak current). Nonetheless, stronger pulses are produced as voltages increased further due to the detection of more radiation incidents. The Townsend avalanches are continuously produced until a sheath of positive ions are formed around the anode, which results in decreasing the electric field below the point where additional gas multiplication cannot

occur. The process finishes when the GM counter produces the same total number of positive ions being created by the incident radiation. At this point, the GM counter will generate the same amplitude for each output pulse. This outcome can be precisely observed after 700 V, as shown in Figure 4d.

Figure 4e shows the frequency of the pulses as a function of applied voltages. The shape of frequency behavior is similar to the shape of the observed radiation counts with increasing voltages. For the region of interest, 750 V and above, it is seen that as the frequency is increased, more counts are detected. The higher the voltage, the faster a pulse is detected, while the shorter distance between pulses is observed.

Furthermore, the definition of cycle mean is the arithmetic mean over the first cycle in the waveform or the first cycle in the gated region. The cycle mean is a part of the amplitude measurement category, as explained in the oscilloscope manual. Figure 4f shows the cycle mean as a function of operating voltages. The cycle mean behavior is similar to the deadtime behavior of the GM detector, where the deadtime tends to exponentially decrease after 750 V. The area of a pulse can be calculated as amplitude times pulse width. It is observed from Figure 4g the area is decreasing exponentially after 750 V. This is expected because the amplitude is constant while the pulse width is exponentially decreasing after 750 V. Looking at the figures of "Area" and "Cycle mean" with respect to applied high voltage, it is observed that they follow a similar behavior of deadtime.

Positive duty is defined in signals as pulse width divided by the period times 100%. It is a calculated value not directly measured. For instance, it is seen from Figure 4h that at 600 V, the positive duty cycle is approximately 30%, which means that the pulse width occupies 30% of the period or the signal is 'on' 30%. Hence, the pulse width is short at this

voltage, as observed in Figure 4a. At 650 V, positive duty is 50%, which means the pulse width occupies half of the period. From 750 V and onward, positive duty for combined radioactive sources is above 55%, which means the signal is 'on' 55% of the time, and it is exponentially decreasing with increasing voltages.

Figure 4i shows the full size of the positive pulse (rise time + pulse width + fall time). When all of these properties are added together, it is observed that from 600 V to 1200 V, the full positive pulse is exponentially decreasing. This behavior is also in agreement with the findings of our previous study.[19] Table 3 summarizes the statistics of the fit lines in Figure 4. Since this study focuses on higher applied voltages and the GM region, the exponential fittings were performed from 750-1200 V.
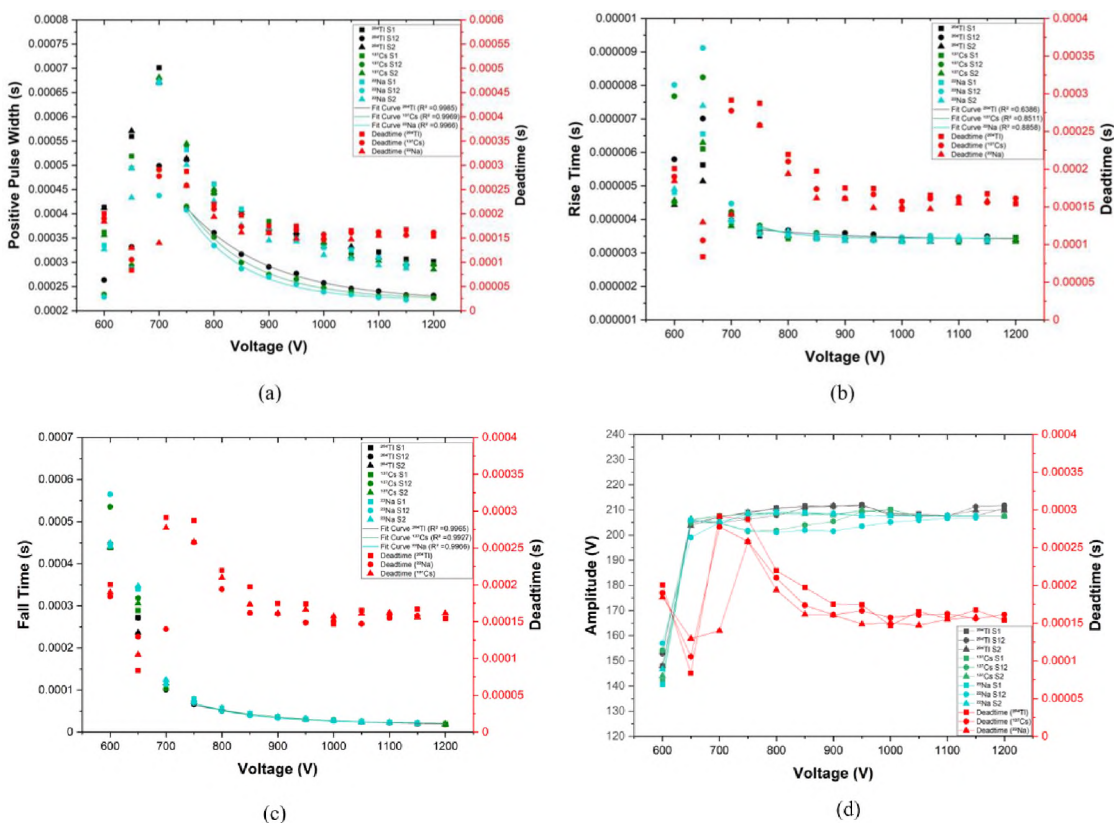
Figure 4. Different parameters with respect to applied high voltage for pulse shape analysis.

(e)

(f)

(g)

(h)

(i)
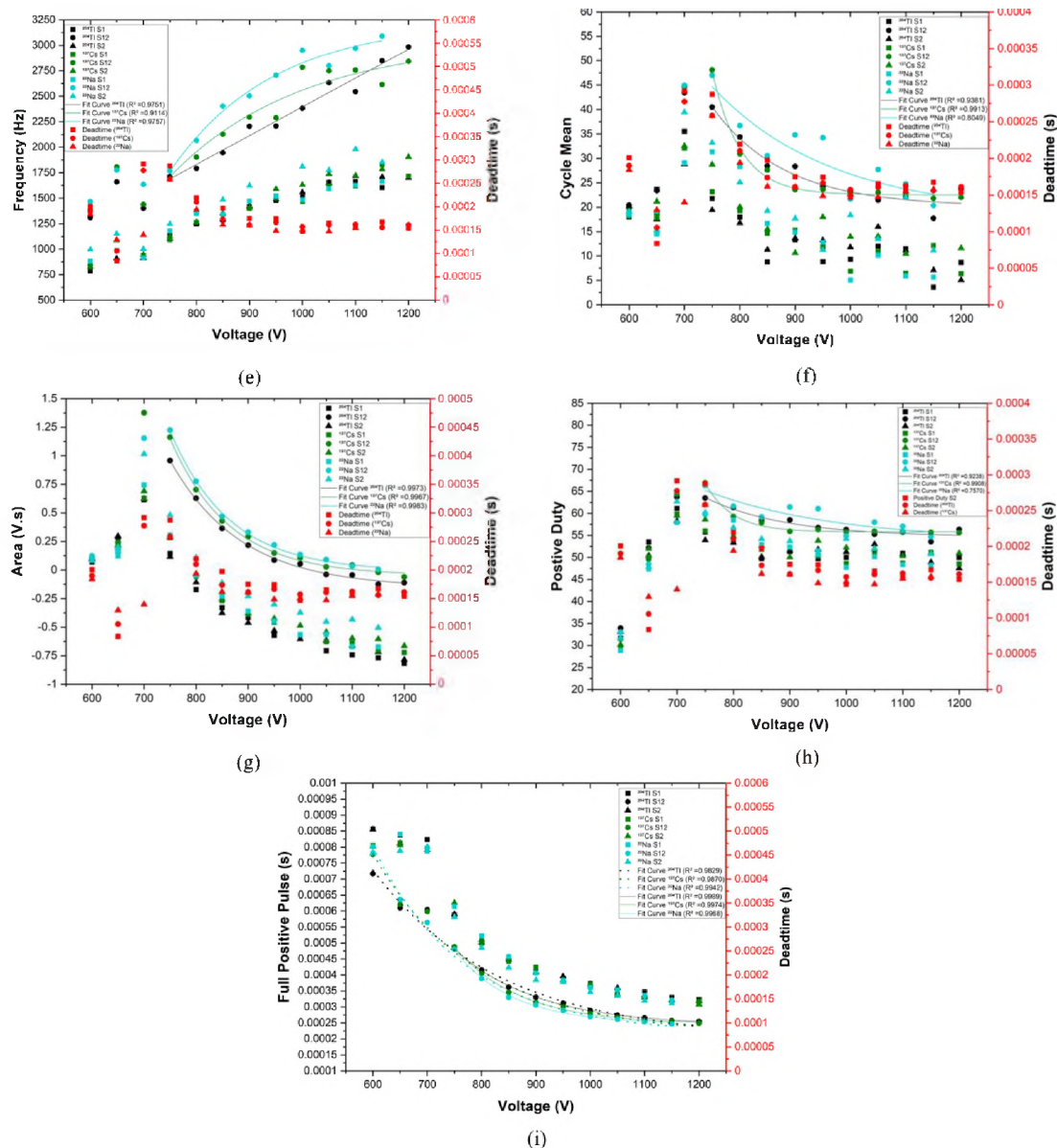
Figure 4. Different parameters with respect to applied high voltage for pulse shape analysis (cont.).

Figure 5 shows the result of some detailed statistical analysis of the results. Since the GM region is of primary interest to many applications, we focused on high applied voltages (from 750-1200 V). Also, since results from individual radioactive sources show

similar behavior when combined sources are used, we focused our correlations analysis on combined sources.

Table 3. Statistical parameters for best fit lines in Figure 4. OriginPro software (version 2020b) was used to derive best fit lines.

EXPONENTIAL FITTING MODELS

Pulse Property	Positive Pulse Width		
Equation	$y = y_0 + A * e^{(R_0 * x)}$		
Source	^{204}Tl S$_{12}$	^{137}Cs S$_{12}$	^{60}Co S$_{12}$
Y0	2.20E-4 ± 2.79E-6	2.23E-4 ± 2.98E-6	2.21E-4 ± 3.2E-6
A	0.0270 ± 0.00577	0.110 ± 0.0395	0.239 ± 0.109
R0	-0.0066 ± 2.91E-4	-0.0084 ± 4.78E-4	-0.0095 ± 6.1E-4
R-Square	0.99851	0.99687	0.99657
Pulse Property	**Rise Time**		
Equation	$y = y_0 + A * e^{(R_0 * x)}$		
Source	^{204}Tl S$_{12}$	^{137}Cs S$_{12}$	^{60}Co S$_{12}$
Y0	3.39E-6 ± 9.83E-8	3.43E-6 ± 2.51E-8	3.43E-6 ± 2.3E-8
A	2.33E-5 ± 9.14E-5	0.094 ± 0.44	0.033 ± 0.14
R0	-0.0058 ± 0.0054	-0.016 ± 0.0062	-0.015 ± 0.0054
R-Square	0.6386	0.8511	0.8858
Pulse Property	**Fall Time**		
Equation	$y = y_0 + A * e^{(R_0 * x)}$		
Source	^{204}Tl S$_{12}$	^{137}Cs S$_{12}$	^{60}Co S$_{12}$
Y0	1.68E-5 ± 1.16E-6	1.91E-5 ± 1.39E-6	2.15E-5 ± 8.6E-7
A	0.00498 ± 0.00158	0.0117 ± 0.00586	0.0455 ± 0.0200
R0	-0.0062 ± 4.37E-4	-0.0073 ± 6.76E-4	-0.0091 ± 5.9E-4
R-Square	0.99649	0.99273	0.99664
Pulse Property	**Frequency**		
Equation	$y = y_0 + A * e^{(R_0 * x)}$		
Source	^{204}Tl S$_{12}$	^{137}Cs S$_{12}$	^{60}Co S$_{12}$
Y0	105526.0 ± 3603694.8	3043.73 ± 310.95	3232.99 ± 157.1
A	-105991.0 ± 3602417.9	-27797.8 ± 38118.4	-69897.5 ± 6264
R0	-2.73E-5 ± 9.55E-4	-0.0040 ± 0.0020	-0.0051 ± 0.0012
R-Square	0.97506	0.91143	0.9757
Pulse Property	**Cycle Mean**		
Equation	$y = y_0 + A * e^{(R_0 * x)}$		
Source	^{204}Tl S$_{12}$	^{137}Cs S$_{12}$	^{60}Co S$_{12}$
Y0	20.13 ± 1.63	22.51 ± 0.36	18.51 ± 10.20
A	6460.2 ± 9949.4	5.96E7 ± 7.55E7	835.30 ± 2228.2
R0	-0.0076 ± 0.0021	-0.01956 ± 0.00168	-0.0046 ± 0.0039
R-Square	0.9381	0.99131	0.80486
Pulse Property	**Area**		
Equation	$y = y_0 + A * e^{(R_0 * x)}$		
Source	^{204}Tl S$_{12}$	^{137}Cs S$_{12}$	^{60}Co S$_{12}$
Y0	-0.154 ± 0.019	-0.047 ± 0.018	-0.012 ± 0.017

Table 3. Statistical parameters for best fit lines in Figure 4. OriginPro software (version 2020b) was used to derive best fit lines (cont.).

EXPONENTIAL FITTING MODELS

Pulse Property	Area		
A	274.04 ± 83.42	927.10 ± 351.57	885.89 ± 273.52
R0	$-0.0073 \pm 4.12E\text{-}4$	$-0.0088 \pm 5.07E\text{-}4$	$-0.0087 \pm 4.1E\text{-}4$
R-Square	0.9973	0.99666	0.99825
Pulse Property	**Positive Duty**		
Equation	$y = y_0 + A * e^{(R_0 * x)}$		
Source	^{204}Tl S_{12}	^{137}Cs S_{12}	^{60}Co S_{12}
Y0	54.66 ± 0.88	55.78 ± 0.15	53.72 ± 5.65
A	1771.764 ± 2910.64	$6.37E7 \pm 8.92E7$	294.57 ± 878.59
R0	-0.0070 ± 0.0022	-0.021 ± 0.0019	-0.0043 ± 0.0044
R-Square	0.92379	0.99083	0.75704
Pulse Property	**Full Positive Pulse**		
Equation	$y = y_0 + A * e^{(R_0 * x)}$		
Source	^{204}Tl S_{12}	^{137}Cs S_{12}	^{22}Na S_{12}
Y0	$2.41E\text{-}4 \pm 3.09E\text{-}6$	$2.461E\text{-}4 \pm 3.54E\text{-}6$	$2.47E\text{-}4 \pm 4.0E\text{-}6$
A	0.03197 ± 0.00592	0.1185 ± 0.03808	0.28506 ± 0.125
R0	$-0.007 \pm 2.54E\text{-}4$	$-0.008 \pm 4.32E\text{-}4$	$-0.001 \pm 5.89E\text{-}4$
R-Square	0.9989	0.9974	0.9968
Pulse Property	**Full Positive Pulse**		
Voltage Range	600-1200 V		
Equation	$y = y_0 + A * e^{(R_0 * x)}$		
Source	^{204}Tl S_{12}	^{137}Cs S_{12}	^{22}Na S_{12}
Y0	$2.017E\text{-}4 \pm 2.61E\text{-}5$	$2.14E\text{-}4 \pm 1.88E\text{-}5$	$2.16E\text{-}4 \pm 1.3E\text{-}5$
A	0.0071 ± 0.0024	0.0129 ± 0.0042	0.0201 ± 0.0051
R0	$-0.004 \pm 5.97E\text{-}4$	$-0.005 \pm 5.57E\text{-}4$	$-0.006 \pm 4.31E\text{-}4$
R-Square	0.9829	0.9870	0.9942

Furthermore, various pulse shape characteristics were examined for their dependence on the operating voltage and its relation to deadtime. Figure 5a shows a negative correlation between the operating voltage and the "Positive Pulse Width." For all three radioactive sources (^{204}Tl, ^{137}Cs, ^{22}Na), the value of the coefficient ranges from -0.94 to -0.90, which is a very strong correlation. However, for all three sources, a weaker correlation between -0.80 to -0.71 was observed with deadtime. Based on the data, one can deduce that there is a strong positive correlation between pulse width and deadtime with coefficients ranging between 0.96 to 0.95, as shown in Figure 5a. This means that longer

the pulse width, the higher the probability for overlapping pulses; hence, deadtime is at its maximum point (at 750 V) when pulse width is observed to be at its maximum width, as can be seen in Figure 4a. As the applied voltage increases, the shorter the pulse width, the more counts are measured. Since, above 750 V the detector starts to operate in the GM region, hence, deadtime starts to decrease exponentially after 750 V until a plateau reached, as shown in Figure 4a.

When observing Figure 5b, one is bound to notice a strong negative correlation between the operating voltage and the pulse "Rise Time" with coefficients ranging between -0.78 to -0.72 for combined sources. Again, there is a positive correlation between deadtime and the pulse "Rise Time." This means that the smaller the "Rise Time", the faster is the collection time of charge due to the increased applied voltage; hence, deadtime shows an exponential decrease until a plateau reach, as shown in Figure 4b.

Similar results were recorded (Figure 5c) for the correlation between the operating voltage and the pulse "Fall Time," with the only difference that the correlation was stronger with the operating voltage (-0.95 to -0.91). Also, pulse "Fall Time," show a strong correlation with deadtime (0.95 to 0.94) Almost identical results were observed for the operating voltage correlation with "Cycle Mean," "Full Positive Pulse," and "Area" (Figure 5d-f).

Nevertheless, the results for the pulse "Frequency" correlation with operating voltage is quite interesting, as shown in Figure 5g. A strong positive correlation is observed (between +0.98 to +0.91) for all sources. This means that increasing the operating voltage increases the count rate. Furthermore, at high frequency, count rate increases, leading to the higher probability for overlapping pulses; however, because the voltage is higher in

which the GM detector operates in the GM region, the deadtime plateau. Pulse "Frequency" and deadtime show a negative correlation between -0.86 to -0.79, as shown in Figure 5g.
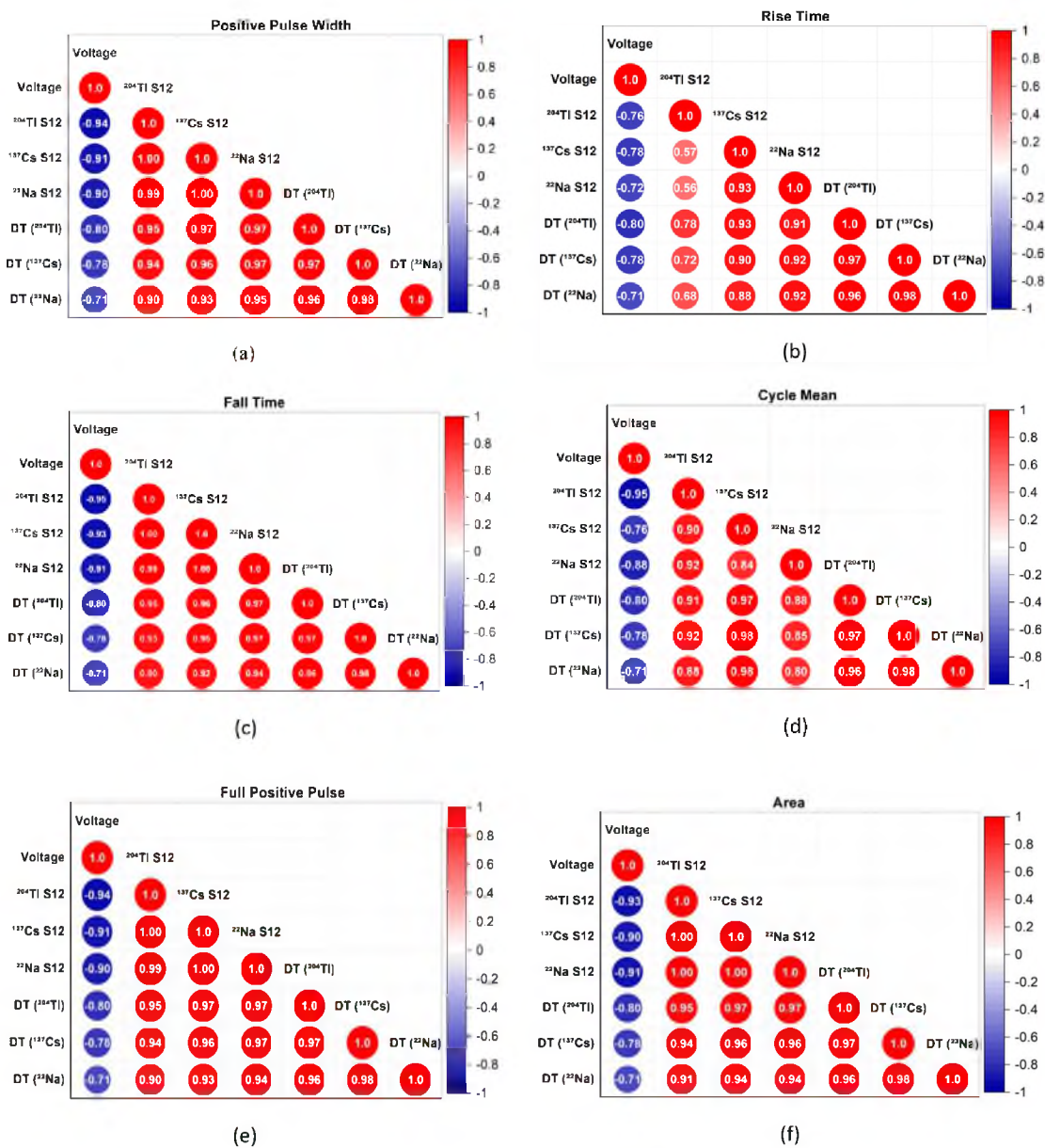
Figure 5. Correlation coefficients for pulse shape characteristics and operating voltages from 750 to 1200 V. S12 stands for combined radioactive sources. DT stands for deadtime.

(g)
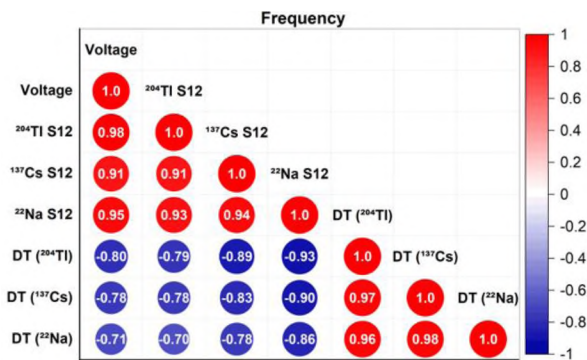
Figure 5. Correlation coefficients for pulse shape characteristics and operating voltages from 750 to 1200 V. S12 stands for combined radioactive sources. DT stands for deadtime (cont.).

4. CONCLUSIONS

To the best of authors' knowledge, this is the first attempt to correlate GM counter operating voltage with pulse shape characteristics and detector deadtime. Based on the data collected in this study, one can draw the following conclusions:

- The general belief that for any GM counter pulse amplitude, pulse shape and deadtime is constant for the entire operating voltage range is incorrect, as recently shown by Akyurek[7] and Almutairi.[19] At low voltages, deadtime decreases with increasing voltages then increases with increasing the voltages further until a maximum deadtime is reached. Then it exponentially decreases until a plateau is reached.

- Akyurek and co-worker's[7] provided some interesting data but their work lacked the analysis of several other important pulse shape properties such as amplitude, fall time, rise time, area, and positive pulse width.

- Data on deadtime and the various pulse parameters were simultaneously collected using ^{204}Tl, ^{137}Cs, ^{22}Na sources to examine the relationship amongst the applied high voltage, GM counter deadtime, and pulse shape properties.

- Based on the data, three distinct deadtime phenomenon depending on the operating voltage are observed.

- At low voltage, the deadtime is caused by charge recombination. Therefore, increasing the voltage increases pulse width and reduces deadtime.

- It can be seen in Figure 4c that rise and fall time are at their highest at low voltages. This means that the pulse had a longer tail because the applied voltage is not strong enough. Therefore, the charge collection time is longer, leading to the long deadtime. Both pulse width and deadtime reduces with increasing voltage in this region.

- When the voltage is high enough for charge multiplication, the deadtime and pulse positive width start to increase. This is due to the fact that more time is needed to collect larger number of charge carriers.

- At the end of the proportionality region, no additional multiplication is possible due to the reduced spaced field intensity after reaching the maximum deadtime.

- After the point of maximum deadtime, there is an exponential drop in deadtime in the GM region until a plateau is reached.

- Operating voltage and detector deadtime exhibit strong correlation with various pulse properties like positive pulse width, rise and fall time, cycle mean, full positive pulse, and area.

REFERENCES

[1] Geiger, H. On the scattering of the α-particles by matter. *Proceedings of the Royal Society of London Series A, Containing Papers of a Mathematical and Physical Character*, 81: 174-177 (1908).

[2] Geiger, H., Müller, W. Electron counting tube for the measurement of the weakest *radioactivities, The Sciences*. 16, 617–618 (1928).

[3] Skinner, S.M. The efficiency of the tube counter, *Phys. Rev.* 48 ,438-447 (1935).

[4] Knoll, G.F. *Radiation Detection and Measurement*. (John Willey & Sons, Ltd, 2010).

[5] Muller, J.W. Dead-time problems. *Nucl. Instrum. Methods* 112, 47-57 (1973).

[6] Patil, A., Usman, S. Measurement and application of paralysis factor for improved detector dead-time characterization, *Nucl. Technol.* 165, 249-256 (2009).

[7] Akyurek, T., Yousaf, M., Liu, X. & Usman, S. GM counter deadtime dependence on applied voltage, operating, temperature and fatigue. *Prog. Nucl. Energy* 73, 26-35 (2015).

[8] Usman, S. & Patil, A. Radiation detector deadtime and pile up: A review of the status of science, *Nucl. Eng. Tec.* 50, 1006-1016 (2008).

[9] Feller, W. On probability problems in the theory of counters. In: R. Courant Anniversary Volume, Studies and Essays. *Interscience*, New York, 105-115, (1948).

[10] Evans, R. D. The Atomic Nucleus, McGraw-Hill, New York, (1955).

[11] Muller, J.W. *A simple derivation of the Takacs formula*. (Bureau International des Poids et Mesures, 1988).

[12] Muller, J.W. Generalized dead times, *Nucl. Instrum. Methods Phys. Res. Sect. A Accel. Spectrom. Detect. Assoc. Equip.* 301, 543-551 (1991).

[13] Albert, G.E., Nelson, L. Contributions to the statistical theory of counter data, *Ann. Math. Stat.* 24, 9-22 (1953).

[14] Lee, S.H., Gardner, R.P. A new G-M counter dead time model, *Appl. Radiat. Isot.* 53, 731-737 (2000).

[15] M. Yousaf, Akyurek, T., Usman, S. A comparison of traditional and hybrid radiation detector dead-time models and detector behavior, *Prog. Nucl. Energy*, 83, 177-185 (2015).

[16] Tsoulfanidis, N., Landsberger, S. Detector dead-time correction and measurement of dead time. In *Measurement and Detection of Radiation*, 63-66 (CRC Press, 2015).

[17] Akyurek, T., Tucker, L.P., Liu, X., Usman S. Portable spectroscopic fast neutron probe and 3He detector dead-time measurements. *Prog. Nucl. Energy* 92, 15-21, (2016).

[18] Costrell, L. Accurate determination of the deadtime and recovery characteristics of Geiger-Muller counters, *Journal of Research of the National Bureau of Standards*, 42-3, 241-249 (1949).

[19] Almutairi, B, Akyurek, T, Usman, S. Voltage dependent pulse shape analysis of Geiger-Müller counter. *Nucl. Eng. Tec.* 51, 1081-1090 (2019).

[20] Almutairi, B., Alam, S., Akyurek, T, Goodwin, C., Usman, S. Experimental evaluation of the deadtime phenomenon for GM detector: deadtime dependence on operating voltage. Submitted to *Scientific Reports* (2020).

[21] Disk Source Sets. www.spectrumtechniques.com (2020).

[22] Radović, A.S. and Usman, S. Voltage dependent pulse shape analysis of Geiger-Müller counter. *Nuclear Technology*. 157(1), 106-109 (2007).

[23] Model 44-7 Alpha-Beta-Gamma Detector. www.ludlums.com (2020).

[24] 142A/B/C Preamplifiers. www.ortec-online.com (2020).

[25] Model 3125 0-2/0-5 kV Dual H.V. Power. www.nuclearphysicslab.com (2020).

[26] TBS2000 Digital Storage Oscilloscope. www.tek.com (2020).

[27] Model 570 Spectroscopy Amplifier. www.ortec-online.com (2020).

[28] Cardoso, J. M., Simões, J.B., Menezes, T., Correia, C.M.B.A. CdZnTe Spectra improvement through digital pulse amplitude correction using the linear sliding method. *Nucl. Intstr. and Meth.* 505, 334-337 (1999).

[29] Model 994 Dual Counter/Timer. www.ortec-online.com (2020).

IV. MATERIAL CHARACTERIZATION OF NEUTRON–IRRADIATED ACCIDENT TOLERANT SILICON CARBIDE CLADDING FOR HIGH BURNUP SMALL MODULAR REACTOR CORE

Bader Almutairi[a,b,c], Safwan Jaradat[d], Cameron Goodwin[c], Ayodeji Alajo[a], Shoaib Usman[a], Syed Alam[a]

[a]Department of Mining and Nuclear Engineering, Missouri S&T, USA

[b]Environment and Life Sciences Research Center, Kuwait Institute for Scientific Research, Kuwait

[c]Rhode Island Atomic Energy Commission, Narragansett, Rhode Island, USA

[d]Department of Physics, Higher Colleges of Technology, Abu Dhabi, United Arab Emirates

ABSTRACT

Accident tolerant fuel (ATF) cladding is one of the most active area for research to advance the global contribution of nuclear energy since ATF will ensure and enhance the reactor safety allowing long refueling cycles and higher burnup. Silicon Carbide (SiC) is one material that can potentially be a solution to this long-standing challenge. This study offers both computational reactor physics modeling and experimental investigation to examine the behavior of SiC in nuclear reactor environment. With recent interest in Small Modular Reactors (SMR), this study selected SMR compact core as a reference assembly for Computational Burnup Modeling (CBM). Results of CBM suggest that SiC cladding will provide highest burnup and maximum uranium utilization. Therefore, subsequent experimental investigations focused on SiC only. Rhode Island Nuclear Science Center (RINSC)'s was used to investigate effects of irradiation on sintered tubular SiC material

samples at 1atm, initially at 120°C, followed by high temperatures between 850°C and 1350°C to simulate harsh reactor environment.

Experimental analyses of (a) weight loss and (b) burst testing are considered for SiC samples. For the weight loss experiment, we have considered both types of samples: (1) Non-irradiated and (2) Neutron-irradiated samples. Weight loss was found to be dependent on sample geometry. Irradiated samples show ~2–10% higher weight loss per area than that of the non-irradiated samples. Besides, considering the medium flow rate (less than 10 g/min), it has been observed that the irradiated samples exhibit ~10–40% higher weight loss than that of the non-irradiated samples over temperatures of 120°C, 850°C to 1350°C. It is also seen that material loss rates are generally more sensitive at higher temperatures than at lower temperatures, and irradiated samples are more prone to weight loss. Furthermore, for the burst testing experimental investigations, experiments were conducted for (1) As-received samples (2) Non-irradiated samples and (3) Irradiated samples. Considering the three types of samples, it was observed that the maximum and minimum peak load values are ~70% higher and ~60% lower than the average peak load while fracture hoop stress is consistently ~70–75% higher than the internal pressure for all as-received samples. Experimental and computational investigations suggest that SiC is a viable candidate for ATF cladding material.

1. INTRODUCTION

After the 2011 Fukushima Daiichi nuclear disaster, various research and development (R&D) programs have been devoted to finding a potential ATF cladding. Silicon Carbide has been proposed as a potential ATF cladding.[1, 2, 3] Due to SiC's lower

corrosion rate, it might tolerate higher fuel burnups. In addition, SiC has favorable characteristics in which it can enhance reactor safety, increase fuel burnup, and possibly enhance the power level of Light Water Reactors (LWRs). These favorable characteristics make SiC a potential ATF cladding that can outperform the traditional Zirconium (Zr)-based alloy cladding of nuclear fuel. Zirconium alloys have been used as fuel cladding in naval reactors since the 1950s because it has lower neutron absorption cross-section than stainless steel.[4,5,6] In the 1960s, the nuclear industry began adopting zirconium alloys as a cladding material, and since then, it became the cladding of choice for LWRs worldwide. However, zirconium alloys show unfavorable characteristics in the water at high temperatures, such as increased corrosion rate and material degradation. This, in turn, imposes limits on their in-core residence time. Besides, in severe accident scenarios, the self-accelerating of the exothermic steam-zirconium reaction at high temperatures of 1200°C is one of the significant weaknesses of zirconium alloys.[7,8,9] Not only does it generate a large amount of heat, but it also produces hydrogen gas as a product of the reaction.[10] Hydrogen is an extremely flammable gas, and it can ignite and creates an explosion once it has contact with hot surfaces with a minimum temperature of 520-720°C. It is worth noting that Hydrogen initiated several hydrogen-air chemical explosions due to the reaction between steam and nuclear fuel cladding. This ultimately resulted in the failure of three of the reactor containment buildings in the Fukushima nuclear accident. The accident led the industry to seriously consider redesigning fuel and cladding in an effort to tolerate accident conditions.

Simply put, SiC possesses several relatively favorable characteristics over zirconium alloys. These characteristics include the following: (1) higher melting point (2,730°C); (2)

higher strength at elevated temperature (>1,600°C); (3) lower neutron absorption cross-section, (4) higher dimensional stability when exposed to radiation; and (5) less chemical reactions due to fuel and coolant interactions. Because of these characteristics, SiC shows improved corrosion resistance and reduced susceptibility to hydrogen embrittlement.[7, 8, 9, 11, 12, 13] MIT[4, 5] has investigated the use of multi- layered SiC composite for the possible application in LWR fuel cladding. Their study concluded that SiC composite could withstand irradiation with minimal material degradation and endure high temperatures without failure. In addition, since SiC cladding does not creep down towards the fuel, the fuel gap remains open. This, in turn, adds heat transfer resistance and, therefore, the nuclear fuel temperature can be higher such as in the application of advanced high-burnup SMR cores in which the current Zr-based alloys cannot be of practical use.[4, 5, 11, 14, 15, 16, 17, 18]

While zircaloy cladding currently in use can survive the achievable burnup of 60–70 GWd/tonne,[19, 20, 21] attaining 15 years' long-life core would exceed the discharge burnup of 90 GWd/tonne. This leads to limit the cladding design by a significant margin. Therefore, the typical Zr cladding will not be a feasible choice, and improvements in nuclear fuel/cladding design are warranted to facilitate higher burnup.[22, 23]

This paper investigates the behavior of alternative cladding for long-life core (15–20+ years), suitable for applications such as in small modular reactor (SMR) or marine propulsion.[22, 24, 25] Relying on both computational modeling and experimental analyses feasibility of accident-tolerant claddings are investigated. The first part of this study considers the reactor physics modeling of the 2D assembly of soluble-boron-free (SBF) SMR core. The computational modeling investigates several potential accident-tolerant cladding candidates in order to find the best cladding that exhibits the highest achievable

discharge burnup, a dominant factor for determining core lifetime. Based on the results of the first part (neutronic analyses), SiC is chosen as the cladding material for its lower neutron capture and higher burnup potential. The second part of this study experimentally analyzed the behaviors of both irradiated and non-irradiated SiC. Sintered tubular SiC was used as the material of choice for the experimental campaign. Sintered SiC were exposed to oxidizing environments containing pure steam at 1 atm 120°C, and subsequently at higher temperatures (850°C to 1350°C) to simulate the harsh environment in a nuclear reactor. This harsh reactor environment is known to cause weight loss and mechanical strength degradation[4, 5] in SiC. The fact that SiC tubes are not available that matches the geometry of Zr cladding, it was necessary to study the samples of various thicknesses and surface areas to understand the effect of sample geometry on material degradation.

It is worth noting that:

- The main objective of this work is to understand the fundamental behavior of SiC in terms of weight loss and mechanical strength, which provides us with a clear indication of the SiC behavior under the harsh environment.

- The SiC experiments were conducted at the Rhode Island Nuclear Science Center, which permitted irradiation and conduct of the experiments for a maximum of 8 hours/day. This, however, does not prevent us from understanding the material properties.

- Several studies[3, 26, 27] have shown that steam pressure, up to 20.43 atm, has a limited effect on the oxidation behavior on SiC. Hence, we conducted our study at 1 atm partial pressure.

- Uncertainty quantification and statistical analyses are out of the scope of this paper, although authors reported some standard deviation and error for the samples). A detailed error and statistical analyses will be reported in a future work.

- A detailed discussion of the obtained results from the Neutron Activation Analysis (NAA) is out of the scope of this study.

2. CLADDING SELECTION FOR HIGH BURNUP APPLICATION: NEUTRONIC INVESTIGATION

Our previous studies[20, 21, 24, 28] focused on homogeneously mixed UO2 fuel in a 13X13 assembly [29] and confirmed that 15% of initial uranium enrichment is required for achieving a burnup of 100 GWd/tonne, which will be necessary for a core lifetime of 15 effective full power years (EFPY). This means that the 15-EFPY fuel cycle leads to very high (average) discharge burnups (ca. 100 GWd/tonne), which are far beyond the current operating experience in Pressurized Water Reactors (PWRs). In addition, considering the radial and axial power peaking factors, higher local burnup values are expected to elevate the performance demand for Accident Tolerant Fuel (ATF) cladding material.

For various candidate claddings, a 2D assembly-level with specific fissile loading was simulated to study the maximum attainable discharge burnup. For high burnup, our neutronic analyses used 15% and 19.9% enrichment for UO_2 fuel, which is significantly higher than the current industry practice. Due to high interest in light-water SMR reactors, a compact 13X13 assembly was modeled using MCNP 6.1, as shown in Figure 1.[20, 21, 24, 28] Table 1 shows the design parameters for the 2D lattice of the proposed SMR core.[30, 31, 32, 33, 34, 35]

SMR Fuel Assembly
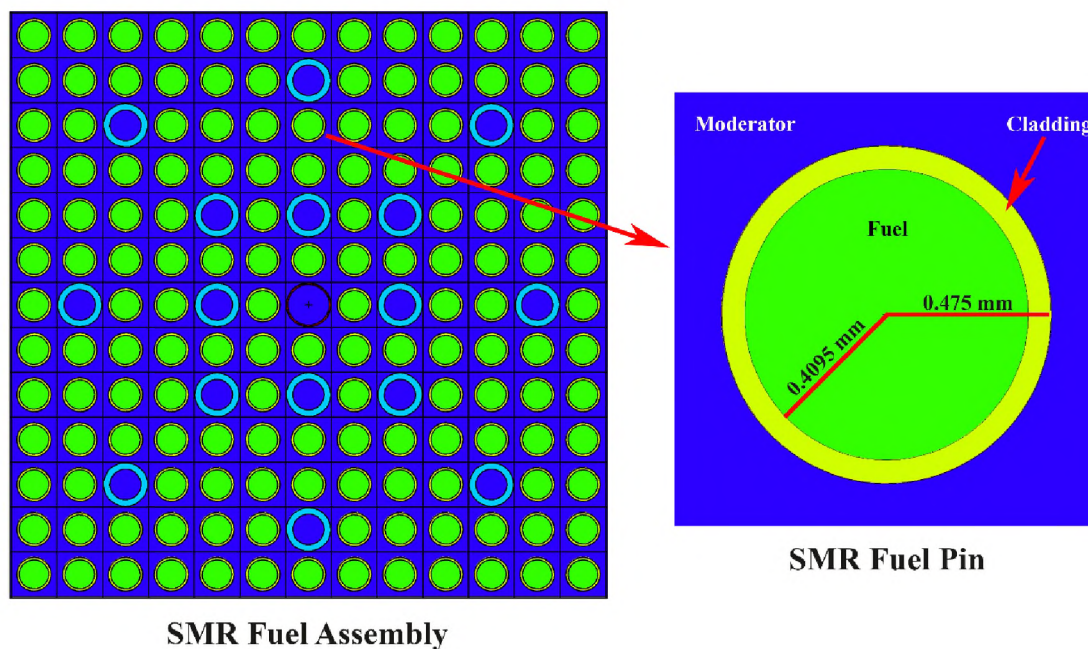
Figure 1. 13X13 geometry layout of the 2D subassembly lattice along with pin cell layout for a PWR-SMR reactor core.

Table 1. Design parameters of proposed SMR core.[20, 21, 24, 28, 29]

Design Parameters	Values
Thermal power (MWth)	333
Assembly array	13X13
Center-to-center pitch (cm)	1.265
Pellet thickness (mm)	8.19
Cladding + gap thickness (mm)	0.66
Total rod diameter (mm)	9.5
Pitch/diameter (P/D) ratio	1.33
Side length of an assembly (m)	0.1645
Area of an Assembly (cm^2)	300
Hydrogen to Heavy Metal (H/HM) ratio	3.99
Soluble boron concentration (ppm)	0

Figure 2a and 2b show k∞ vs. burnup for 15% and 19.9% enrichment, respectively, for various cladding materials. It can be seen that UO2 fuel with SiC cladding achieves the highest discharge burnup (BD). All other ATF candidate cladding materials fall sufficiently short of SiC and Zr claddings. For both the 15% and 19.9% enrichments, SiC outperforms Zr cladding in terms of BD. This superior performance is attributed to the additional neutron moderation in SiC due to the presence of carbon atom along with the lower thermal capture cross-section of silicon in comparison with zirconium. In addition, it has been observed for both fissile enrichments that SiC outperforms APMT, FeCrAl, SS (considering both SS304 and SS310), and Zircaloy (considering both Zr-2 and Zr-4) claddings by ∼7%, ∼6%, ∼10%, and ∼5%, respectively.
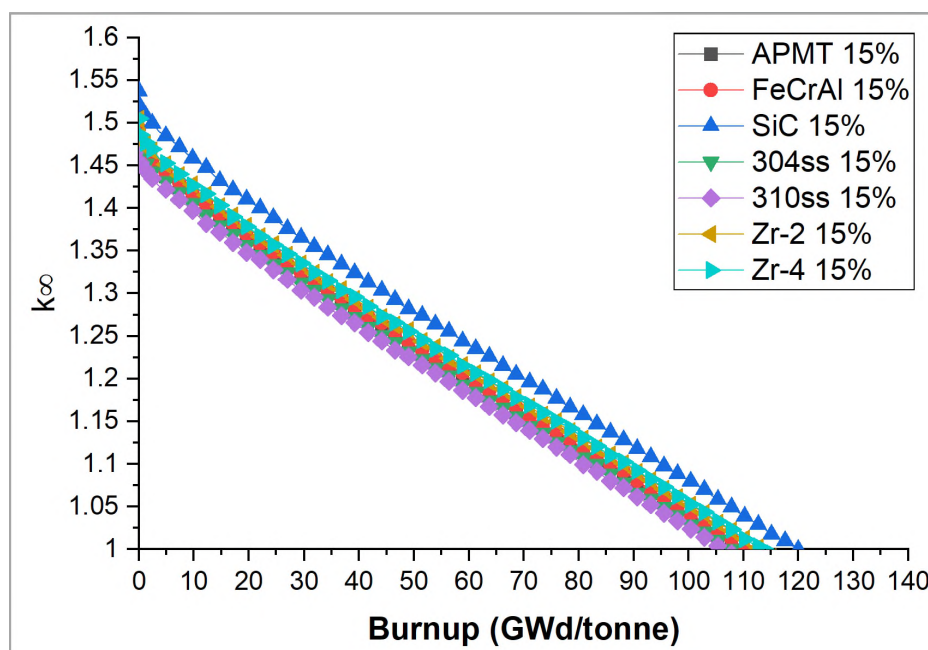
(a)

Figure 2. Reactivity vs. burnup for UO2 fuel: (a) 15% enrichment; (b) 19.9% enrichment.

(b)
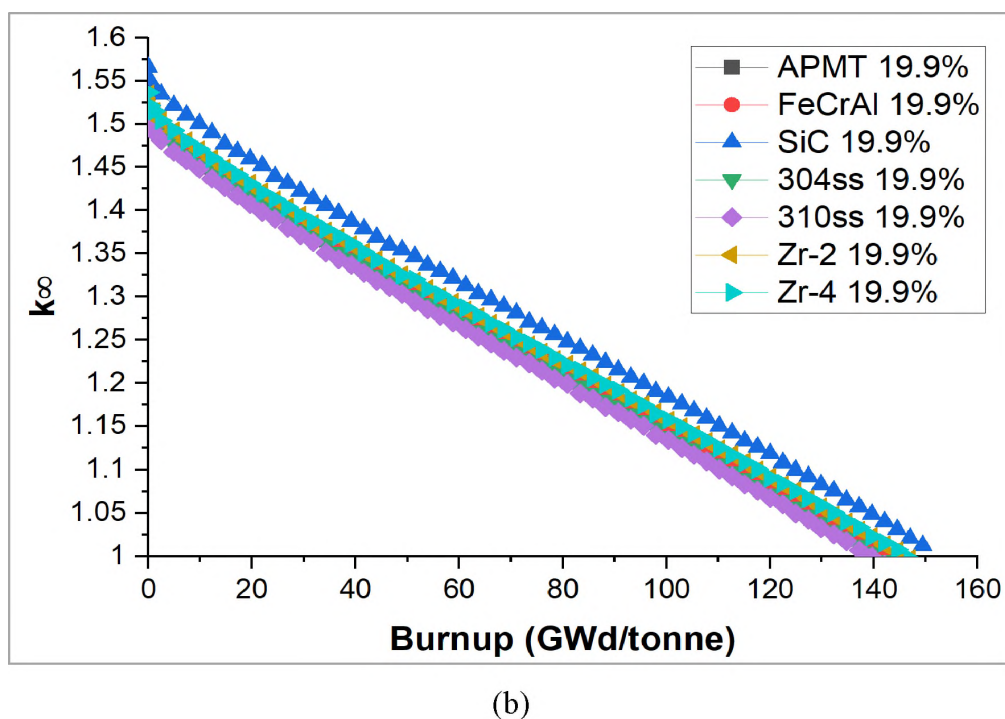
Figure 2. Reactivity vs. burnup for UO2 fuel: (a) 15% enrichment; (b) 19.9% enrichment (cont.).

Reactivity behavior is examined further in Figures 3a and 3b by considering BD penalty and gain. In these figures, the difference in reactivity (in pcm) is presented using SiC as reference cladding. Fundamentally, it has been consistently observed that the highest achievable burnup is obtained following this pattern: SiC > Zr > FeCrAl > APMT > SS. The physical explanations of this pattern were well explained in a previous literature.[25] FeCrAl falls short of SiC and Zr, mainly due to the presence of iron. Furthermore, APMT exhibits lower burnup than FeCrAl. This is attributed to the presence of high resonance absorbing material molybdenum. SS-based claddings exhibit the lowest burnup due to the presence of iron, molybdenum, and nickel.

(a)

(b)
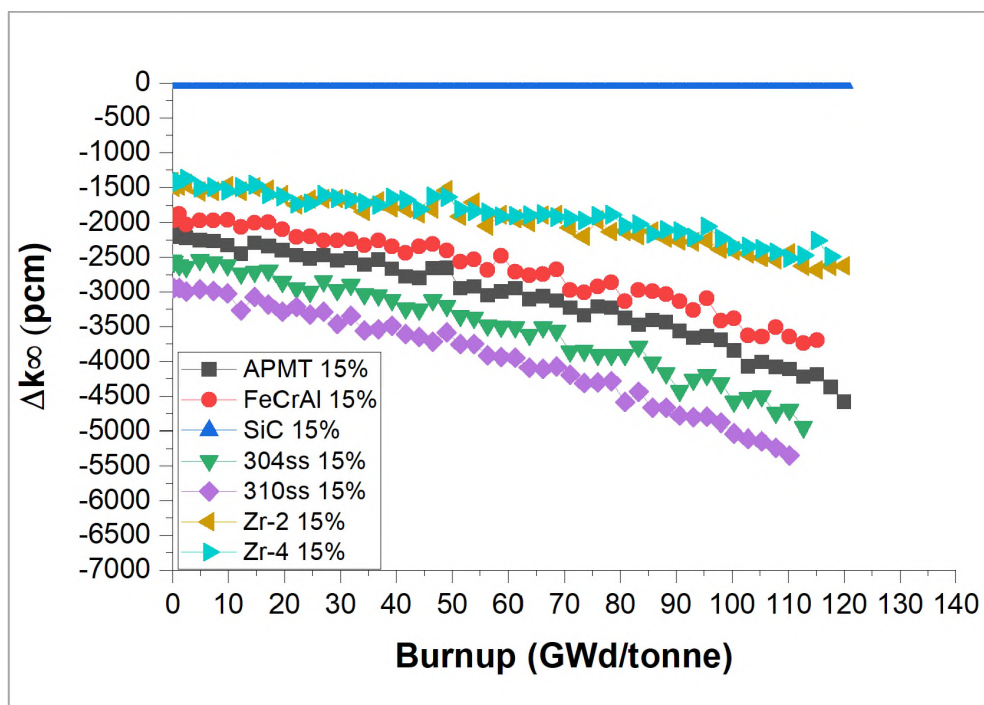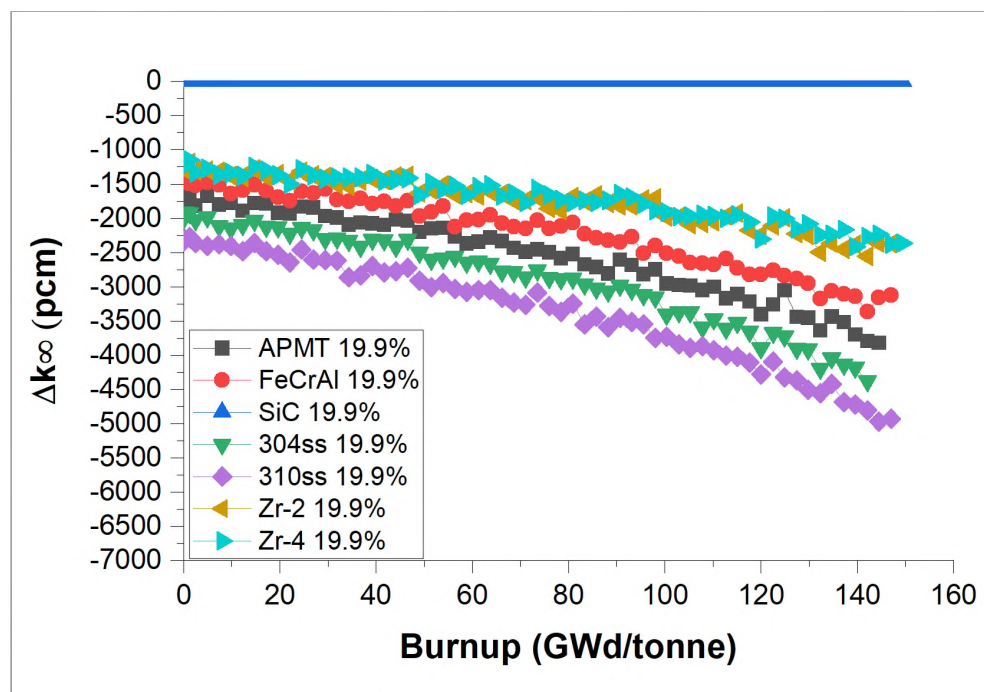
Figure 3. Δk∞ from SiC clad vs. burnup: (a) 15% enrichment; (b) 19.9% enrichment.

In order to confirm the neutron capture and reactivity behavior of the candidate cladding, we calculated the beginning-of-life (BOL) flux spectrum. Derived from the normalized flux spectrum, we have calculated the normalized flux ratio of the candidate claddings with respect to the flux values of SiC in the thermal energy range, where our reference core is a LWR. For the flux calculations, we have not considered Zr-2 and 304SS since these naturally exhibit a similar flux associated with Zr-4 and 310SS. It can be observed from Figure 4a and 4b that SiC exhibits the softer spectrum due to the less absorption neutron capture probability than that of the other claddings. The neutron flux clearly explains reactivity behavior.

One of the primary requirements for a long core lifetime is the utilization of higher fissile enrichment in the reactor core. It can be seen that although traditional Zr cladding can survive until a maximum of 70 GWd/tonne, higher fissile enrichment leads to much higher BD (above 100 GWd/tonne). From Figure 5, it can be observed that 15% fissile enrichment generally leads to 105 GWd/tonne to 117 GWd/tonne for the candidate claddings to achieve at least 15 years of core lifetime (according to our previous studies). Nevertheless, if we do not want to violate the enrichment constraint and also increase the core lifetime even longer (longer than 15 years), we can utilize 19.9% enrichment to obtain the highest achievable core lifetime while not exceeding the enrichment limit of 20%. It is clear from Figure 5 that the utilization of 19.9% enrichment leads to a burnup of around 135–150 GWd/tonne, which is ~30% higher than that for 15% enrichment. The traditional zircaloy cannot survive this higher burnup. Therefore, an accident-tolerant cladding would be required for our proposed application.
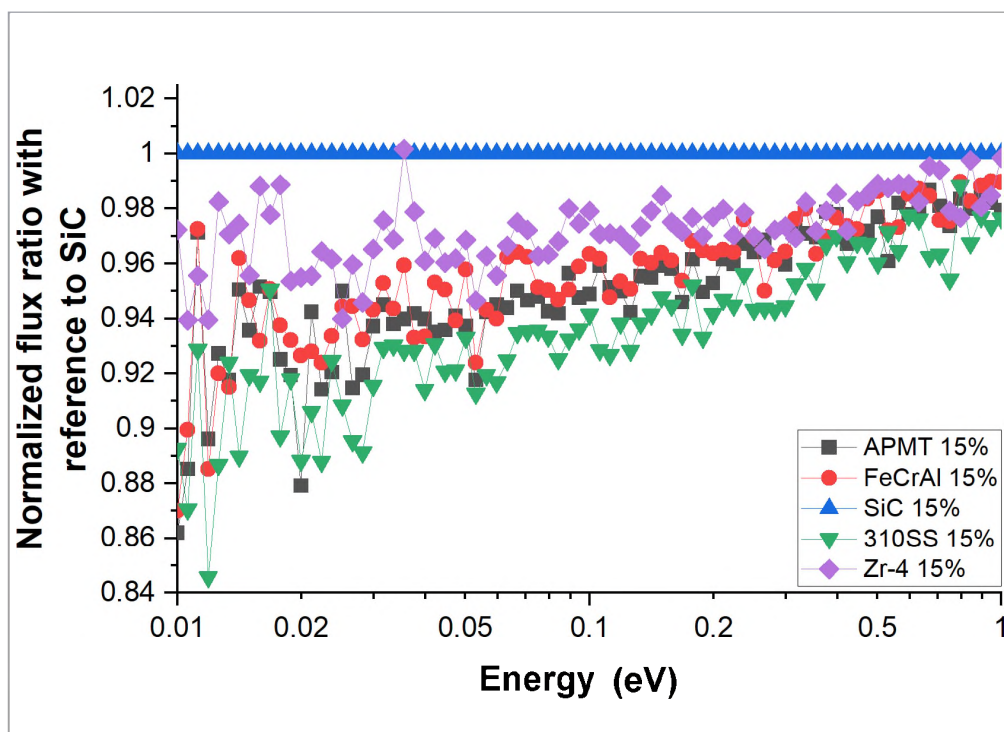
(a)
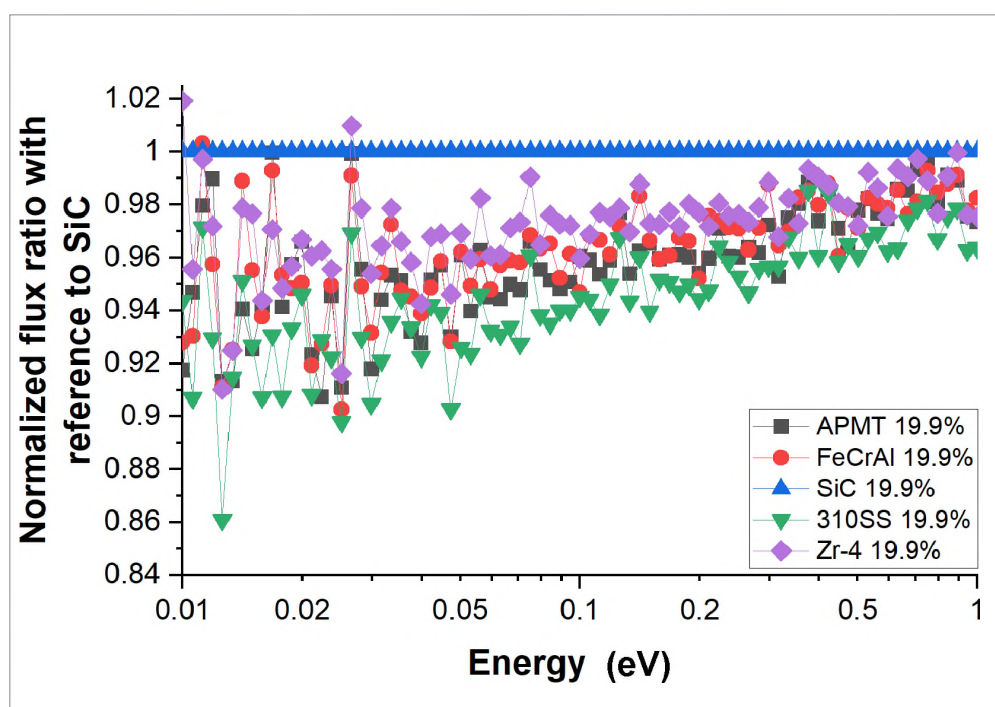
(b)

Figure 4. Beginning-of-life normalized flux ratio with reference to SiC in thermal energy range: (a) 15% enrichment; (b) 19.9% enrichment.
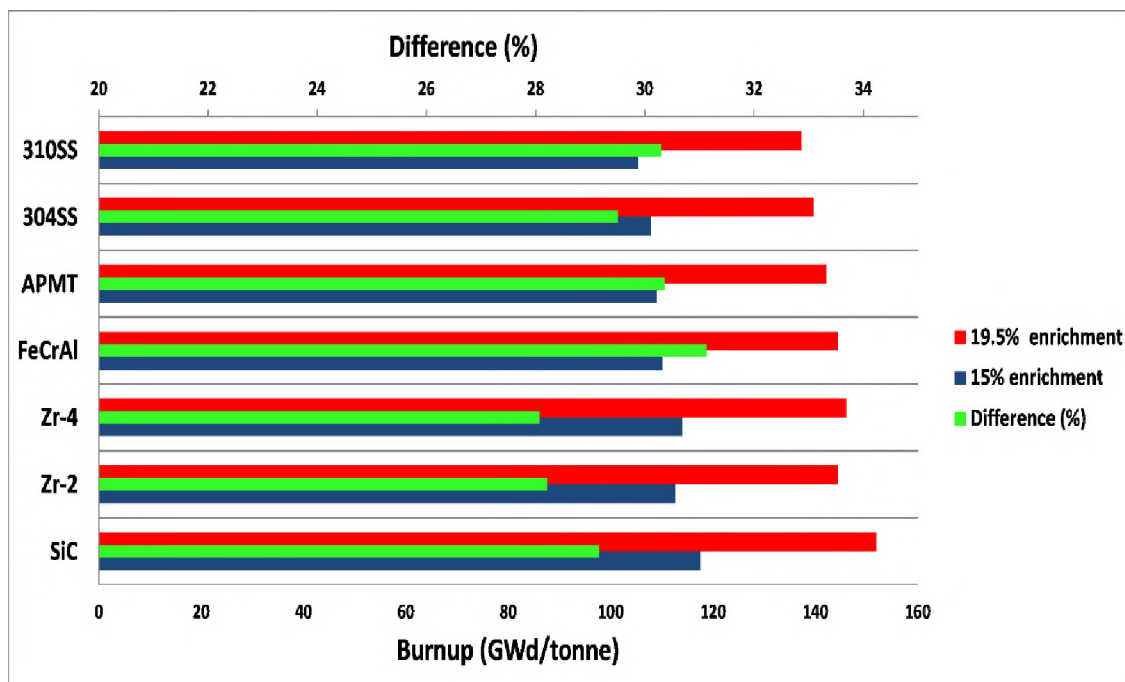
Figure 5. Discharge burnup for different claddings for 15% and 19.9% enrichment along with their difference (%).

Our previous studies[20, 21, 24, 28] showed that around 100 GWd/tonne (on assembly-level), the core life can be extended to 15 years or more. Accordingly, it can be assumed that Zr would not be an appropriate choice for our long lifetime core since it will suffer from a cladding failure at higher burnups and temperatures. Furthermore, it can also be observed from our discussion that unlike SiC, all other claddings prevent us from getting the maximum benefit of higher enrichment utilization due to their higher neutron capture in comparison with SiC. Hence, only SiC cladding stands out as the potential candidate for our SMR application. Going forward, we limited our experimental research to SiC cladding only.

3. CURRENT RESEARCH STATUS OF SILICON CARBIDE

DOE's nuclear program showed an interest in SiC as a potential ATF cladding for the purpose of replacing traditional Zr-based alloys.[1, 36, 37] Therefore, information on SiC's microstructural properties under irradiation is essential. Other crucial properties that warrant further investigations are (1) interaction of SiC materials with coolant; (2) extent of the possible synergy of environmental conditions; and (3) irradiation under high temperatures.[37] Furthermore, Zr-based alloys under high- burnup applications exhibit several unfavorable material characteristics, including fission gas release, ballooning, bursting, and cracking. Henceforth, an alternative ATF cladding that outperforms Zr-based alloys under normal operating conditions and severe accidents is critically needed. The findings of this study suggest that SiC can overcome some of the challenges faced by Zr-based cladding. Several types of SiC are available in the industry as well as academia, such as monolithic, fiber, and ceramic matrix composites.[37, 38] Each of these types has distinct mechanical strength, radiation resistance, thermal, and chemical properties depending on its fabrication technique. In a recent study,[37, 39] Idaho National Laboratory (INL) reviewed key factor issues for the possible deployment of SiC in advanced LWR fuel development. Their study discussed some of the SiC fabrication techniques, benefits, outstanding issues, and provided projections of SiC's current technology development status. Additionally, INL conducted significant developmental efforts to characterize silicon carbide materials as well as investigated their feasibility in nuclear environments. INL consistently demonstrated the advantages of SiC materials as a cladding material instead of Zr-based alloys. Furthermore, INL used a MELCOR code, a severe accident analysis computer code developed at Sandia

National Laboratory in New Mexico for the U.S. Nuclear Regulatory Commission,[37, 40] to simulate the Three Mile Island (TMI-2) accident. The simulations involved a loss of coolant accident (LOCA) scenario where the code assumed the full replacement of Zr-alloy materials with SiC ceramics and used existing data on SiC properties. The results showed an improvement in the reactor coping time with SiC materials compared to Zr-alloys.

The experimental data on SiC might still be insufficient to confidently adjudicate SiC as the new reliable cladding system. Moreover, technology gaps of SiC still exist, particularly for SiC composite materials. Nonetheless, early observation indicates the potential adoption of SiC components in nuclear environments. Additionally, even though the report focuses mainly on the use of SiC in LWRs, a study[41] by ORNL has also suggested that SiC can not only be used in long-life PWR-type reactors but also be potentially used in fluoride salt reactors.

4. EXPERIMENTAL METHOD

Experimental analyses of (a) weight loss[42, 43, 44] and (b) burst testing[45] are considered for SiC samples in this study. The weight loss experiment utilized the nuclear research reactor at Rhode Island Nuclear Science Center (RINSC) in the USA, a 2 Mega-Watt, light water-cooled, pool-type reactor. The burst testing experiment is conducted at the mechanical engineering department facility of the University of Rhode Island.

A total of 150 SiC samples were used in this experimental campaign. SiC specimens were manufactured by the pressureless[46, 47] sintering of submicron silicon carbide powder in a proprietary extruding process.[48] The sintering process results in a self-bonded and

95% dense fine-grained (less than 10 m) SiC product. Monolithic tubular SiC samples were obtained from Saint-Gobain Inc.[48]

The SiC samples are SE grade Hexoloy with a density of 3.05 g/cm^3. The reported dimensions of the SiC samples by Saint-Gobain Inc. are 13 mm Height (H), 14 mm Outer Diameter (OD), 12.44 mm Inner Diameter (ID), and 1.56 mm Thickness (T). However, we observed a slight variation in samples' dimensions due to fabrication tolerance. The SiC specimens' dimensions were measured by using a calibrated micrometer (Mitutoyo, model number 293-340-30CAL) with ±0.00005 inch accuracy. Therefore, in the burst testing section, we reported the measurements of the SiC specimens' dimensions in inches.

Out of the 150 provided SiC specimens, 44 samples were chosen randomly and tested for impurity using Neutron Activation Analysis (NAA) method.[49] A pneumatically timed-controlled tube (known as the rabbit system) was used to bombard the 44 samples (each trial utilized four samples) with neutrons inside the core of the research reactor. After exposure to the neutrons, the samples were deposited in a lead-shielded box in order for the radioactivity to reach acceptable limits for safe handling. A Geiger-Muller counter was used to detect the level of radioactivity of the SiC samples. Then, the gamma-ray spectroscopy detected the radioactivity of each sample using a High-Purity Germanium detector (HPGe); hence, the consecrations of elemental compositions in the SiC specimens were detected. It is found that concentrations of impurities are negligible. Discussing in detail the results from performing the NAA is beyond the scope of this study.

Furthermore, a total of 106 specimens were used for weight loss and burst testing experiments. The samples were divided into 23 groups: 12 groups were labeled as "non-irradiation samples," and 11 groups were labeled as "neutron-irradiation samples." Each

group consisted of 4 SiC samples. Furthermore, a total of 14 SiC specimens were labeled "as-received samples" in which they were used as control samples (not exposed to steam, heat, or neutron irradiation). All the samples were decontaminated by immersing them in a deionized (DI) water for 3 minutes in the ultrasonic cleaner (Model VGT-2000). Samples were further decontaminated using 10% methanol and left to dry. The cleaned, dried SiC specimens were weighed using a Mettler Balance (Type H16) prior to heat and steam exposure.

In the case of control samples, they were decontaminated and weighed. Since they were assigned as control samples, they were not used for the weight loss experiment; however, they were designated for burst testing in order to determine their strength. Further details are discussed in the results section. In the case of the non-irradiated experiment, the samples were decontaminated and weighed. Then, they were inserted into the sample holder, which can hold a maximum of 4 samples. The sample holder is made of alumina ceramic, and it has a cap with two threaded holes to allow steam to be delivered to the samples in and out through the alumina rods that can handle high temperatures. The sample holder was then inserted into the heating coil to simulate reactor temperature by utilizing the electric heater.

The experimental setup was located at the _L_eft _3_rd (L3) beam port of the nuclear research reactor at RINSC, as shown in Figure 6. Radiation shielding bricks were designed and used to maintain safe conditions for personnel. A heat plate was used to heat deionized water for steam generation. Since the real reactor environment is not considered in this experiment, the steam generator provided a continuous flow of pure steam at 5.63 g/min with 1 atm partial pressure for each experiment's duration. The steam mass flow of 5.63 g/min was measured with ±5% accuracy by dividing the mass deficit of the water by the

duration of steam generation. The sample holder's inserted samples were heated using a Robust Radiator (RHUL-MP2125-4 Model, which is capable of reaching temperatures up to 1700°C) and exposed to a pure steam environment for 8 hours. The robust radiator can reach a maximum power of 1425 Watts, and it requires a 220 V power supply. The robust radiator is enclosed in a FiberFree(TM) ceramic refractory.

A power transformer, temperature, and process controller unit (Eurotherm Bpan-O-120T Model 2416) was utilized for the following tasks: (1) to heat the SiC specimens to the desired temperature; (2) to maintain the same temperature for the duration of the experiment; and (3) to cool down the temperature gradually after the end of the experiment. The gradual cooling down process takes an hour, where temperatures were decreased in 50°C degrees increments. It is worth addressing here

that when the duration of the experiment lapsed (8 hours), the steam generator was disconnected; hence, the samples were not exposed to steam while cooling the SiC samples gradually.

Furthermore, a thermocouple (TC) of type B (capable of measuring temperatures up to 1700°C) was inserted through a hole made specifically for the TC to monitor and maintain temperature. After an hour of cooling down of the specimens, samples were removed from the heater and left overnight to dry. The day after each experiment, the SiC samples were weighed for weight loss analysis. In the case of the "neutron-irradiated samples," the same procedures were followed in which the samples were exposed to steam and high temperatures, but with simultaneous neutron irradiation at the L3 beam port of the nuclear reactor. The nuclear reactor power was in the range of 1.85–2 MW and the neutron flux at the L3 beam port was measured using the gold foil activation technique. The neutron

flux was determined to be 4.37E8 (neutrons/cm^2/s) within 1% absolute accuracy. Therefore, the maximum neutron fluence in which the irradiated samples were exposed to was a fluence of 1.23E13 (neutrons/cm^2).

Furthermore, from a practical perspective, SiC strength is an essential parameter in the design of nuclear fuel rod safety. Hence, we measured the strength of SiC tubular samples by a destructive type of test known as "burst testing"[45] by utilizing a burst testing machine (Model Vishay, Tensile Testing Machine). For performing the tests, polyurethane rods were utilized that had the same diameter; however, the height was cut carefully to acquire a specific volume for each tubular SiC specimen. In order to find the optimal rod height so that when the rod is compressed, it would not barrel out of the tubular SiC specimen several trials were conducted. After finding the optimal volume, each rod was inserted into the hollow volume of the tubular SiC sample, where a load of stainless steel was applied on the rod compressively. This controlled load results in the expansion of the plug radially, which exerts tensile loads on the specimen walls. As soon as the load makes contact with the polyurethane rod, the PC takes readings of the force applied. The speed at which the load was exerted is 2.00 (mm/min). This destructive type of test is used to simulate the internal pressurization of the SiC specimens. The internal pressure (P_f) is calculated as follows:

$$P_f = \frac{F_f}{\pi (r_p)^2} \qquad (4.1)$$

where F_f is the peak load at which the specimen is fractured, and r_p is the radius of the polyurethane rod. For calculating the fracture hoop stress,[50, 51] the thin-walled approach[50] was used since the tubular SiC wall is almost 10% of the tube diameter. The fracture hoop stress is, therefore, calculated as follow:

$$\sigma_{\theta,f} = \frac{P_f \, r_m}{t_{thickness}} \tag{4.2}$$

where r_m is the radius of SiC tube. The r_m is measured from the center of wall thickness, and $t_{thickness}$ is wall thickness.[4, 5]

It is worth addressing that a total of 5 SiC samples gave misleading results due to the polyurethane rod being cut smaller than intended in which the stainless steel rod excreted force directly on the top of SiC tube which resulted in higher peak load readings. Figure 7 shows SiC tubular specimens after being bursted. Figure 7a and 7b show the difference between a successful and failed test in which results from the failed test show rather high peak load values.

5. RESULTS AND ANALYSIS OF EXPERIMENTS

5.1. WEIGHT LOSS

Weight loss is one of the critical physical properties indicative of material's strength; therefore, ceramic SiC cladding must exhibit minimal weight loss under reactor operating conditions for long SMR core lifetime. The results reported here are limited to non-transient analyses. For the weight loss experiment, we divided the samples into two groups: (1) non-irradiated and (2) neutron-irradiated samples to further examine the effect of neutron irradiation on weight loss mechanism.

It is well known that weight loss is a surface phenomenon,[42, 43, 44] therefore, geometry is likely to play a significant role. Therefore, we observed the change of weight (per area) for the samples under investigation. Likewise, the phenomenon is also temperature dependent; hence, data are desired at different temperatures. Throughout the

"weight loss" experiments, we considered this term as "weight loss per area" to understand how the weight of the samples is affected per area.
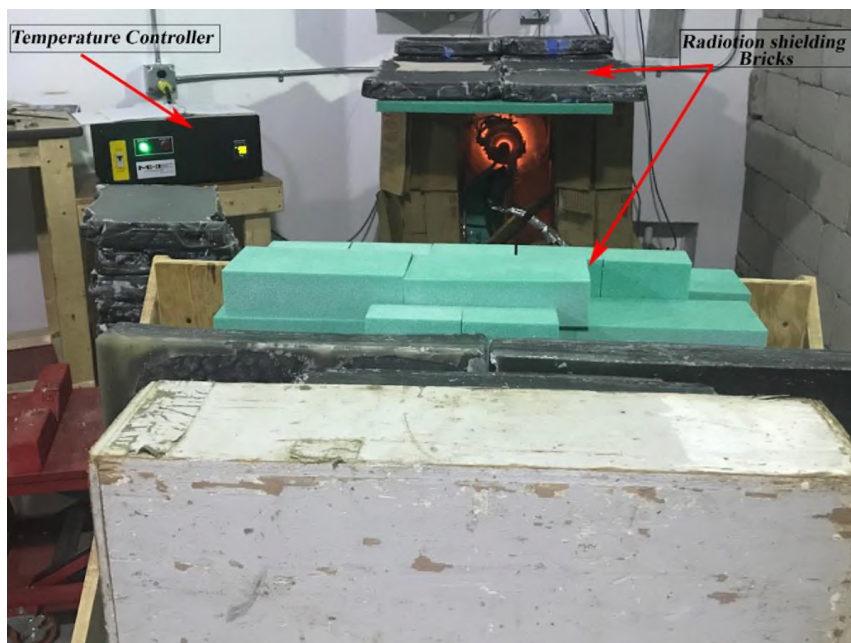
(a)
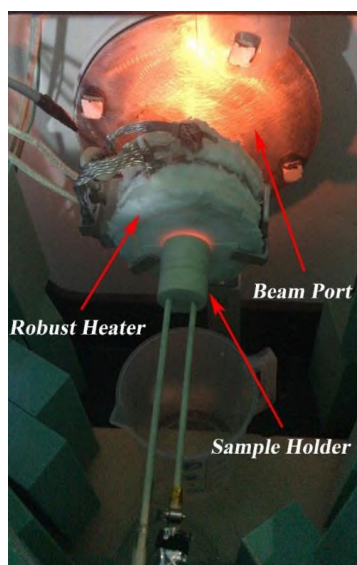
(b)

Figure 6. Experimental setup: (a) L3 beam port location where the experiment was conducted; (b) A close up of the beam port where samples were exposed to steam while heated by the robust heater.

(a)   (b)
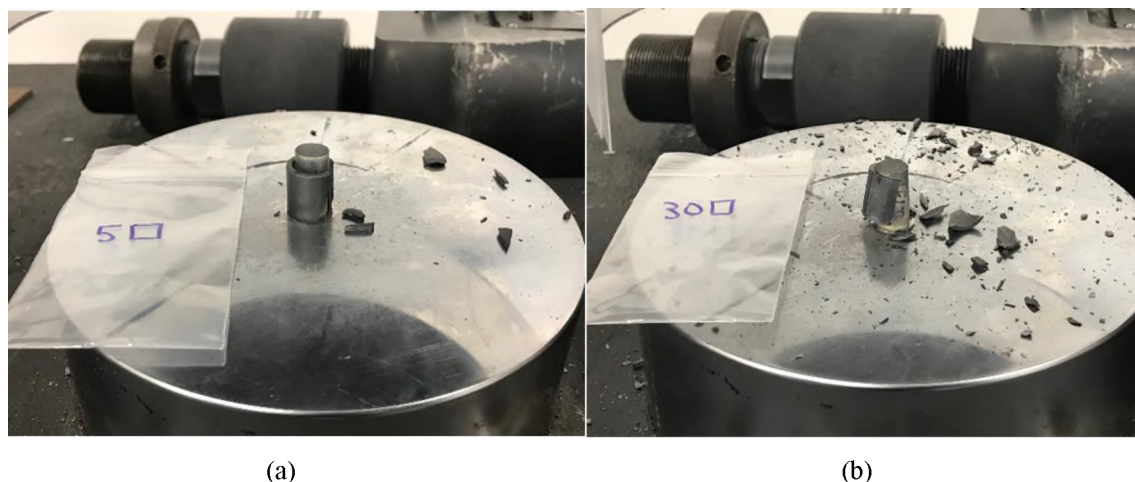
Figure 7. SiC tubes after performing burst testing: (a) A successful bursted SiC specimen; (b) Heavily shattered SiC tube which indicates a failed burst test.

We considered 48 non-irradiated samples for the weight loss experiment and associated standard deviation (SD) values are provided. In this case, our sample sizes range between 0.415–0.438 inch (SD=0.00415), 0.545–0.566 inch (SD=0.00321), and 0.526–0.590 inch (SD=0.0169) for internal diameter, outer diameter, and heights of the samples, respectively. In this experiment, weight loss is directly proportional to the surface area, which is in range between 1.57–1.77 inches^2 (SD=0.0522). Figure 8a shows that weight loss per area is mostly ranged between 0 to -0.1 mg/cm^2. It is seen that weight loss between the samples in the periphery of -0.1 mg/cm^2 varies between 2–6% which can be attributed to the variation in the sample dimensions.

Furthermore, weight loss behavior is also investigated for the total 44 irradiated samples. In this case, internal diameter, outer diameter, and heights range between 0.414–0.431 inch (SD =0.003), 0.541–0.567 inch (SD=0.005), and 0.489–0.580 inch (SD=0.019), respectively for the 44 samples. It has been observed that the overall volume of the irradiated samples is 1.15%–4.88% lower than that of the non-irradiated samples. It can be seen in

Figure 8b that the weight loss behavior is consistent between the irradiated and non-irradiated samples, where weight loss per area is mostly ranged between 0–0.1 mg/cm². The average weight loss for the sample showing non-zero loss was 0.1 mg/cm² and the inter-variation within the samples showing weight loss was in the range of 5–7%. Most importantly, it is also observed that the irradiated samples show 2–10% higher weight loss per area than that of the non-irradiated samples.
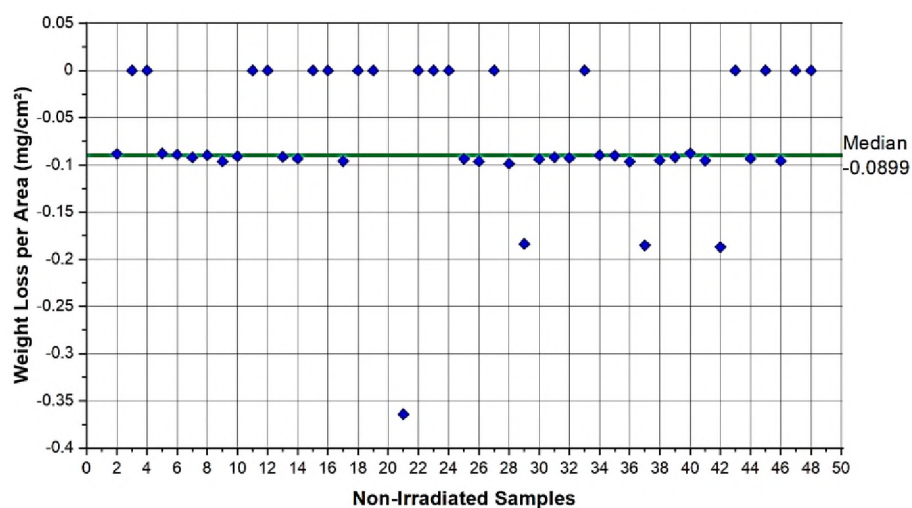
(a)
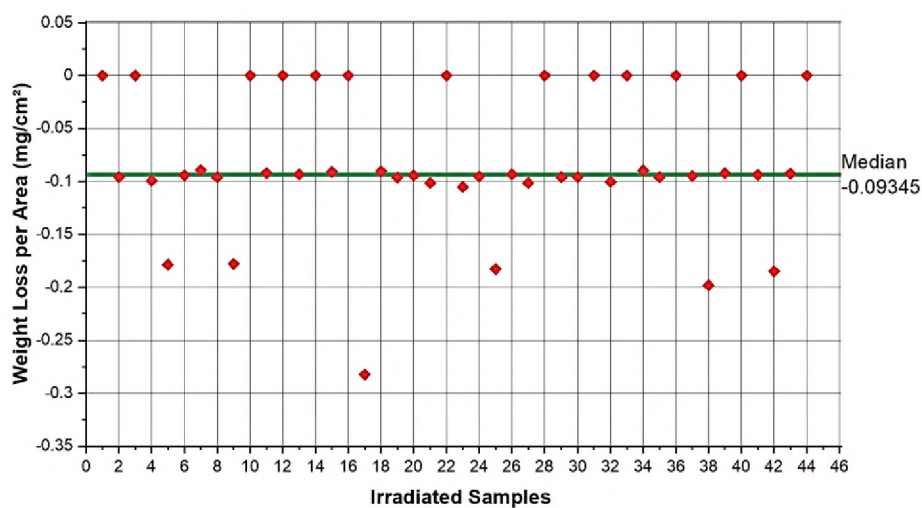
(b)

Figure 8. Weight loss per area for: (a) Non-irradiated samples; (b) Irradiated samples.
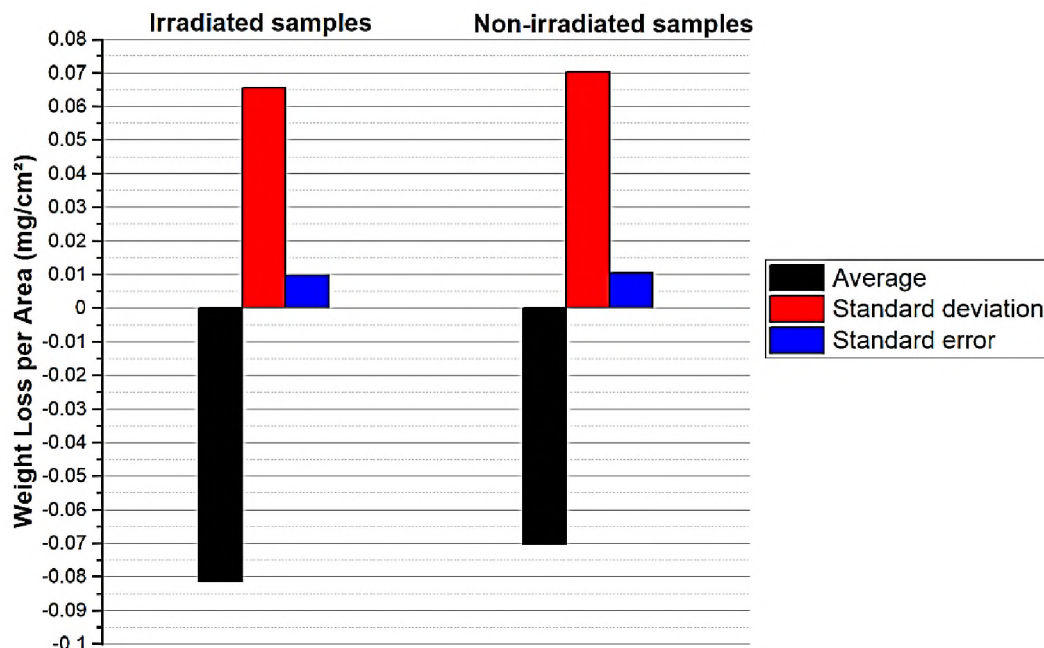
Figure 9. Mean, standard deviation, and standard error for the irradiated and non-irradiated samples.

Since there are differences in the dimensions of the irradiated and non-irradiated samples, there are apparent uncertainties that need to be addressed; therefore, we calculated mean, SD, and standard error (SE) for the irradiated and non-irradiated samples, as shown in Figure 9. It can be observed that average weight loss is 15% higher for irradiated samples, as expected. However, irradiated samples show a 7% lower SD and 5% lower SE values for the weight loss per area.

Moreover, since temperature is one of the prime factors influencing the weight loss of the SiC cladding, we have evaluated the average weight loss of SiC material with respect to temperature, as shown in Figure 10a and Figure 10b. We have considered a medium flow rate (less than 10 g/min) in order to be consistent with the reactor operating flow rate. The results show that the irradiated samples exhibit 10–40% higher weight loss than that of the non-irradiated samples over the range of the associated temperatures. It is also observed that

material loss rates are generally more sensitive at a higher applied temperature than at lower applied temperatures.

Temperature dependence on weight change between irradiated and non-irradiated samples is shown in Figure 11. It can be seen that at lower temperatures and up to 1000°C, positive values are observed, which means the irradiated samples are more prone to weight loss. Up to 1000°C, radiation is more uniform since the sample size is almost unaffected by the radiation due to the accident tolerant behavior of the SiC sample (unlike Zr cladding). In the reactor environment after 1000°C, the fuel and cladding materials are prone to different underlying effects such as fission gas release, porosity, and the possibility of blunt/crack, which are responsible for not having a uniform distribution of radiation through the samples mainly due to the poor thermal contact. It means that up to 1000°C, SiC samples are more tolerant towards radiation, which is also proven by the previous literature and future study will consider the associated uncertainty quantification analysis.[4, 5, 6, 8, 14]

5.2. BURST TESTING

Burst testing[45] has been performed in terms of peak load force, internal pressure, and fracture hoop stress through- out this study. Peak load force is defined as the load at which the specimen is fractured. The fracture hoop stress is the force exerted on every particle in the cylinder wall in both directions (axial and radial). Peak load (N), internal pressure (MPa), and fracture hoop stress (MPa) are investigated for three types of samples: 1. as-received; 2. non-irradiated; 3. irradiated samples. The influence of temperature on sample strength was also considered for irradiated and non-irradiated samples. It should be noted that the Grubbs test[52, 53] was performed in order to confirm that two outliers exist in the data. It was

found that at the 0.05 significance level,[52, 53] the highest values of interest are significant outliers for the non-irradiated (sample 30) and irradiated (sample 1). Therefore, these outliers were replaced with the mean of the group for this analysis of the same temperature. These were true outliers, and the reason behind this is mainly due to an error while cutting the polyurethane rod. The error resulted in producing the final volume of the polyurethane rod being smaller than the calculated volume for the rod to be inserted in the SiC tubular samples for performing the burst testing experiment. Since the polyurethane rod volume was small for these samples, it resulted in high peaking loads because the stainless steel rod from the burst testing machine had more contact with the SiC tubular samples while compressing.
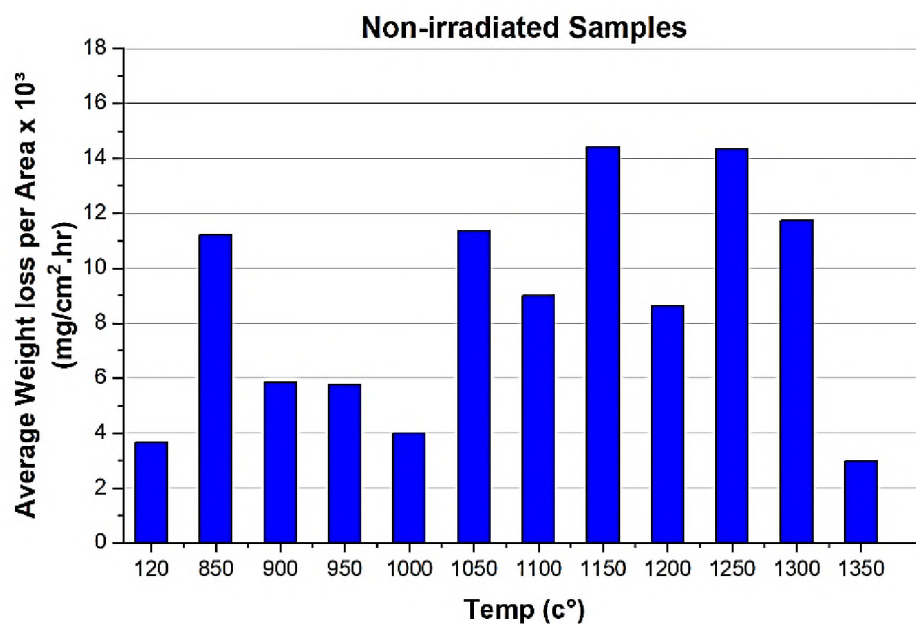
Figure 10. Temperature dependence for samples: (a) Non-irradiated; (b) Irradiated.
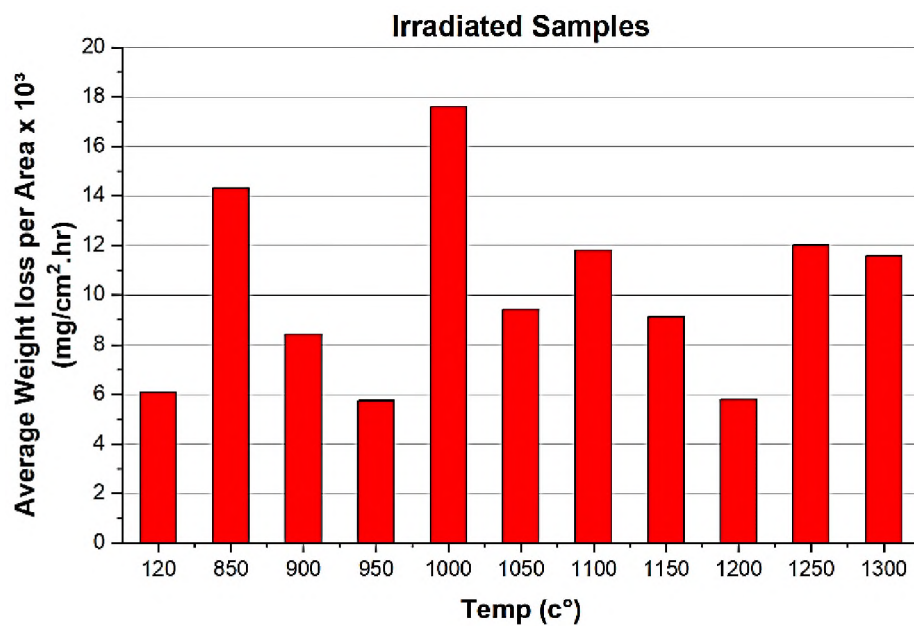
(b)

Figure 10. Temperature dependence for samples: (a) Non-irradiated; (b) Irradiated (cont.).
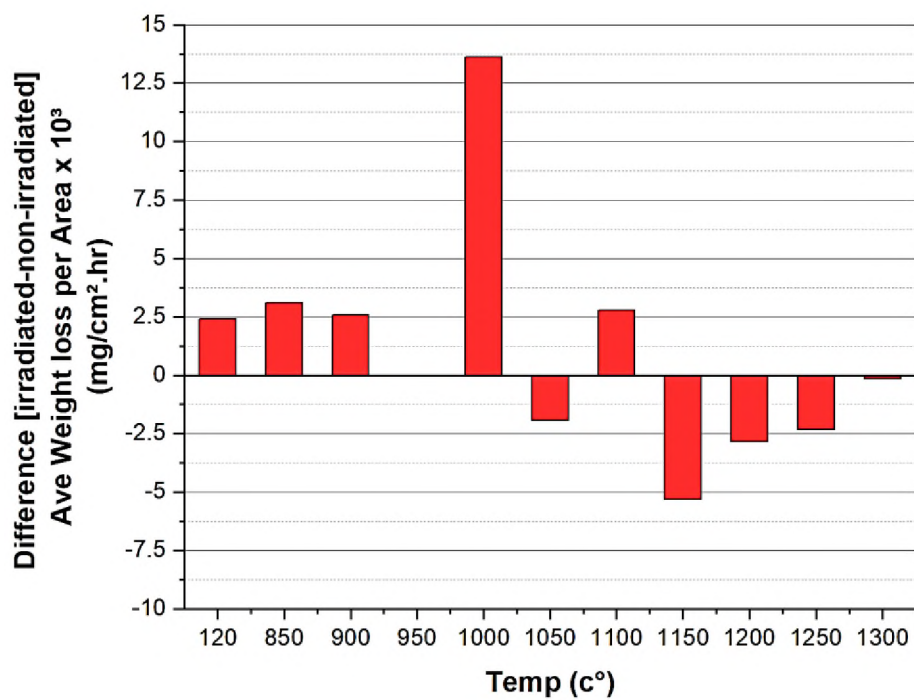
Figure 11. Weight loss dependence on temperature.

5.2.1. As-Received Samples. The burst testing analyses are initiated in our test facility for the as-received samples in order to understand the sample strength without being exposed to pure steam, high temperatures, and neutron irradiation. Table 2 shows as-received sample information for burst testing. In the case of as-received samples, internal diameter, outer diameter, heights and surface area range between 0.418–0.433 inch (SD=0.005), 0.551–0.560 inch (SD=0.003), 0.517–0.587 inch (SD=0.017), and 1.542–1.760 inch² (SD=0.055), respectively. By considering the dimensional uncertainties, It has been observed that the samples show SD between 0.002 to 0.055, and SE ranges from 0.001 to 0.015.

It can be seen for as-received samples that peak load values of SiC samples are mostly in the range of 5000 N, as shown in Figure 12. However, two samples (as-received sample 3 and 32) show considerably higher load of 20K N mainly due to error while cutting the polyurethane rods. Excluding these two data sets of 20K N, it can be seen that the maximum and minimum peak load values are 6890 N and 1718 N, respectively which are 70% higher and 60% lower than the average peak load of 4045 N. In addition, the samples exhibit SD values of 1436 N and SE of 383 N.

Table 2. As-received sample parameters for weight loss and burst testing.

As-received sample number	ID (in)	OD (in)	H (in)
1	0.433	0.556	0.554
2	0.424	0.555	0.55
3	0.424	0.559	0.571
4	0.423	0.559	0.539
21	0.426	0.559	0.549

Table 2. As-received sample parameters for weight loss and burst testing (cont.).

As-received sample number	ID (in)	OD (in)	H (in)
22	0.429	0.56	0.559
23	0.429	0.56	0.552
24	0.422	0.552	0.542
31	0.418	0.553	0.532
32	0.418	0.552	0.548
33	0.425	0.553	0.587
34	0.418	0.553	0.547
35	0.422	0.552	0.517
36	0.42	0.551	0.561
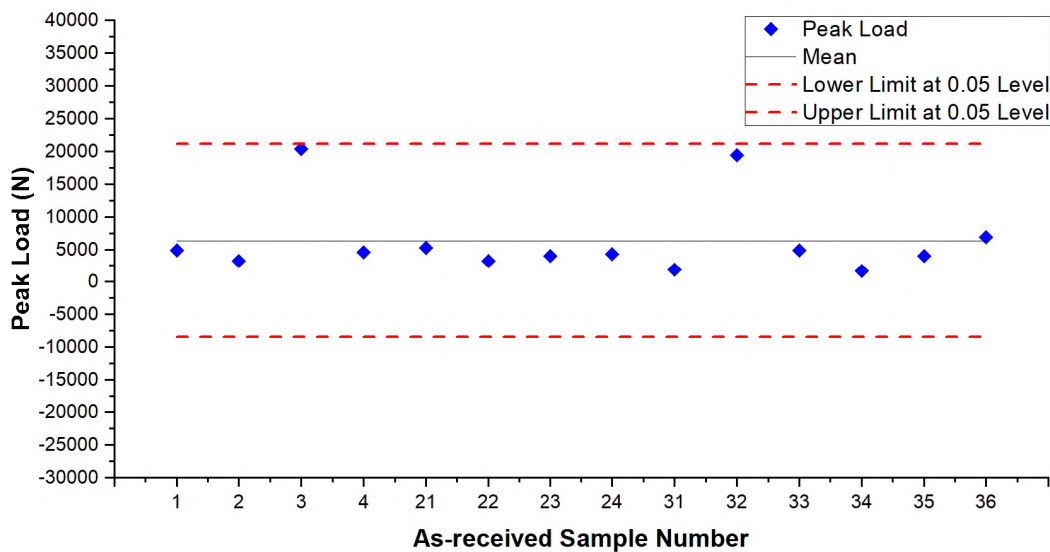
Figure 12. Peak load values with Grubbs test for as-received samples.

Internal pressure and fracture hoop stress are also evaluated, as can be seen in Figure

13a. Fracture hoop stress, also known as breaking stress, is the stress at which a specimen fails

via fracture.[51,54,55] This is usually determined for a given specimen by a tensile test,[56] which charts the stress. In order to be consistent with all the findings from the burst testing samples, fracture stress is calculated by using the thin-wall approach since the wall thickness of the tubular SiC samples are roughly 10-15% of the tube diameter.
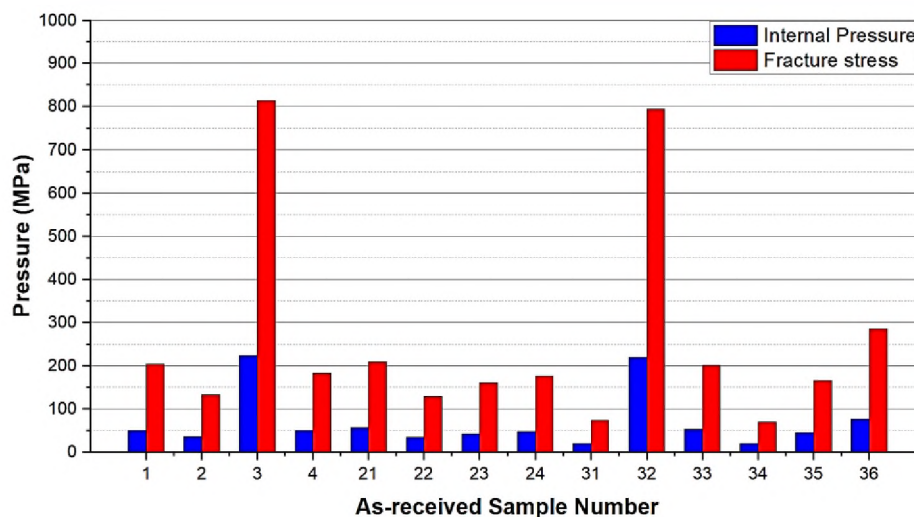
(a)
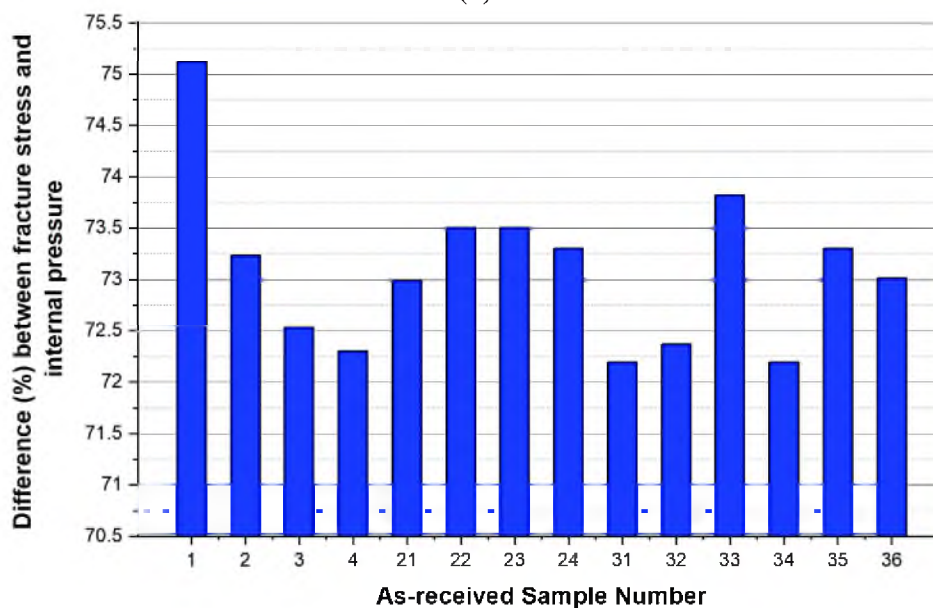
(b)

Figure 13. (a) Internal pressure and fracture hoop stress for as-received samples; (b) Difference between pressure and fracture hoop stress for as-received samples.

Excluding samples 3 and 32, which show significantly higher than average values, Figure 13a shows that internal pressure and fracture stress range between 19–77 MPa (SD= 15.8) and 69–285 MPa (SD= 15.8), respectively, which demonstrates the fact that the highest and lowest ranges of fracture stress values are 72% higher than that of the internal pressure. It can also be seen that fracture hoop stress is consistently 70-75% higher than the internal pressure for all the as-received samples (as can be seen in Figure 13b). These results are well expected since internal pressure is the pressure experienced by the samples' internal surface, whereas fracture hoop stress is the highest tolerant stress faced by the samples before bursting.

5.2.2. Non-Irradiated Samples. Non-Irradiated samples are examined for the peak load testing using the University of Rhode Island's mechanical engineering facilities. Table 3 shows non-irradiated sample information for burst testing. The non-irradiated samples are 48 in total and the highest temperature achieved is 1350°C. In the case of 48 non-irradiated samples, internal diameter, outer diameter, heights and surface area range between 0.415–0.438 inch (SD=0.004), 0.545–0.566 inch (SD=0.003), 0.526–0.590 inch (SD=0.017) and 1.570–1.769 inch^2 (SD=0.052), respectively.

Figure 14a shows that the peak load for most of the samples lies between 5000 to 10000 N. However, one sample shows a peak load in the vicinity of 40K N. After performing the Grubbs test, it can be seen that this sample is a true outlier. The outlier result can be attributed to the error while cutting the polyurethane rod that was used for burst testing. This, in turn, resulted in higher than average of the other samples (as confirmed in Figure 14b). Therefore, the result from sample 30 was replaced with the mean of the samples heated to the same temperature. Besides, it can be observed that the peak

load of non-irradiated SiC samples are 45% higher than the as-received samples. Furthermore, the maximum and minimum peak load values for non-irradiated samples are 9273 N (sample 30) and 2080 N (excluding the high values of sample 11 and 46), respectively, which are 30% higher than the respective as-received samples. It is worthwhile mentioning that the non-irradiated samples exhibit higher SD values than as-received samples (SD= 1436 N vs. 2000 N).

Excluding the high values of sample 11 and 46, Figure 15a shows that internal pressure and fracture stress of non-irradiated samples range between 23–160 MPa and 91–410 MPa, respectively, which demonstrates the fact that non-irradiated samples show at least 20% higher internal pressure and fracture stress values than as-received samples. In addition, consistent with the results of "as-received samples", we see that fracture stress values of non-irradiated samples are almost 70–75% higher than the internal pressure (as seen in Figure 15b), whereas the margin of difference was 70–77% for the as-received samples.

It is important addressing that the higher strength following the exposure to steam arises from the crack blunting effect,[4] which is mainly due to the formation of SiO_2 via oxidation and these findings are in well agreement with the previous studies.[4, 57, 58]

5.2.3. Irradiated Samples. Neutron irradiated information for 44 samples examined with burst testing are shown in Table 4. Internal diameter, outer diameter, heights and surface area for irradiated samples range between 0.380–0.431 inch (SD=0.001), 0.541–0.567 inch (SD=0.001), 0.489–0.580 inch (SD=0.03) and 1.474–1.743 inch^2 (SD=0.09), respectively. It was observed that SiC tubular samples used for neutron

irradiation are smaller in dimensions than as-received and non-irradiated samples. The SiC

samples allocated for irradiation show SE (0.001–0.009).

Table 3. Sample parameters for non-irradiated weight loss and burst testing experiments.

Temperature (c°)	Non-Irradiated sample number	IN (in)	OD (in)	Height (in)
120	2	0.417	0.552	0.589
	3	0.426	0.555	0.539
	4	0.428	0.549	0.541
850	5	0.422	0.554	0.587
	6	0.423	0.555	0.58
	7	0.438	0.566	0.549
	8	0.438	0.555	0.573
900	9	0.425	0.553	0.538
	10	0.425	0.557	0.566
	11	0.416	0.555	0.539
	12	0.415	0.55	0.556
950	13	0.427	0.554	0.565
	14	0.425	0.548	0.56
	15	0.42	0.554	0.539
	16	0.424	0.545	0.545
1000	17	0.424	0.55	0.543
	18	0.425	0.554	0.54
	19	0.424	0.558	0.579
1050	21	0.426	0.557	0.565
	22	0.422	0.554	0.57
	23	0.422	0.552	0.565
	24	0.425	0.554	0.548
1100	25	0.424	0.554	0.552
	26	0.424	0.558	0.535
	27	0.424	0.554	0.568
	28	0.426	0.552	0.526
1150	29	0.424	0.553	0.564
	30	0.424	0.557	0.548
	31	0.427	0.551	0.566
	32	0.422	0.554	0.559

Table 3. Sample parameters for non-irradiated weight loss and burst testing experiments (cont.).

Temperature (c°)	Non-Irradiated sample number	IN (in)	OD (in)	Height (in)
1200	33	0.424	0.553	0.588
	34	0.424	0.554	0.577
	35	0.42	0.554	0.574
	36	0.424	0.551	0.538
1250	37	0.42	0.556	0.557
	38	0.424	0.554	0.545
	39	0.42	0.551	0.567
	40	0.419	0.554	0.59
1300	41	0.425	0.556	0.54
	42	0.423	0.552	0.555
	43	0.419	0.557	0.538
	44	0.425	0.556	0.552
1350	45	0.423	0.556	0.534
	46	0.425	0.557	0.538
	47	0.423	0.555	0.566
	48	0.426	0.555	0.553
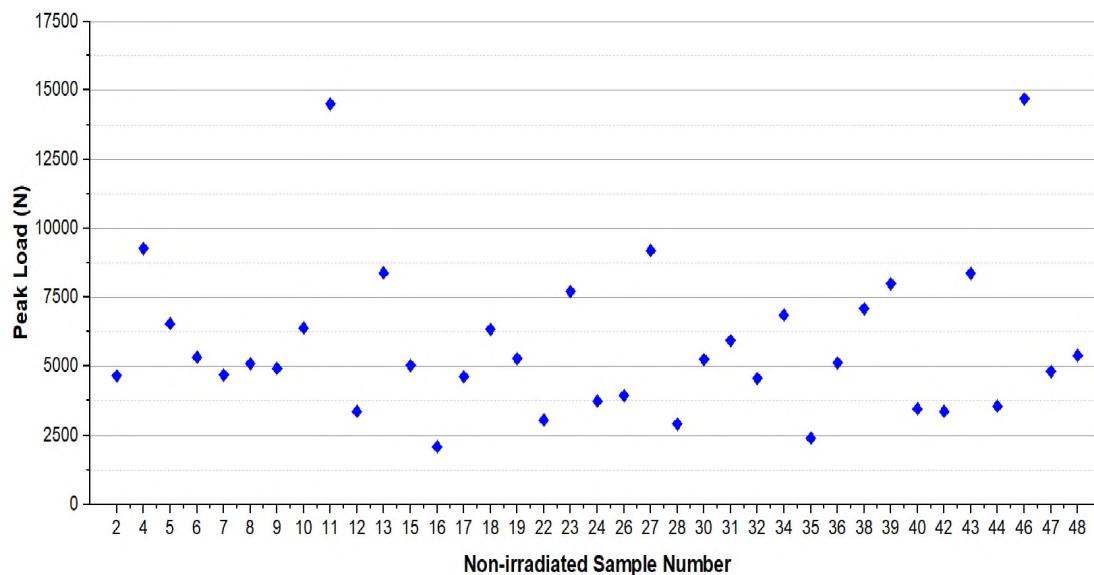
(a)

Figure 14. (a) Peak load for non-irradiated samples; (b) Grubbs test results for non-irradiated samples.
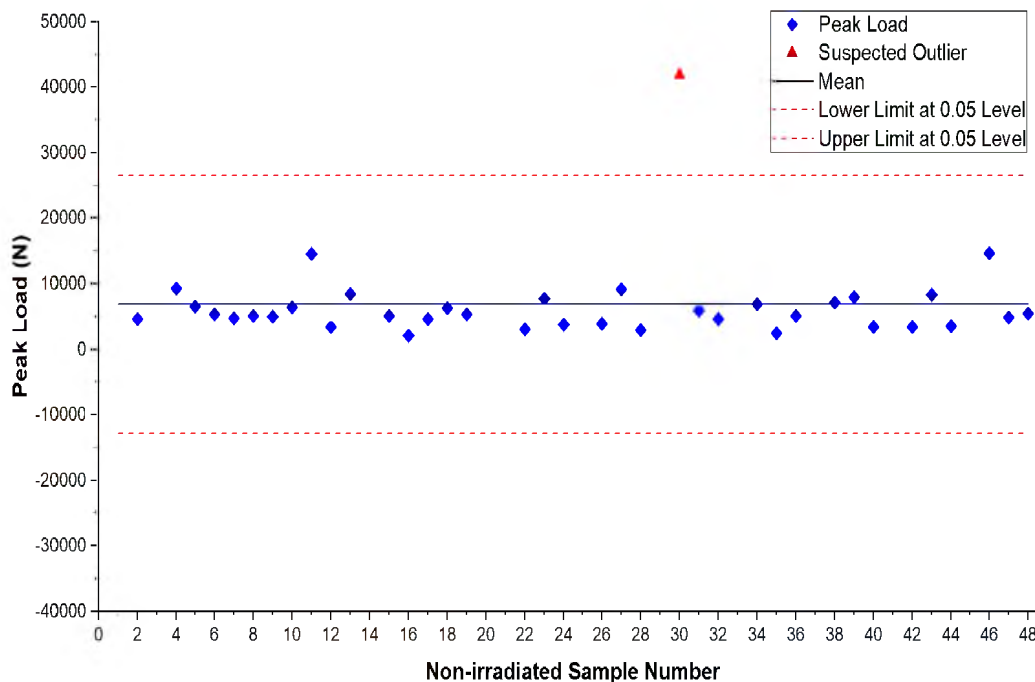
(b)

Figure 14. (a) Peak load for non-irradiated samples; (b) Grubbs test results for non-irradiated samples (cont.).

A maximum temperature of 1300°C was achieved for irradiated samples. We could not achieve higher temperatures due to the malfunction of the coil in the heater. From Figure 16a, it is observed that for the irradiated samples, the peak load (N) is ranged between 5000–10000 N, which is similar to the range of non-irradiated and as-received samples (5000–9000 N). However, sample 1 shows a high peak load with 22593 N. After performing the Grubbs test, it is found that sample 1 is a true outlier. Hence, its value is exchanged with the temperature group mean as addressed previously. The Grubbs test results can be seen in Figure 16b. Furthermore, the maximum and minimum peak load values for non-irradiated samples are 11617 N and 2324 N, respectively, which are 10–15% higher than the respective non-irradiated samples. Irradiated samples exhibit

significantly lower SD values than as-received and non-irradiated samples. It is also seen in Figure 17a that maximum fracture stress and internal pressure values are 468 MPa and 131 MPa, respectively, where fracture stress is 75% higher than the internal pressure (Figure 17b). This finding is consistent with respective non-irradiated and as-received samples. Most importantly, the maximum fracture stress and internal pressure values exhibit SD of 13 and 4 MPa, respectively, which are comparable to the non-irradiated samples.

(a)

(b)
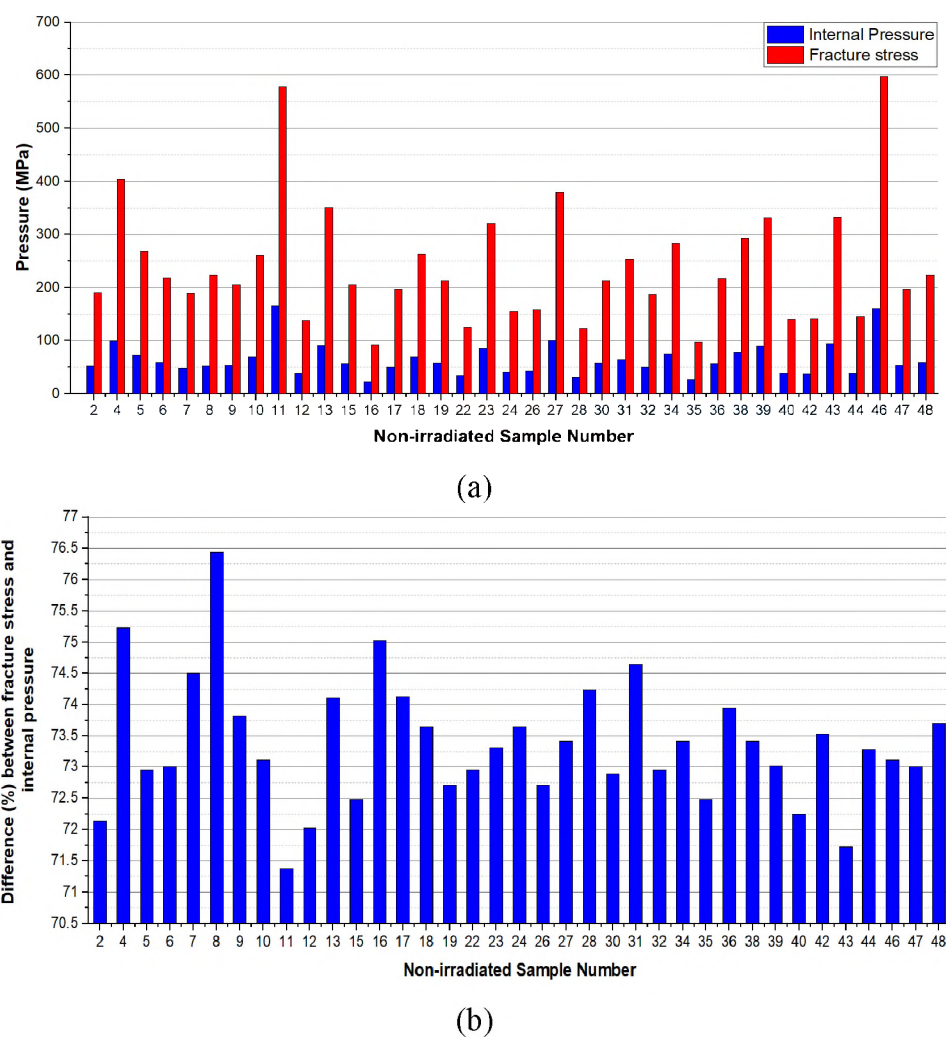
Figure 15. (a) Pressure and fracture hoop stress for non-irradiated samples; (b) Difference between pressure and fracture hoop stress for non-irradiated samples.

Table 4. Sample parameters for irradiated weight loss and burst testing experiments.

Temperature (c°)	Irradiated sample number	ID (in)	OD (in)	Height (in)
120	1	0.424	0.555	0.543
	2	0.422	0.555	0.54
	3	0.426	0.556	0.541
	4	0.419	0.556	0.521
850	5	0.423	0.554	0.578
	6	0.423	0.554	0.549
	7	0.423	0.557	0.577
	8	0.42	0.554	0.539
900	9	0.429	0.554	0.58
	10	0.42	0.555	0.567
	11	0.42	0.555	0.562
	12	0.426	0.557	0.542
950	13	0.419	0.554	0.555
	14	0.424	0.554	0.565
	15	0.421	0.549	0.573
	16	0.423	0.557	0.557
1000	17	0.423	0.561	0.544
	18	0.424	0.549	0.576
	19	0.424	0.543	0.546
	20	0.424	0.557	0.545
1050	21	0.42	0.55	0.515
	22	0.424	0.555	0.55
	23	0.429	0.559	0.489
	24	0.421	0.548	0.549
1100	25	0.425	0.567	0.554
	26	0.421	0.554	0.554
	27	0.431	0.544	0.518
	28	0.424	0.553	0.553
1150	29	0.424	0.553	0.54
	30	0.428	0.558	0.537
	31	0.429	0.558	0.539
	32	0.429	0.559	0.512

Table 4. Sample parameters for irradiated weight loss and burst testing experiments (cont.).

Temperature (c°)	Irradiated sample number	ID (in)	OD (in)	Height (in)
1250	37	0.418	0.554	0.547
	38	0.42	0.554	0.523
	39	0.424	0.55	0.564
	40	0.425	0.552	0.543
1300	41	0.423	0.553	0.554
	42	0.424	0.552	0.561
	43	0.426	0.557	0.556
	44	0.42	0.554	0.552
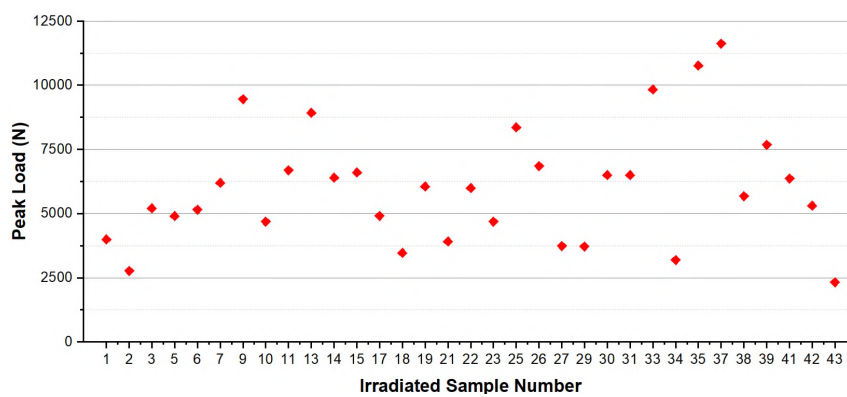
(a)
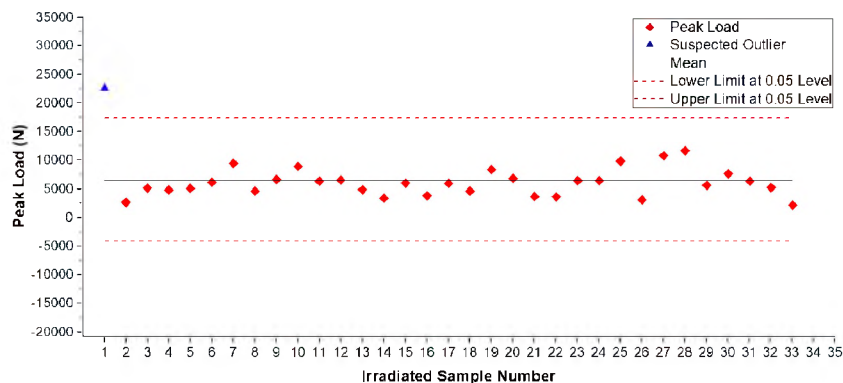
(b)

Figure 16. (a) Peak load for irradiated samples; (b) Grubbs test results for irradiated samples.
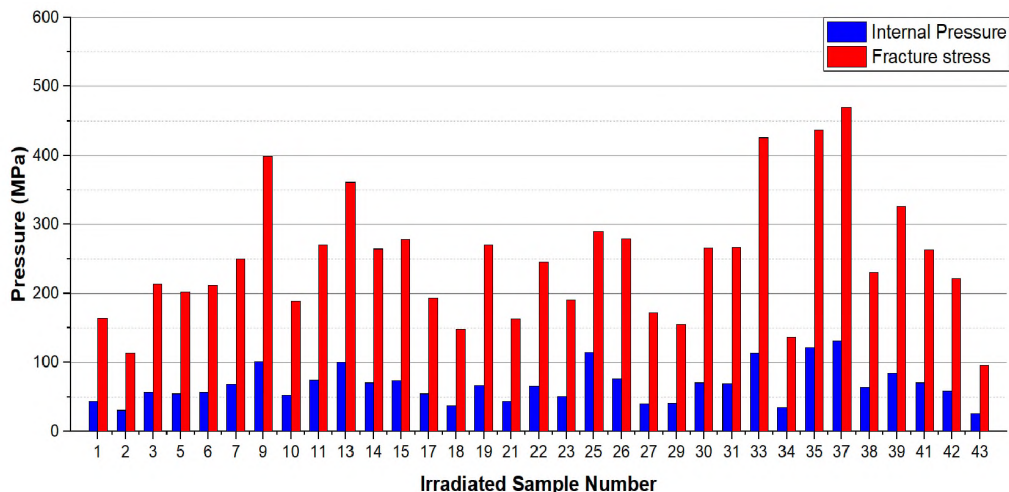
(a)
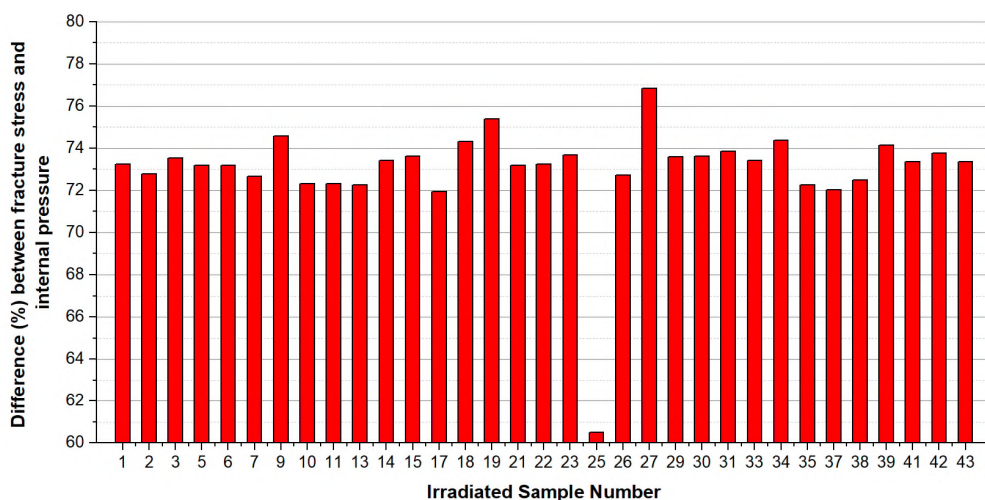
(b)

Figure 17. (a) Internal pressure and fracture hoop stress for irradiated samples; (b) Difference between pressure and fracture hoop stress for irradiated samples.

Furthermore, internal pressure and fracture hoop stress for non-irradiated and irradiated samples with respect to temperature can be seen in Figure 18. The maximum internal pressure (average) and fracture stress (average) over the temperature ranges are comparable (90 N and 340 MPa) for both the non-irradiated and irradiated sample types; however, irradiated samples show slightly higher values.
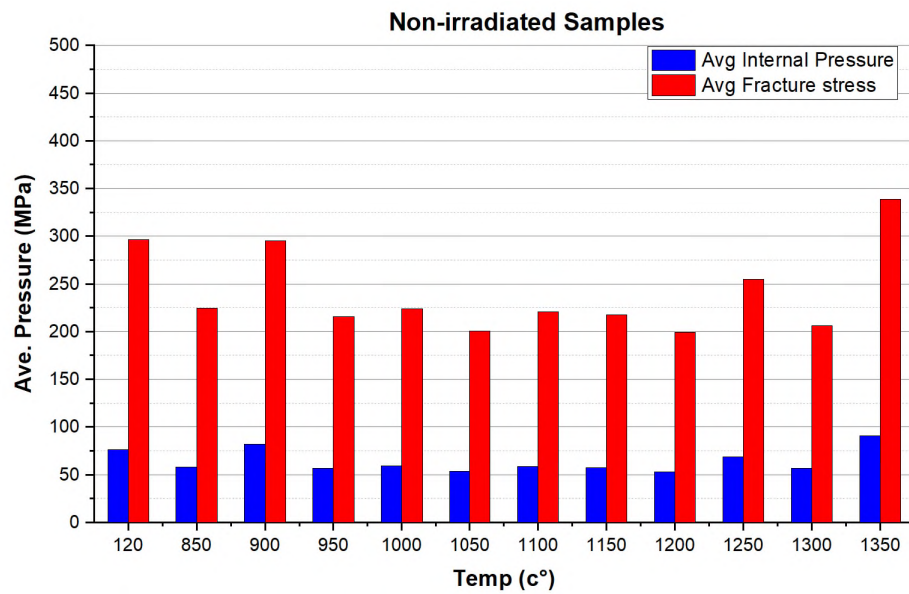
(a)
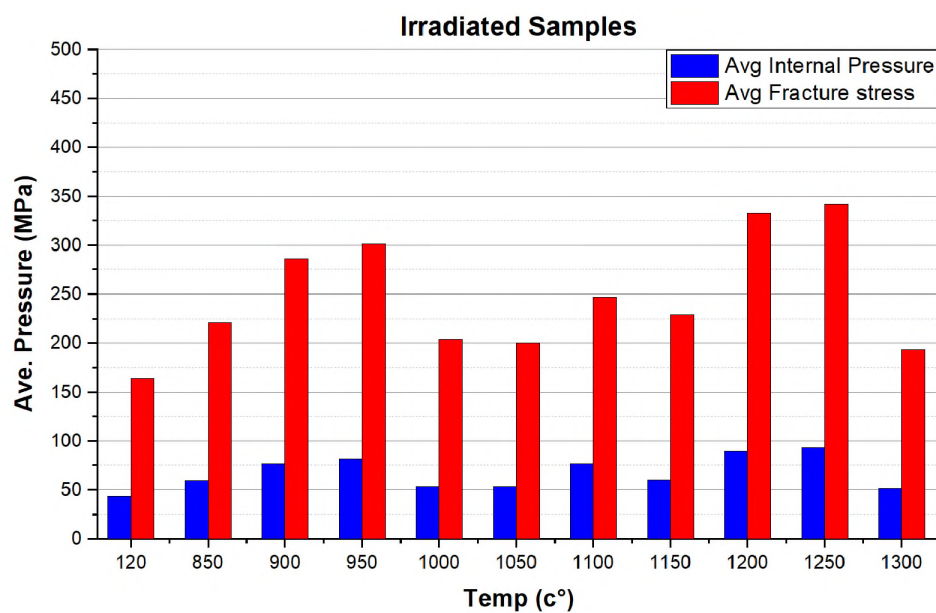
(b)

Figure 18. Internal pressure and fracture hoop stress with respect to temperature: (a) non-irradiated samples; (b) irradiated samples.

6. CONCLUSIONS

This paper investigates the behavior of accident-tolerant cladding for long-life SMR core for the possible application of marine propulsion of 15–20+ years. This study is divided into two parts: (1) reactor physics modeling of the accident–tolerant cladding candidates, and (2) experimental analyses of silicon carbide cladding material. Reactor physics modeling (first part of the study) confirms the following:

- Silicon carbide cladding exhibits a higher initial reactivity in SMR core than that of the other accident-tolerant candidate claddings.

- Silicon Carbide cladding provides the highest achievable discharge burnup in SMR core out of all other accident-tolerant candidate claddings, making this cladding the natural choice for experimental investigation.

For the experimental investigation (the second part of the study), weight loss, and burst testing of the tubular sintered SiC samples at 1 atm with a temperature range of 120°C, 850°C to 1300°C are examined. For the weight loss experiment, we have considered two types of samples: (1) non-irradiated and (2) neutron-irradiated samples. The key results are the following:

- Weight loss is sensitive to the sample dimensions, and irradiated samples show 2–10% higher weight loss per area than that of the non-irradiated samples.

- Considering the medium flow rate (less than 10 g/min), irradiated samples exhibit 10–40% higher weight loss than that of the non-irradiated samples over the range of temperatures (120°C, 850°C to 1350°C).

- Material loss rates are generally more sensitive at a higher temperature than at lower temperatures, and irradiated samples are more prone to weight loss.

For the burst testing investigations, experiments are conducted for (1) As–received samples (2) Non-irradiated samples, and (3) Irradiated samples. The key results are:

- Fracture hoop stress is consistently 70–75% higher than the internal pressure for all the as-received samples.

- The maximum internal pressure (average) and fracture stress (average) over the temperature ranges are comparable for both the non-irradiated and irradiated sample types; however, irradiated samples show slightly higher values.

Hence, based on the experimental and computational investigations, it is concluded that SiC has the potential to be a preferred accident-tolerant cladding material choice for the long lifetime reactor core operation.

It is worth emphasizing that the SiC experiments were conducted in the Rhode Island Nuclear Science Center. Although SiC material will be utilized for long-life and high burnup cores, SiC experiments are limited to 8 hours to understand its fundamental behavior in terms of weight loss and mechanical strength, which provides us a clear indication of the SiC behavior under the harsh environment.

Future work will consider the following:

- Extend the reactor physics modeling from a 2D assembly investigation to a whole core.

- Associated uncertainty quantification analysis of the samples.

- Operational extension (up to 72 hours) of the experiments in one of the US National Labs.

- In order to understand the micro-structural properties of the SiC specimens used in this experiment, we will investigate the SiC materials' properties using Scanning electron microscopy (SEM), Raman spectroscopy, and Electron paramagnetic resonance spectroscopy (EPR).

REFERENCES

[1] Terrani, K. A. Accident tolerant fuel cladding development: Promise, status, and challenges. *Journal of Nuclear Materials* 501, 13–30 (2018).

[2] Andrews, N., Pilat, E., Shirvan, K. & Kazimi, M. Impact of SiC cladding on plutonium burning in a thorium fueled PWR. In *Proc. ICAPP 2014*, Charlotte, USA (2014).

[3] Pint, B. A., Terrani, K. A., Yamamoto, Y. & Snead, L. L. Material selection for accident tolerant fuel cladding. *Metallurgical and Materials Transactions E* 2, 190–196 (2015).

[4] Lee, Y. et al. Oxidation behavior of sintered tubular silicon carbide in pure steam I: Experiments. *Ceramics International* 42, 1916–1925 (2016).

[5] Lee, Y., McKrell, T. J. & Kazimi, M. S. Oxidation behavior of sintered tubular silicon carbide in pure steam II: Weight-loss correlation developments. *Ceramics International* 42, 4679–4689 (2016).

[6] Sukjai, Y. *Silicon carbide performance as cladding for advanced uranium and thorium fuels for light water reactors*. Ph.D. thesis, Massachusetts Institute of Technology (2014).

[7] Li, S. et al. Microstructural evolution of coating-modified 3D C/SiC composites after annealing in wet oxygen at different temperatures. *Corrosion Science* 52, 2837–2845 (2010).

[8] Qiang, X. et al. A modified dual-layer SiC oxidation protective coating for carbon/carbon composites prepared by one-step pack cementation. *Corrosion Science* 53, 523–527 (2011).

[9] Hou, X.-m. & Chou, K.-C. A simple model for the oxidation of carbon-containing composites. *Corrosion Science* 52, 1093–1097 (2010).

[10] Hollnagel, E. & Fujita, Y. The fukushima disaster–systemic failures as the lack of resilience. *Nuclear Engineering and Technology* 45, 13–20 (2013).

[11] Yao, R., Feng, Z., Chen, L., Zhang, Y. & Zhang, B. Oxidation behavior of hi-nicalon SiC monofilament fibres in air and o2–h2o–ar atmospheres. *Corrosion Science* 57, 182–191 (2012).

[12] Yang, X. et al. Resistance to oxidation and ablation of SiC coating on graphite prepared by chemical vapor reaction. *Corrosion Science* 75, 16–27 (2013).

[13] Charpentier, L., Dawi, K., Balat-Pichelin, M., Bˆeche, E. & Audubert, F. Chemical degradation of SiC/SiC composite for the cladding of gas-cooled fast reactor in case of severe accident scenarios. *Corrosion Science* 59, 127–135 (2012).

[14] Narushima, T., Goto, T., Hirai, T. & Iguchi, Y. High-temperature oxidation of silicon carbide and silicon nitride. *Materials transactions*, JIM 38, 821–835 (1997).

[15] Tortorelli, P. F. & More, K. L. Effects of high water-vapor pressure on oxidation of silicon carbide at 1200Âř c. *Journal of the American Ceramic Society* 86, 1249–1255 (2003).

[16] Opila, E. J. & Hann Jr, R. E. Paralinear oxidation of CVD SiC in water vapor. *Journal of the American Ceramic Society* 80, 197–205 (1997).

[17] Opila, E. J. Volatility of common protective oxides in high-temperature water vapor: current understanding and unanswered questions. In *Materials Science Forum*, vol. 461, 765–774 (Trans Tech Publ, 2004).

[18] Terrani, K. A. et al. Silicon carbide oxidation in steam up to 2 MPa. *Journal of the American Ceramic Society* 97, 2331–2352 (2014).

[19] MacDonald, P. & Lee, C. Use of thoria-urania fuels in PWRs: A general review of a NERI project to assess feasible core designs, economics, fabrication methods, in-pile thermal/mechanical behavior, and waste form characteristics. *Nucl. Technol.* 147, 1–7 (2004).

[20] Alam, S. B. et al. Small modular reactor core design for civil marine propulsion using micro-heterogeneous duplex fuel. Part I: Assembly-level analysis. *Nucl Eng Des.* 346, 157–175 (2019).

[21] Alam, S. B. et al. Small modular reactor core design for civil marine propulsion using micro-heterogeneous duplex fuel. Part II: Whole-core analysis. *Nucl Eng Des.* 346, 176–191 (2019).

[22] Peakman, A., Owen, H. & Abram, T. The core design of a small modular pressurised water reactor for commercial marine propulsion. *Progress in Nuclear Energy* 113, 175–185 (2019).

[23] Alam, S. B. The Design of Reactor Cores for Civil Nuclear Marine Propulsion. Ph.D. thesis, University of Cambridge, Cambridge, UK (2018).

[24] Alam, S. B., Goodwin, C. S. & Parks, G. T. Parametric neutronics analyses of lattice geometry and coolant candidates for a soluble-boron-free civil marine SMR core using micro-heterogeneous duplex fuel. *Annals of Nuclear Energy* 129, 1–12 (2019).

[25] Alam, S. B., Goodwin, C. S. & Parks, G. T. Assembly-level analyses of accident-tolerant cladding concepts for a long-life civil marine SMR core using micro-heterogeneous duplex fuel. *Prog Nucl Energ* 111, 24–41 (2019).

[26] Cheng, T., Keiser, J., Brady, M., Terrani, K. & Pint, B. Oxidation of fuel cladding candidate materials in steam environments at high temperature and pressure. *J. Nucl. Mater.* 427, 396–400 (2012).

[27] Pint, B., Terrani, K., Brady, M., Cheng, T. & Keiser, J. High temperature oxidation of fuel cladding candidate materials in steam-hydrogen environments. *J. Nucl. Mater.* 440, 420–427 (2013).

[28] Alam, S. B., de Oliveira, R. G., Goodwin, C. S. & Parks, G. T. Coupled neutronic/thermal-hydraulic hot channel analysis of high power density civil marine SMR cores. *Annals of Nuclear Energy* 127, 400–411 (2019).

[29] Otto, R. T. *Core Optimization in a Thorium-based Civil Marine Propulsion Reactor*. Master's thesis, Department of Engineering, University of Cambridge (2013).

[30] Alam, S. B., Parks, G. T., Almutairi, B. & Goodwin, C. S. Neutronic assessment of accident-tolerant cladding concepts for civil nuclear marine propulsion cores. Part I: Reactivity & spectral hardening. *In Proc. PHYSOR* 2018, 3142–3153 (Cancun, Mexico, 2018).

[31] Alam, S. B., Parks, G. T., Almutairi, B. & Goodwin, C. S. Neutronic assessment of accident-tolerant cladding concepts for civil nuclear marine propulsion cores. Part II: Rim effect & reactivity feedback analysis. *In Proc. PHYSOR* 2018, 3154–3165 (Cancun, Mexico, 2018).

[32] Alam, S. B., Ridwan, T., Parks, G. T., Almutairi, B. & Goodwin, C. S. High power density reactor core design for civil nuclear marine propulsion. Part I: Assembly-level analysis. *In Proc. PHYSOR* 2018, 46–57 (Cancun, Mexico, 2018).

[33] Alam, S. B., Ridwan, T., Parks, G. T., Almutairi, B. & Goodwin, C. S. High power density reactor core design for civil nuclear marine propulsion. Part II: Whole-core analysis. In *Proc. PHYSOR* 2018, 58–69 (Cancun, Mexico, 2018).

[34] Alam, S. B., Lindley, B. A. & Parks, G. T. Neutronic performance of high power density marine propulsion cores using UO2 and microheterogeneous ThO2-UO2 duplex fuels. In *Proc. PHYSOR* 2016, 3519–3531 (Sun Valley, Idaho, USA, 2016).

[35] Alam, S. B., Parks, G. T. & Lindley, B. A. Hot assembly and whole-core thermal-hydraulic analysis of a high power density marine core with neutronic/thermal-hydraulic coupling. In *Proc. PHYSOR* 2016, 3506–3518 (Sun Valley, Idaho, USA, 2016).

[36] Griffith, G. W. US department of energy accident resistant SiC clad nuclear fuel development. Tech. Rep., Idaho National Laboratory (2011).

[37] Mohamed, H. Developing an optimised pin-type fuel assembly design for a small fluoride salt cooled high temperature reactor. Tech. Rep., PhD First Year Report, Department of Engineering, University of Cambridge (2013).

[38] Farzbod, F., Reese, S. J., Hua, Z., Khafizov, M. & Hurley, D. H. Advanced measurements of silicon carbide ceramic matrix composites. Tech. Rep., Idaho National Laboratory (2012).

[39] Bragg-Sitton, S. et al. Silicon carbide gap analysis and feasibility study. Tech. Rep., INL/EXT-13-29728, in, Idaho National Laboratory, Idaho Falls (2013).

[40] Merrill, B. J., Bragg-Sitton, S. M. & Humrickhouse, P. W. Modification of melcor for severe accident analysis of candidate accident tolerant cladding materials. *Nuclear Engineering and Design* 315, 170–178 (2017).

[41] Katoh, Y., Wilson, D. F. & Forsberg, C. W. Assessment of silicon carbide composites for advanced salt-cooled reactors. *ORNL/TM-2007/168* 47–58 (2007).

[42] Nagano, T., Kaneko, K., Zhan, G.-D. & Mitomo, M. Effect of atmosphere on weight loss in sintered silicon carbide during heat treatment. *Journal of the American Ceramic Society* 83, 2781–2787 (2000).

[43] Nunes, P. & Ramanathan, L. Corrosion behavior of alumina-aluminum and silicon carbide-aluminum metal-matrix composites. *Corrosion* 51, 610–617 (1995).

[44] Keppeler, M. et al. High temperature mechanical behaviour of liquid phase sintered silicon carbide. *Journal of the European Ceramic Society* 18, 521–526 (1998).

[45] Alva, L. H., Huang, X., Jacobsen, G. M. & Back, C. A. High pressure burst testing of SiCf –SiCm composite nuclear fuel cladding. *Advancement of Optical Methods in Experimental Mechanics* 3, 387–393 (2015).

[46] Zhang, J., Jiang, D., Lin, Q., Chen, Z. & Huang, Z. Properties of silicon carbide ceramics from gelcasting and pressureless sintering. *Materials & Design* 65, 12–16 (2015).

[47] Guo, X., Cai, X., Zhu, L., Zhang, L. & Yang, H. Preparation and properties of SiC honeycomb ceramics by pressureless sintering technology. *Journal of Advanced Ceramics* 3, 83–88 (2014).

[48] Ceramics, S.-G. Hexoloy SE SiC material (2020).URL https://www.ceramicsrefractories.saint-gobain.com/products/hexoloy-sic materials/grades/se.

[49] TECDOC, I. Use of research reactors for neutron activation analysis. IAEA, Vienna (2001).

[50] Byun, T. S., Lara-Curzio, E., Lowden, R. A., Snead, L. L. & Katoh, Y. Miniaturized fracture stress tests for thin-walled tubular SiC specimens. *Journal of nuclear materials* 367, 653–658 (2007).

[51] Hong, S.-G., Byun, T.-S., Lowden, R. A., Snead, L. L. & Katoh, Y. Evaluation of the fracture strength for silicon carbide layers in the tri-isotropic-coated fuel particle. *Journal of the American Ceramic Society* 90, 184–191 (2007).

[52] Frank, G. Procedures for detecting outlying observations in samples. *Technometrics* 11, 1–21 (1969).

[53] Stefansky, W. Rejecting outliers in factorial designs. *Technometrics* 14, 469–479 (1972).

[54] Priddle, E. Effect of multiaxial stresses on the fracture strength of silicon carbide. *Journal of Strain Analysis* 4, 81–87 (1969).

[55] Stempien, J. D., Carpenter, D. M., Kohse, G. & Kazimi, M. S. Characteristics of composite silicon carbide fuel cladding after irradiation under simulated pwr conditions. *Nuclear technology* 183, 13–29 (2013).

[56] Rahman, M. H. & Al Rashed, H. M. Characterization of silicon carbide reinforced aluminum matrix composites. *Procedia Engineering* 90, 103–109 (2014).

[57] Easler, T., Bradt, R. & Tressler, R. Strength distributions of SiC ceramics after oxidation and oxidation under load. *J. Am. Ceram. Soc.* 64, 731–734 (1981).

[58] Kim, H. & Moorehead, A. Effects of gaseous corrosion on the strength of SiC and Si3N4. *Ceram. Trans.* 10, 81–96 (1990).

SECTION

2. CONCLUSION

This dissertation explores the physical behavior and characterization of neutron-irradiated accident tolerant nuclear fuel cladding for high burnup application of small modular reactor core as well as characterizing radiation detector deadtime. Testing of GM counter was added to this effort to ensure safe handling of neutron-irradiated materials. Since GM detector is generally used as survey meter in similar situations, deadtime was investigated for the reliability of GM counters. At high count rates, GM detectors suffer from deadtime phenomenon in which a number of radiation events go undetected, as described in previous sections. These undetected events lead to an underestimation of dose rate and possible health risk. Therefore, a fundamental understanding of deadtime behavior is crucial. This led to the design of the first study.

In the first study, the pulse shape properties generated by a GM detector due to radiation exposure were investigated. Background radiation and two radioactive sources (^{137}Cs and ^{60}Co) were examined in this study. An oscilloscope was utilized to capture and record the pulse shape properties manually.

This study was performed in order to: (1) understand pulse shape dependence on operating voltage, (2) confirm that not all pulses generated by a GM counter are identical (3) assess if these pulse shape properties follow distinct patterns similar to deadtime behavior reported by a previous study, as discussed in previous sections. Deadtime observation study concluded that there are three distinct deadtime regions depending on the operating voltage. In the first region, at low applied voltages, deadtime is reduced with

increasing voltage. In this region, it is found that pulse width and fall time were also decreasing with increasing voltage. In the second region, the region of constant minimum deadtime, it was found that the pulse tail has vanished while pulse width was observed to be at its minimum. In the third region, at higher applied voltages, it is seen that the second pulse (after initial pulse) showed a reduction in its width.

Furthermore, this study confirmed that the general belief that all pulses generated by a GM detector due to radiation exposure are identical is questionable. Also, based on the data collected, it is inferred that there is a strong correlation between pulse shape properties and detector deadtime. Results from this work was published in Paper I. However, in order to identify a relationship between pulse shape properties, operating voltage, and detector deadtime, a more robust experiment design was required. This ultimately led to the design of the second study.

In the second study, to better understand the behavior of deadtime, simultaneous measurements of deadtime and pulse shape characteristics were required to develop a relationship between operating voltage, deadtime, and pulse shape properties. This study was divided into two parts. The first part evaluated deadtime dependence on operating voltage, while the second part analyzed pulse shape properties. In order to accomplish these two tasks and generate more data for in-depth analysis of deadtime and pulse shape properties, the oscilloscope used to capture and record the pulses was set to automatic measurement. Also, four radioactive sources (^{204}Tl, ^{137}Cs, ^{22}Na, ^{54}Mn) were utilized for deadtime measurement based on the two-source method.

For the first part, a peculiar relationship between deadtime and the operating voltage was observed. At 650 V, deadtime reached a minimum value for three radioactive

sources (22 µs for ^{204}Tl, 26 µs for ^{137}Cs, 9 µs for ^{22}Na). This minimum value at low voltage range is possibly due to reduced recombination processes. Increasing the voltage further, deadtime increased rapidly to reach its maximum value at approximately 750 V for all three radioactive sources (22 µs for ^{204}Tl, 26 µs for ^{137}Cs, 9 µs for ^{22}Na). This behavior is mainly attributed to the on-set of gas multiplication processes. After the maximum deadtime value, an exponential decrease in deadtime was observed until a plateau was reached. This plateau region falls under the manufacturer's recommended region for the operation of the GM counter. This deadtime behavior was observed using three sources with the exception of ^{54}Mn source in which low count rates measured from ^{54}Mn resulted in negative deadtime values. Therefore, data collected using ^{54}Mn was not used for drawing a conclusion.

For the second part of this study, a detailed analysis of several pulse shape properties and their dependence on the operating voltage while investigating their correlation with detector deadtime were performed. The study's objective was to find a correlation between deadtime, pulse shape properties, and operating voltage. Since the GM region is of primary interest for many applications, the pulse shape correlation investigation focused on the high applied voltages.

It is observed that the recorded pulse shape properties follow a distinct pattern in relation to deadtime. "Positive Pulse Width" showed a strong negative correlation for all three sources (between -0.94 to -0.90) with operating voltage. However, a weaker correlation for the three sources was observed between deadtime and operating voltage (between -0.80 to -0.71). Therefore, it is inferred from the data that there is a positive correlation between "Positive Pulse Width" and deadtime.

Furthermore, a positive correlation between "Rise Time" and deadtime was observed. Also, "Fall time" showed a stronger negative correlation with the operating voltage (between -0.95 to -0.91) and a strong positive correlation with deadtime (between 0.95-0.94). Similar results were observed for "Cycle Mean," "Full Positive Pulse," and "Area" properties. The results from "Frequency" show a negative correlation with deadtime (between -0.79 to -0.86) and a strong positive correlation with the operating voltage (between 0.98 to 0.91). This is in agreement with the observation that as applied voltages increased, more counts are measured by the detector. This study confirmed that operating voltage and detector deadtime exhibit a strong correlation with several pulse shape properties.

Furthermore, the SiC study was divided into two parts. In the first part, computational reactor physics modeling using Monte Carlo N-Particle (MCNP), version 6.1, was performed. It was performed to investigate the neutronics of various accident tolerant nuclear fuel cladding candidates for high burnup application of the proposed low enriched uranium SMR core due to the increasing interest in SMRs worldwide. Therefore, this study selected a compact pressurized water reactor SMR core as a reference 2D 13X13 assembly. Uranium dioxide (UO2) was chosen as fuel for the compact SMR core with two different fissile enrichments: 15% and 19.9%. SiC and other alternative accident tolerant fuel (ATF) claddings (APMT, FeCrAl, SS-204, SS310) along with the traditional zircaloy claddings (Zr-2, Zr-4) were investigated in terms of discharge burnup. The burnup simulation results showed that SiC as an alternative ATF cladding material provides the highest achievable burnup as well as the maximum uranium utilization. This is due to the presence of carbon atoms, which provide additional moderation of neutrons; besides, the

lower thermal capture cross-sections of silicon. In addition, reactivity behavior was investigated by considering both discharge burnup penalty and gain. The results confirmed that SiC outperforms all other alternative cladding materials: Zr, FeCrAl, APMT, and SS. Therefore, SiC was chosen for further investigation as a potential ATF cladding for the high burnup SMR core application.

In the second part of the study, an experimental investigation to characterize SiC in terms of weight loss and mechanical strength was conducted. The 2 MW, light water-cooled, pool-type nuclear research reactor at the Rhode Island Nuclear Science center (RINSC) was utilized to irradiate SiC with neutrons in harsh environments (in pure steam at 1 atm at various applied high temperatures (120°C, 850°C to 1350°C). The experiments were conducted at the beam port. The flux at the beam port was determined to be 4.3E8 (neutrons/cm^2/s).

To draw useful conclusions, SiC samples were divided in three groups. As-received group which provided the base-line properties, while the second group (heat and steam exposure) provided property degradation in the absence of radiation. Finally, the third group of specimens were exposed to radiation in addition to steam and heat to mimic reactor environment. The weight loss experiment results showed that irradiated samples show a 2-10% higher weight loss per area than non-irradiated samples. Also, the results show that the material loss rate is more sensitive at higher temperatures and that irradiated specimens are more prone to weight loss. For the mechanical test, burst testing experiment was chosen to investigate SiC's strength. The results show that maximum internal pressure and fracture stress for non-irradiated and irradiated SiC specimens over the applied temperatures were comparable. Details of these results can be seen in Paper IV.

3. FUTURE WORKS

First, characterization of the SiC material included the following: (1) Scanning Electron Microscope, (2) Raman Spectroscopy, and (3) Electron Paramagnetic Resonance (EPR). Nevertheless, due to time constraint and my employee's (Kuwait Institute for Scientific Research, KISR) requirement to resume working physically in the State of Kuwait, the final results from these techniques were not included in this dissertation. Furthermore, the results need more in-depth analysis. Hence, a subsequent paper will be submitted after analyzing the results from these already completed studies.

The SEM was utilized to perform tests on 3 selected SiC specimens. The selection of SiC specimens considered (I) as-received samples, (II) non-irradiated samples for extreme cases (temperature of 850°C and 1300°C), and neutron-irradiated samples selected from the same temperature groups. The main purpose of utilizing SEM is to detect the presence of oxide films at the microstructural level in order to characterize the oxidation behavior.

Using different magnification scales, oxidation films on the control sample were not detected. This was performed on the control sample, which was not exposed to steam or heat, in order to compare the results with non-irradiated and irradiated samples (exposed to steam and heat). Nonetheless, crack and striation of the external SiC surface were observed, as shown in Figure 3.1a. The reason behind the striation pattern can be attributed to the extruding process while producing the SiC tubular specimen. Also, cracking on the SiC tube was observed which can be attributed to the burst testing experiment. Figure 3.1b shows that the bulk of the external surface of the tube reveals hierarchical porosity (nano- and microporosity) as well as microsized carbon inclusions with particular elongated

shape. Most of the residual porosity in the tube is observed along the grain boundaries and triple junctions indicating that the SiC is still not fully consolidated during processing. Also, it is seen that the SiC grains range in sizes between 5 to 20 microns. Nevertheless, the black spots observed in Figure 3.1b could be carbon inclusion and not porosity. Therefore, Raman Spectroscopy was needed to investigate the source of these spots. Furthermore, SEM was also utilized to investigate the internal surface of the SiC tube.
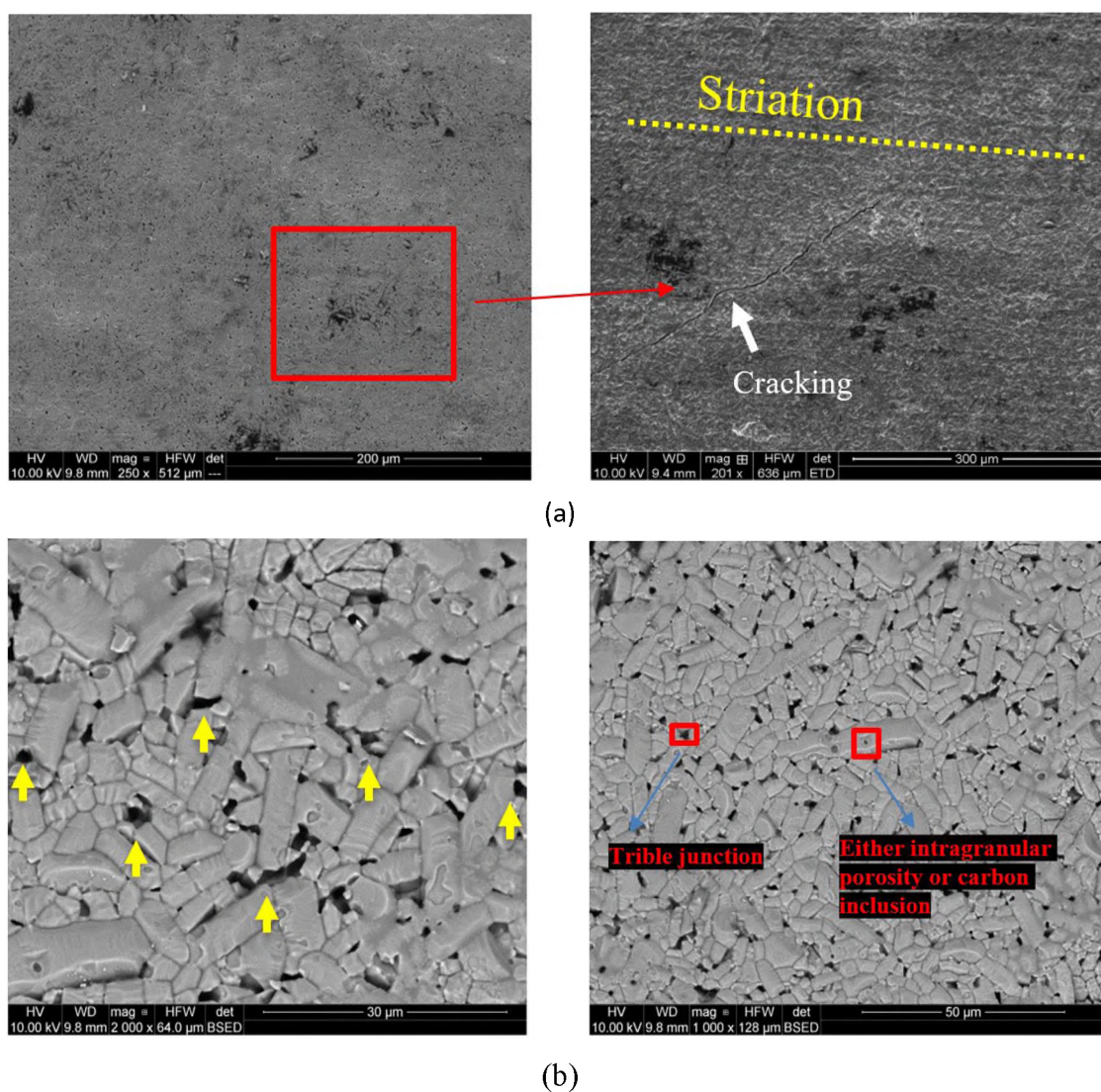
Figure 3.1. SEM images of the as-received SiC tubular sample: (a) the external surface of the SiC tube; (b) the internal surface of the specimen.

Figure 3.2a shows the inner surface of the SiC tube which has a significant amount of topographical texturing. This surface is comprised by a complex forest of micro-sized needle, plate, and tubular structures, as shown in Figure 3.2b. A comparison between the samples seems to show some difference in the roughness of the inner surface with temperature, although a more detailed analysis will be needed to assess that hypothesis.

(a)

(b)
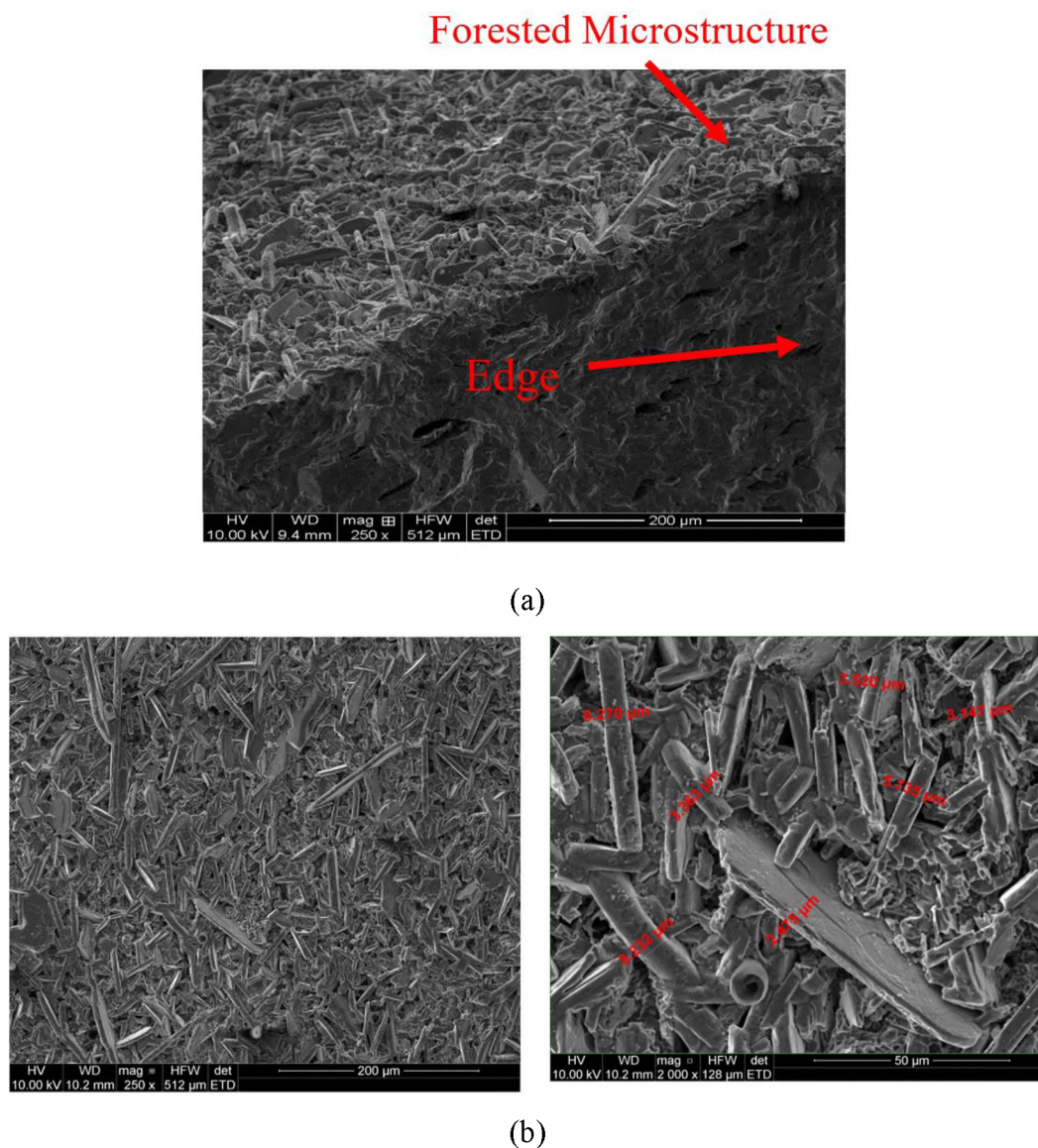
Figure 3.2. SEM images of as-received SiC tube sample: (a) topographical texturing along with edge; (b) a magnified SEM micrograph where needle, plate, and tubular structures are shown.

Figure 3.3 shows SEM results of the irradiated SiC sample at 1300°C using the polished cross section technique while Figure 3.4 shows non-irradiated sample. No significant changes between the samples were observed. An oxide phase was not present according to the BSEM micrographs. The reason behind this can be that the oxidation stage was still at an early stage and the oxide layer is beyond the resolution of the SEM (in the high magnifications X80000). Another reason for not detecting an oxide layer might be due to the accidental removal of the oxide layer while polishing the cross-section samples.
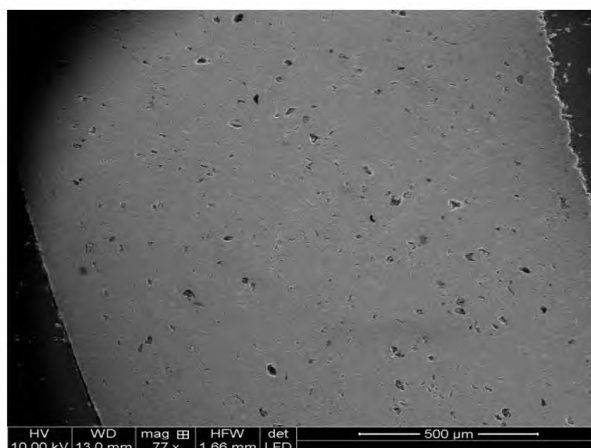
Figure 3.3. Edge SEM image of the neutron irradiated SiC external tube at 1300°C.
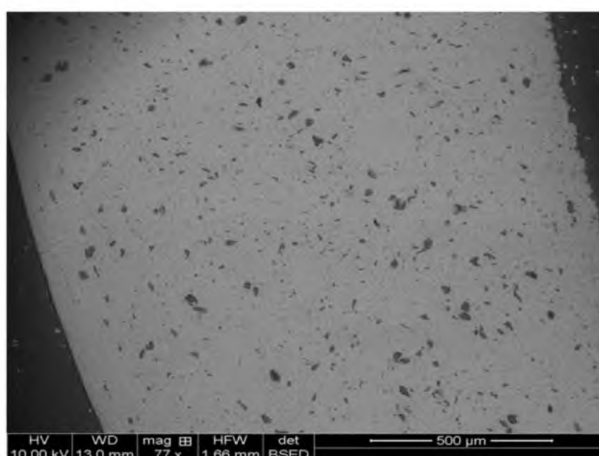
Figure 3.4. Edge SEM image of as-received SiC external tube.

Furthermore, analysis of the results obtained from the Raman Spectroscopy and EPR would provide supplementary information. The findings from SEM, Raman spectroscopy, and EPR will be reported to a peer reviewed journal by the end of this calendar year.

Second, to ensure the safety of the nuclear system, uncertainty quantification (UQ) is emphasized by the nuclear engineering community. A preliminary UQ assessment has been performed in order to understand the uncertainty of reactor core physics parameters and how it affects the core output parameters. In order to perform the task, a polynomial chaos method (PCM) of 3rd degree polynomial has been used for SiC and Zr (zircaloy-4) cladding candidates for the high burnup SMR core. Initially, two input uncertainties of the SMR core parameters have been considered to perform UQs: (1) cladding density, and (2) cladding thickness with 10% uncertainty. However, quantifying the 'combined' effect of uncertainties is essential in the nuclear system. It needs a large number of simulations for UQ and needs to be factored-in to improve the UQ methodology. Table 3.1 (as part of the preliminary assessment) shows the original input parameters for both SiC and Zr cladding candidates. In this calculation, new input parameters were generated by utilizing the 3rd degree order of PCM, which resulted in 16 new inputs, as shown in Table 3.2. The new input parameters were injected into MCNP to perform the new simulations. However, this UQ study is currently under investigation. It is expected that the outcome of this analysis will be reported to a peer-reviewed platform by the end of this calendar year.

Table 3.1. Input uncertainties for SiC and Zr-4 cases.

Parameters	Mean	Uncertainty
SiC Case		
Density	2.58	10%

Table 3.1. Input uncertainties for SiC and Zr-4 cases (cont.).

Parameters	Mean	Uncertainty
Thickness	0.655	10%
Parameters	**Mean**	**Uncertainty**
Zr-4 Case		
Density	6.56	10%
Thickness	0.655	10%

Table 3.2. The input densities and thicknesses for SiC and Zr-4 candidate claddings generated by the PCM.

SiC density	Zr-4 density	Cladding Thickness
2.3578	5.9951	0.0599
2.4923	6.337	0.0599
2.6677	6.783	0.0599
2.8022	7.1249	0.0599
2.3578	5.9951	0.0633
2.4923	6.337	0.0633
2.6677	6.783	0.0633
2.8022	7.1249	0.0633
2.3578	5.9951	0.0677
2.4923	6.337	0.0677
2.6677	6.783	0.0677
2.8022	7.1249	0.0677
2.3578	5.9951	0.0711
2.4923	6.337	0.0711
2.6677	6.783	0.0711
2.8022	7.1249	0.0711

APPENDIX A.

MATLAB CODE FOR DEADTIME MODELS

```matlab
% File input 1: launcher.m
clear all;
clc;

disp('Please the model you would like to run');
disp('Enter 1 for Non-Paralyzing Model');
disp('Enter 2 for Paralyzing Model');
disp('Enter 3 for Lee-Gardner - PN Model');
disp('Enter 4 for Lee-Gardner - NP Model');
disp('Enter 5 for Patil-Usman Model');
disp('Anything else will exit');

figure();
hold on
i = 1;
while i < 8
i = input('Model number: ');
if i == 1
[nonParalyzingni,nonParalyzingmi]  = nonParalyz();
elseif i == 2
[Paralyzingni,Paralyzingmi] = Paralyz();
elseif i == 3
[leeGardnerPnNi, leeGardnerPnMi] = LeeGardnerPN();
elseif i == 4
[leeGardnerNpNi, leeGardnerNpMi] = LeeGardnerNP();
elseif i == 5
[PatilUsmanni, PatilUsmanmi] = PatilUsman();
else
disp('Sorry, wrong model number, please try again');
end
end

% File input 2: launcher2.m
[nonParalyzNi, nonParalyzMi] = nonParalyz();
[paralyzNi, paralyzMi] = Paralyz();
[leeGardnerPnNi, leeGardnerPnMi] = LeeGardnerPN();
[leeGardnerNpNi, leeGardnerNpMi] = LeeGardnerNP();
[PatilUsmanNi, PatilUsmanMi] = PatilUsman();
```

```matlab
figure();
plot(leeGardnerNpNi, leeGardnerNpMi, leeGardnerPnNi, leeGardnerPnMi
    , nonParalyzNi, nonParalyzMi, paralyzNi, paralyzMi, PatilUsmanNi
    , PatilUsmanMi);

legend('NP', 'PN', 'Non Paralyzing', 'Paralyzing', 'AlmutairiUsman'
    , 'PatilUsman');
xlabel('True Count Rate');
ylabel('Measured Count Rate');

% File input 3: nonParalyz.m
function [ niRecord, miRecord ] = nonParalyz()
countRi = input('Enter the inital count rate (ct/s): ');
binSizeR = input('Enter the bin size (sec): ');
tnor = input('Enter the Non-Paralyzing Deadtime (sec): ');
tHalfR = input('Enter half life (sec): ');
lar = log(2)/tHalfR;  % Activity [1/sec]
ttr = tnor;
niRecord = [];
miRecord = [];
ttRecord = [];
excelOutput = [];
notFinished = 1;

while notFinished
% Initialize
ni = 1;
mi = 0;
tt = 0;

while tt < binSizeR
ramp = rand();  % Get a random number
deltaTr = -log(ramp)/countRi;
tt = tt + deltaTr;
ni = ni + 1;

if deltaTr > ttr
mi = mi + 1;
```

```matlab
ttr = tnor;
else
ttr = ttr-deltaTr;
end


end


niRecord = [niRecord, ni];
miRecord = [miRecord, mi];
ttRecord = [ttRecord, tt];
excelOutput = [excelOutput; ni, mi];
countRi = countRi * exp(-binSizeR * lar);
if ni < 15
notFinished = 0; % to finish and exist the loop after ni<15 counts
end


end % End of while loop


plot(niRecord, miRecord);
title('Non Paralyzing');
xlabel('True Count Rate');
ylabel('Measured Count Rate');
legend

%%%this section for saving the results in excel file in a specified
    folder%%%
filter = {'*.xlsx';'*.*'};
fullFileName = uiputfile(filter);
xlswrite(fullFileName , excelOutput);


end


% File input 4: Paralyz.m
function [ niRecord, miRecord ] = Paralyz( )
% Get input from user
CountRI = input('Enter the inital count rate (ct/s): ');
BinsizeR = input('Enter the bin size (sec): ');
paralyzDeadtime = input('Enter the Paralyzing Deadtime (sec): ');
```

```matlab
THALFR = input('Enter half life (sec): ');
lar = log(2)/THALFR;  % Activity [1/sec]
CCountR = CountRI;
paralyzedTimeRemaining = paralyzDeadtime;


excelOutput = [];
niRecord = [];
miRecord = [];
ttRecord = [];
notFinished = 1;


while notFinished


% Initialize
trueCounts = 1;
measCounts = 0;
t = 0;


while t < BinsizeR
% Compute how long it has been since the previous interaction
DeltaTR = -log(rand())/CCountR;
t = t + DeltaTR;
trueCounts = trueCounts + 1;
% Detector counts the event only if it is no longer paralyzed
if DeltaTR > paralyzedTimeRemaining
measCounts = measCounts + 1;
end


% Reset the detector dead time
paralyzedTimeRemaining = paralyzDeadtime;


end


niRecord = [niRecord, trueCounts];
miRecord = [miRecord, measCounts];
ttRecord = [ttRecord, t];
excelOutput = [excelOutput; trueCounts, measCounts];
% Compute the decay rate for the next timestep
```

```matlab
CCountR = CCountR * exp(-BinsizeR * lar);


if trueCounts < 15
notFinished = 0;
end


end % End of while loop


plot(niRecord, miRecord);
title('Paralyzing');
xlabel('True Count Rate');
ylabel('Measured Count Rate');
legend


%%%this section for saving the results in excel file in a specified
    folder%%%
filter = {'*.xlsx';'*.*'};
fullFileName = uiputfile(filter);
xlswrite(fullFileName , excelOutput);


end

% File input 5: LeeGardnerPN.m
function [ niRecord, miRecord ] = LeeGardnerPN( )
% Get input from user
CountRI = input('Enter the inital count rate (ct/s): ');
BinsizeR = input('Enter the bin size (sec): ');
TPOR = input('Enter the Original Paralyzing Deadtime (sec)');
TNOR = input('Enter the Original Non-Paralyzing Deadtime (sec)');
THALFR = input('Enter half life (sec): ');


lar = log(2)/THALFR;  % Activity [1/sec]
TPR=TPOR;
TNR=TNOR;
TTR = TNR + TPR;


excelOutput = [];
niRecord = [];
```

```matlab
miRecord = [];
ttRecord = [];
notFinished = 1;


while notFinished


% Initialize
NI = 1;
MI = 0;
tt = 0;


while tt < BinsizeR


ramp = rand();  % Get a random number
DeltaTR = -log(ramp)/CountRI;


tt = tt + DeltaTR;
NI = NI + 1;
TTR= TNR + TPR;


if DeltaTR < TPR
%MI = MI;
TPR = TPOR;
TNR = TNOR;
elseif DeltaTR < TTR
%MI=MI
TPR=0.0;
TNR = TNR - DeltaTR;


else
MI= MI+1;
TPR=TPOR;
TNR=TNOR;
end


end


niRecord = [niRecord, NI];
```

```matlab
miRecord = [miRecord, MI];
ttRecord = [ttRecord, tt];
excelOutput = [excelOutput; NI, MI];



CountRI = CountRI * exp(-BinsizeR * lar);
if NI < 15     % kill anything less than 15 counts
notFinished = 0;
end


end % End of while loop


plot(niRecord, miRecord);
title('Lee-Gardner PN');
xlabel('True Count Rate');
ylabel('Measured Count Rate');
legend

%%%this section for saving the results in excel file in a specified
    folder%%%
filter = {'*.xlsx';'*.*'};
fullFileName = uiputfile(filter);
xlswrite(fullFileName , excelOutput);


end

% File input 6: LeeGardnerNP.m
function [ niRecord, miRecord ] = LeeGardnerPN( )
% Get input from user
CountRI = input('Enter the inital count rate (ct/s): ');
BinsizeR = input('Enter the bin size (sec): ');
TPOR = input('Enter the Original Paralyzing Deadtime (sec)');
TNOR = input('Enter the Original Non-Paralyzing Deadtime (sec)');
THALFR = input('Enter half life (sec): ');


lar = log(2)/THALFR;  % Activity [1/sec]
TPR=TPOR;
TNR=TNOR;
```

```matlab
TTR = TNR + TPR;


excelOutput = [];
niRecord = [];
miRecord = [];
ttRecord = [];


notFinished = 1;


while notFinished


% Initialize
NI = 1;
MI = 0;
tt = 0;


while tt < BinsizeR


ramp = rand();   % Get a random number
DeltaTR = -log(ramp)/CountRI;


tt = tt + DeltaTR;
NI = NI + 1;
TTR= TNR + TPR;


if DeltaTR < TPR
%MI = MI;
TPR = TPOR;
TNR = TNOR;
elseif DeltaTR < TTR
%MI=MI
TPR=0.0;
TNR = TNR - DeltaTR;


else
MI= MI+1;
TPR=TPOR;
TNR=TNOR;
```

```matlab
        end


    end


    niRecord = [niRecord, NI];
    miRecord = [miRecord, MI];
    ttRecord = [ttRecord, tt];
    excelOutput = [excelOutput; NI, MI];


    CountRI = CountRI * exp(-BinsizeR * lar);
    if NI < 15      % kill anything less than 15 counts
    notFinished = 0;
    end


end % End of while loop


plot(niRecord, miRecord);
title('Lee-Gardner PN');
xlabel('True Count Rate');
ylabel('Measured Count Rate');
legend

%%%this section for saving the results in excel file in a specified
    folder%%%
filter = {'*.xlsx';'*.*'};
fullFileName = uiputfile(filter);
xlswrite(fullFileName , excelOutput);


end

% File input 7: PatilUsman.m
function [ niRecord, miRecord ] = PatilUsman( )
% Get input from user
CountRI = input('Enter the inital count rate (ct/s): ');
BinsizeR = input('Enter the bin size (sec): ');
TPOR = input('Enter the Paralyzing Deadtime (sec): ');
TNOR = input('Enter the Non-Paralyzing Deadtime (sec): ');
THALFR = input('Enter half life (sec): ');
```

```matlab
PFR = input('Enter the PFR (between 0 and 1): '); % paralysis
    factor
lar = log(2)/THALFR;   % Activity [1/sec]
CCountR = CountRI;   % This is pointless
TTOR= TPOR + TNOR;
TTR = TTOR;
PFR=0.50;        % this is paralysis factor can be changed, in this
    case its 50%

excelOutput = [];
niRecord = [];
miRecord = [];
ttRecord = [];
notFinished = 1;

while notFinished
% Initialize
NI = 1;
MI = 0;
tt = 0;

while tt < BinsizeR
ramp = rand();  % Get a random number
DeltaTR = -log(ramp)/CCountR;
tt = tt + DeltaTR;
NI = NI + 1;
if DeltaTR > TTR
MI = MI + 1;
TTR=TTOR;
else
if ramp > PFR
TTR = TTR - DeltaTR;
else
TTR=TTOR;
end

end
```

```matlab
end


niRecord = [niRecord, NI];
miRecord = [miRecord, MI];
ttRecord = [ttRecord, tt];
excelOutput = [excelOutput; NI, MI];


CCountR = CCountR * exp(-BinsizeR * lar);
if NI < 15
notFinished = 0;
end


end % End of while loop

plot(niRecord, miRecord);
title('Patil Usman');
xlabel('True Count Rate');
ylabel('Measured Count Rate');
legend

%%%this section for saving the results in excel file in a specified
    folder%%%
filter = {'*.xlsx';'*.*'};
fullFileName = uiputfile(filter);
xlswrite(fullFileName , excelOutput);


end
```

APPENDIX B.

MCNP CODE FOR SIC NEUTRONICS

1. MCNP 6 CODE TO CALCULATE K∞ AND DISCHARGE BURNUP

The following sections 1.1 and 1.2 includes MCNP 6.1 sample input codes. The sample codes shown below are only for SiC cladding material. Same input codes were used for other cladding materials; however, the density is changed along with associated material's card for the cladding. In addition, to assign different enrichment, such as 19.9%, the material's card for the nuclear fuel is changed. The same approach is followed for calculating flux at beginning of life (BOL).

1.1 CODE FOR SIC CLADDING MATERIAL WITH 15% ENRICHMENT

```
set title "Burnup for SMR-15% Enrichment"
c Cell Cards
c ------------------------------------------------------------------------------
c The next cells defines pin G
1       1 -0.707      -1          u=1 imp:n=1              $ Water
2       2 -6.88547    1 -2        u=1 imp:n=1              $ cladGT
3       1 -0.707      2           u=1 imp:n=1              $ Water
c The next cells defines pin U
4       3 -9.619      -3          u=2 imp:n=1 vol=94.3     $ Fuel
5       4 -2.58       3 -4        u=2 imp:n=1 vol=32.58    $ cladF of SiC
6       5 -7.08208    4 -5        u=2 imp:n=1              $ cladCrsn
7       1 -0.707      5           u=2 imp:n=1              $ Water
c The next cells defines pin I
8       1 -0.707      -6          u=3 imp:n=1              $ Water
9       6 -6.56       6 -7        u=3 imp:n=1              $ cladI Zr
10      2 -6.88547    7 -8        u=3 imp:n=1              $ cladGT
11      1 -0.707      8           u=3 imp:n=1              $ Water
c ------------------------------------------------------------------------------
50      1 -0.707      -20         u=4  imp:n=1             $ water
12      0 -9 10 -11 12 u=12  imp:n=1 lat=1 fill=-7:7 -7:7 0:0   $ square lattice-pin
                4 4 4 4 4 4 4 4 4 4 4 4 4 4 4
                4 2 2 2 2 2 2 2 2 2 2 2 2 2 4
                4 2 2 2 2 2 2 1 2 2 2 2 2 2 4
                4 2 2 1 2 2 2 2 2 2 2 1 2 2 4
                4 2 2 2 2 2 2 2 2 2 2 2 2 2 4
                4 2 2 2 2 1 2 1 2 1 2 2 2 2 4
                4 2 2 2 2 2 2 2 2 2 2 2 2 2 4
```

```
              4 2 1 2 2 1 2 3 2 1 2 2 1 2 4
              4 2 2 2 2 2 2 2 2 2 2 2 2 2 4
              4 2 2 2 2 1 2 1 2 1 2 2 2 2 4
              4 2 2 2 2 2 2 2 2 2 2 2 2 2 4
              4 2 2 1 2 2 2 2 2 2 2 1 2 2 4
              4 2 2 2 2 2 2 1 2 2 2 2 2 2 4
              4 2 2 2 2 2 2 2 2 2 2 2 2 2 4
              4 4 4 4 4 4 4 4 4 4 4 4 4 4 4
13     0   -13 14 -15 16 80 -90      imp:n=1 fill=12        $ square assembly
15     0   #13                       imp:n=0                $ outside world
```

c --

c surface cards

1	cz	0.433	
2	cz	0.612	
3	cz	0.4095	
4	cz	0.475	
5	cz	0.476638	
6	cz	0.572	
7	cz	0.612	
8	cz	0.617179	
9	px	0.632675	$ 1st side of the square lattice
10	px	-0.632675	$ 2nd side of the square lattice
11	py	0.632675	$ 3rd side of the square lattice
12	py	-0.632675	$ 4th side of the square lattice
*13	px	8.266775	$ 1st side of the square assembly
*14	px	-8.266775	$ 2nd side of the square assembly
*15	py	8.266775	$ 3rd side of the square assembly
*16	py	-8.266775	$ 4th side of the square assembly
*80	pz	-89.5	$ Bottom of half-core
*90	pz	89.5	$ Top of half-core
20	cz	100	

c --

c Data Cards

burn time= 10 40 50 100 200r

    mat=3 power=2.976 pfrac=1.0 203r bopt=1.0 -24 -1 $ Tier 3 Burnup

    omit=3 4 6014 7016 8018 9018

    matvol=14333.567

c Materials

m1	1001.53c-0.1119		$ water @ 600K
	8016.53c	-0.8881	$ water @ 600K
mt1	lwtr.16t		$ Thermal scattering

c cladGT @ 600K ENDF/B-VII.1

m2	26056.81c	-0.5756	$ Fe
	24052.81c	-0.1895	$ Cr-52
	28058.81c	-0.2244	$ Ni-58
	25055.81c	-0.006	$ Mn-55

```
            14028.81c   -0.0045           $ Si 28
m3   92235.82c      -0.13077          $ Fuel @ 900K "2006"
         92238.82c      -0.75051          $ Fuel @ 900K "2006"
         8016.82c      -0.11872          $ Fuel @ 900K "2011"
c cladF @ 600K ENDF/B-VII.1
m4   14028.81c   -0.7008             $ Si
         6000.81c   -0.2992             $ C
c cladCrsn @ 600K ENDF/B-VII.1
m5   26056.81c      -0.203            $ Fe
         24052.81c   -0.203            $ Cr-52
         28058.81c   -0.594            $ Ni-58
c cladI @ 600K ENDF/B-VII.1
m6   40090.81c      -1               $ Zr
kcode 5000 1.0 50 250                $ Criticality card
ksrc   1.3 0 0                       $ source in the fuel
```

1.2.   MCNP 6 Code for SiC cladding material to calculate Flux at BOL

```
set title "Flux for SMR-15% Enrichment"
c Cell Cards
c -------------------------------------------------------------------
c The next cells defines pin G
1       1 -0.707       -1         u=1 imp:n=1          $ Water
2       2 -6.88547     1 -2       u=1 imp:n=1          $ cladGT
3       1 -0.707       2          u=1 imp:n=1          $ Water
c The next cells defines pin U
4       3 -9.619       -3         u=2 imp:n=1 vol=94.3   $ Fuel
5       4 -2.58        3 -4       u=2 imp:n=1 vol=32.58  $ cladF of APMT
6       5 -7.08208     4 -5       u=2 imp:n=1          $ cladCrsn
7       1 -0.707       5          u=2 imp:n=1          $ Water
c The next cells defines pin I
8       1 -0.707       -6         u=3 imp:n=1          $ Water
9       6 -6.56        6 -7       u=3 imp:n=1          $ cladI Zr
10      2 -6.88547     7 -8       u=3 imp:n=1          $ cladGT
11      1 -0.707       8          u=3 imp:n=1          $ Water
c -------------------------------------------------------------------
50      1 -0.707       -20        u=4 imp:n=1          $ water
12      0 -9 10 -11 12 u=12  imp:n=1 lat=1 fill=-7:7 -7:7 0:0    $ square lattice-pin
            4 4 4 4 4 4 4 4 4 4 4 4 4 4 4
            4 2 2 2 2 2 2 2 2 2 2 2 2 2 4
            4 2 2 2 2 2 2 1 2 2 2 2 2 2 4
            4 2 2 1 2 2 2 2 2 2 2 1 2 2 4
            4 2 2 2 2 2 2 2 2 2 2 2 2 2 4
            4 2 2 2 2 1 2 1 2 1 2 2 2 2 4
            4 2 2 2 2 2 2 2 2 2 2 2 2 2 4
            4 2 1 2 2 1 2 3 2 1 2 2 1 2 4
```

```
            4 2 2 2 2 2 2 2 2 2 2 2 2 2 4
            4 2 2 2 2 1 2 1 2 1 2 2 2 2 4
            4 2 2 2 2 2 2 2 2 2 2 2 2 2 4
            4 2 2 1 2 2 2 2 2 2 2 1 2 2 4
            4 2 2 2 2 2 2 1 2 2 2 2 2 2 4
            4 2 2 2 2 2 2 2 2 2 2 2 2 2 4
            4 4 4 4 4 4 4 4 4 4 4 4 4 4 4
13      0   -13 14 -15 16 80 -90       imp:n=1 fill=12       $ square assembly
15      0   #13                        imp:n=0               $ outside world
```

c --
c surface cards

```
1            cz      0.433
2            cz      0.612
3            cz      0.4095
4            cz      0.475
5            cz      0.476638
6            cz      0.572
7            cz      0.612
8            cz      0.617179
9            px      0.632675         $ 1st side of the square lattice
10           px     -0.632675         $ 2nd side of the square lattice
11           py      0.632675         $ 3rd side of the square lattice
12           py     -0.632675         $ 4th side of the square lattice
*13   px     8.266775                 $ 1st side of the square assembly
*14   px    -8.266775                 $ 2nd side of the square assembly
*15   py     8.266775                 $ 3rd side of the square assembly
*16   py    -8.266775                 $ 4th side of the square assembly
*80   pz    -89.5                     $ Bottom of half-core
*90   pz     89.5                     $ Top of half-core
20           cz      100
```

c --

c Data Cards
c Materials

```
m1    1001.53c-0.1119                 $ water @ 600K
         8016.53c    -0.8881          $ water @ 600K
mt1  lwtr.16t                         $ Thermal
c cladGT @ 600K ENDF/B-VII.1
m2    26056.81c     -0.5756           $ Fe
         24052.81c   -0.1895          $ Cr-52
         28058.81c   -0.2244          $ Ni-58
         25055.81c   -0.006           $ Mn-55
         14028.81c   -0.0045          $ Si 28
m3    92235.82c     -0.13077          $ Fuel @ 900K "2006"
         92238.82c   -0.75051         $ Fuel @ 900K "2006"
         8016.82c    -0.11872         $ Fuel @ 900K "2011"
c cladF @ 600K ENDF/B-VII.1
```

```
m4    14028.81c    -0.7008                          $ Si
      6000.81c     -0.2992                          $ C
c cladCrsn @ 600K ENDF/B-VII.1
m5    26056.81c        -0.203                        $ Fe
      24052.81c    -0.203                            $ Cr-52
      28058.81c    -0.594                            $ Ni-58
c cladI @ 600K ENDF/B-VII.1
m6    40090.81c        -1                            $ Zr
kcode 10000 1.0 100 350
ksrc    1.3 0 0                                      $ Initial source in the fuel
c -----------------------------------------------------------------------------
f4:n 4                                               $ Flux avg. over cell 4
E0      1.00000e-9 1.05925e-9 1.12202e-9 1.18850e-9 1.25893e-9 &
        1.33352e-9 1.41254e-9 1.49624e-9 1.58489e-9 1.67880e-9 &
        1.77828e-9 1.88365e-9 1.99526e-9 2.11349e-9 2.23872e-9 &
        2.37137e-9 2.51189e-9 2.66073e-9 2.81838e-9 2.98538e-9 &
        3.16228e-9 3.34965e-9 3.54813e-9 3.75837e-9 3.98107e-9 &
        4.21697e-9 4.46684e-9 4.73151e-9 5.01187e-9 5.30884e-9 &
        5.62341e-9 5.95662e-9 6.30957e-9 6.68344e-9 7.07946e-9 &
        7.49894e-9 7.94328e-9 8.41395e-9 8.91251e-9 9.44061e-9 &
        1.00000e-8 1.05925e-8 1.12202e-8 1.18850e-8 1.25893e-8 &
        1.33352e-8 1.41254e-8 1.49624e-8 1.58489e-8 1.67880e-8 &
        1.77828e-8 1.88365e-8 1.99526e-8 2.11349e-8 2.23872e-8 &
        2.37137e-8 2.51189e-8 2.66073e-8 2.81838e-8 2.98538e-8 &
        3.16228e-8 3.34965e-8 3.54813e-8 3.75837e-8 3.98107e-8 &
        4.21697e-8 4.46684e-8 4.73151e-8 5.01187e-8 5.30884e-8 &
        5.62341e-8 5.95662e-8 6.30957e-8 6.68344e-8 7.07946e-8 &
        7.49894e-8 7.94328e-8 8.41395e-8 8.91251e-8 9.44061e-8 &
        1.00000e-7 1.05925e-7 1.12202e-7 1.18850e-7 1.25893e-7 &
        1.33352e-7 1.41254e-7 1.49624e-7 1.58489e-7 1.67880e-7 &
        1.77828e-7 1.88365e-7 1.99526e-7 2.11349e-7 2.23872e-7 &
        2.37137e-7 2.51189e-7 2.66073e-7 2.81838e-7 2.98538e-7 &
        3.16228e-7 3.34965e-7 3.54813e-7 3.75837e-7 3.98107e-7 &
        4.21697e-7 4.46684e-7 4.73151e-7 5.01187e-7 5.30884e-7 &
        5.62341e-7 5.95662e-7 6.30957e-7 6.68344e-7 7.07946e-7 &
        7.49894e-7 7.94328e-7 8.41395e-7 8.91251e-7 9.44061e-7 &
        1.00000e-6 1.05925e-6 1.12202e-6 1.18850e-6 1.25893e-6 &
        1.33352e-6 1.41254e-6 1.49624e-6 1.58489e-6 1.67880e-6 &
        1.77828e-6 1.88365e-6 1.99526e-6 2.11349e-6 2.23872e-6 &
        2.37137e-6 2.51189e-6 2.66073e-6 2.81838e-6 2.98538e-6 &
        3.16228e-6 3.34965e-6 3.54813e-6 3.75837e-6 3.98107e-6 &
        4.21697e-6 4.46684e-6 4.73151e-6 5.01187e-6 5.30884e-6 &
        5.62341e-6 5.95662e-6 6.30957e-6 6.68344e-6 7.07946e-6 &
        7.49894e-6 7.94328e-6 8.41395e-6 8.91251e-6 9.44061e-6 &
        1.00000e-5 1.05925e-5 1.12202e-5 1.18850e-5 1.25893e-5 &
        1.33352e-5 1.41254e-5 1.49624e-5 1.58489e-5 1.67880e-5 &
```

1.77828e-5 1.88365e-5 1.99526e-5 2.11349e-5 2.23872e-5 &
2.37137e-5 2.51189e-5 2.66073e-5 2.81838e-5 2.98538e-5 &
3.16228e-5 3.34965e-5 3.54813e-5 3.75837e-5 3.98107e-5 &
4.21697e-5 4.46684e-5 4.73151e-5 5.01187e-5 5.30884e-5 &
5.62341e-5 5.95662e-5 6.30957e-5 6.68344e-5 7.07946e-5 &
7.49894e-5 7.94328e-5 8.41395e-5 8.91251e-5 9.44061e-5 &
1.00000e-4 1.05925e-4 1.12202e-4 1.18850e-4 1.25893e-4 &
1.33352e-4 1.41254e-4 1.49624e-4 1.58489e-4 1.67880e-4 &
1.77828e-4 1.88365e-4 1.99526e-4 2.11349e-4 2.23872e-4 &
2.37137e-4 2.51189e-4 2.66073e-4 2.81838e-4 2.98538e-4 &
3.16228e-4 3.34965e-4 3.54813e-4 3.75837e-4 3.98107e-4 &
4.21697e-4 4.46684e-4 4.73151e-4 5.01187e-4 5.30884e-4 &
5.62341e-4 5.95662e-4 6.30957e-4 6.68344e-4 7.07946e-4 &
7.49894e-4 7.94328e-4 8.41395e-4 8.91251e-4 9.44061e-4 &
1.00000e-3 1.05925e-3 1.12202e-3 1.18850e-3 1.25893e-3 &
1.33352e-3 1.41254e-3 1.49624e-3 1.58489e-3 1.67880e-3 &
1.77828e-3 1.88365e-3 1.99526e-3 2.11349e-3 2.23872e-3 &
2.37137e-3 2.51189e-3 2.66073e-3 2.81838e-3 2.98538e-3 &
3.16228e-3 3.34965e-3 3.54813e-3 3.75837e-3 3.98107e-3 &
4.21697e-3 4.46684e-3 4.73151e-3 5.01187e-3 5.30884e-3 &
5.62341e-3 5.95662e-3 6.30957e-3 6.68344e-3 7.07946e-3 &
7.49894e-3 7.94328e-3 8.41395e-3 8.91251e-3 9.44061e-3 &
1.00000e-2 1.05925e-2 1.12202e-2 1.18850e-2 1.25893e-2 &
1.33352e-2 1.41254e-2 1.49624e-2 1.58489e-2 1.67880e-2 &
1.77828e-2 1.88365e-2 1.99526e-2 2.11349e-2 2.23872e-2 &
2.37137e-2 2.51189e-2 2.66073e-2 2.81838e-2 2.98538e-2 &
3.16228e-2 3.34965e-2 3.54813e-2 3.75837e-2 3.98107e-2 &
4.21697e-2 4.46684e-2 4.73151e-2 5.01187e-2 5.30884e-2 &
5.62341e-2 5.95662e-2 6.30957e-2 6.68344e-2 7.07946e-2 &
7.49894e-2 7.94328e-2 8.41395e-2 8.91251e-2 9.44061e-2 &
1.00000e-1 1.05925e-1 1.12202e-1 1.18850e-1 1.25893e-1 &
1.33352e-1 1.41254e-1 1.49624e-1 1.58489e-1 1.67880e-1 &
1.77828e-1 1.88365e-1 1.99526e-1 2.11349e-1 2.23872e-1 &
2.37137e-1 2.51189e-1 2.66073e-1 2.81838e-1 2.98538e-1 &
3.16228e-1 3.34965e-1 3.54813e-1 3.75837e-1 3.98107e-1 &
4.21697e-1 4.46684e-1 4.73151e-1 5.01187e-1 5.30884e-1 &
5.62341e-1 5.95662e-1 6.30957e-1 6.68344e-1 7.07946e-1 &
7.49894e-1 7.94328e-1 8.41395e-1 8.91251e-1 9.44061e-1 &
1.00000e+0 1.05925e+0 1.12202e+0 1.18850e+0 1.25893e+0 &
1.33352e+0 1.41254e+0 1.49624e+0 1.58489e+0 1.67880e+0 &
1.77828e+0 1.88365e+0 1.99526e+0 2.11349e+0 2.23872e+0 &
2.37137e+0 2.51189e+0 2.66073e+0 2.81838e+0 2.98538e+0 &
3.16228e+0 3.34965e+0 3.54813e+0 3.75837e+0 3.98107e+0 &
4.21697e+0 4.46684e+0 4.73151e+0 5.01187e+0 5.30884e+0 &
5.62341e+0 5.95662e+0 6.30957e+0 6.68344e+0 7.07946e+0 &
7.49894e+0 7.94328e+0 8.41395e+0 8.91251e+0 9.44061e+0 &

1.00000e+1 1.05925e+1 1.12202e+1 1.18850e+1 1.25893e+1 &
1.33352e+1 1.41254e+1 1.49624e+1 1.58489e+1 1.67880e+1 &
1.77828e+1 1.88365e+1 2.00000e+1

APPENDIX C.

PYTHON CODE FOR EXTRACTING OUTPUT RESULTS

```python
import pandas as pd
import numpy as np
import re
import tkinter as tk
from tkinter import filedialog
root = tk.Tk()
root.withdraw()


# open browser using tkinter to choose your output file
x = filedialog.askopenfilename()


# find table start patterns
pattern = re.compile("step duration time power keff flux ave.nu ave
    .q burnup source")
start_lines = []
for i, line in enumerate(open(x)):
for match in re.finditer(pattern, line):
start_lines.append(i+1)
  print ('Found on line %s: %s' % (i+1, match.group()))


# find table end patterns
pattern = re.compile("nuclide data are sorted by increasing zaid
    for material")
end_lines = []
for i, line in enumerate(open(x)):
for match in re.finditer(pattern, line):
end_lines.append(i+1)
  print ('Found on line %s: %s' % (i+1, match.group()))


# This will extract the final table in the output file
start_line = start_lines[-1]
end_line = end_lines[-1]


# lines containing the table
lineArray = np.arange(start_line, end_line)
```

```python
import pandas as pd
import numpy as np
import re
import tkinter as tk
from tkinter import filedialog
root = tk.Tk()
root.withdraw()


# open browser using tkinter to choose your output file
x = filedialog.askopenfilename()


# find table start patterns
pattern = re.compile("step duration time power keff flux ave.nu ave
    .q burnup source")
start_lines = []
for i, line in enumerate(open(x)):
for match in re.finditer(pattern, line):
start_lines.append(i+1)
  print ('Found on line %s: %s' % (i+1, match.group()))


# find table end patterns
pattern = re.compile("nuclide data are sorted by increasing zaid
    for material")
end_lines = []
for i, line in enumerate(open(x)):
for match in re.finditer(pattern, line):
end_lines.append(i+1)
  print ('Found on line %s: %s' % (i+1, match.group()))


# This will extract the final table in the output file
start_line = start_lines[-1]
end_line = end_lines[-1]


# lines containing the table
lineArray = np.arange(start_line, end_line)
```

```python
# Save the results in a text file
y =  filedialog.asksaveasfilename(initialdir = "/",title = "Select
    file",filetypes = (("text files","*.txt"),("all files","*.*")))


# save the table
with open(y, 'w') as output:
fp = open(x)
for i, line in enumerate(fp):
if i >= start_line-1 and i<end_line-2:
print(line)
output.write(line)
print('Job is done. Please, check your results \n')


fin = open(y, "r+")
data= fin.read()
data= data.replace('step duration time power keff flux ave.nu ave.q
        burnup source', 'Step Duration Time Power keff Flux ave.N
    ave.Q Burnup Source')


data= data.replace('(days)(days)(MW)(GWd/MTU)(nts/sec)', 'Days Days
    MW(GWd/MTU)(nts/sec)')
if data:
print('The job is done \n')
else:
print('error ocurred \n')
fin.close()


# save headers replacements by overwriting the same text file
fin= open(y, 'wt')


# overwrite the final data and close file.
fin.write(data)
fin.close()
```

BIBLIOGRAPHY

[1]   Knoll, G.F. Radiation Detection and Measurement. (John Willey & Sons, Ltd, 2010).

[2]   Muller, J.W. Dead-time problems. Nucl. Instrum. Methods 112, 47-57 (1973).

[3]   J. C. May, D.H. J. Russell, A Mass-Selective Variable-Temperature Drift Tube Ion Mobility-Mass Spectrometer for Temperature Dependent Ion Mobility Studies, Journal of the American Society for Mass Spectrometry. 22 (2011) 1134-1145.

[4]   Usman, S., Patil, A. Radiation detector deadtime and pile up: A review of the status of science, Nucl. Eng. Tec. 50, 1006-1016 (2008).

[5]   Feller, W. On probability problems in the theory of counters. In: R. Courant Anniversary Volume, Studies and Essays. Interscience, New York, 105-115, (1948).

[6]   Evans, R. D. The Atomic Nucleus, McGraw-Hill, New York, (1955).

[7]   Muller, J.W. A simple derivation of the Takacs formula. (Bureau International des Poids et Mesures, 1988).

[8]   Muller, J.W. Generalized dead times, Nucl. Instrum. Methods Phys. Res. Sect. A Accel. Spectrom. Detect. Assoc. Equip. 301, 543-551 (1991).

[9]   Albert, G.E., Nelson, L. Contributions to the statistical theory of counter data, Ann. Math. Stat. 24, 9-22 (1953).

[10]   Lee, S.H., Gardner, R.P. A new G-M counter dead time model, Appl. Radiat. Isot. 53, 731-737 (2000).

[11]   Terrani, K. A. Accident tolerant fuel cladding development: Promise, status, and challenges. Journal of Nuclear Materials 501, 13–30 (2018).

[12]   Andrews, N., Pilat, E., Shirvan, K. & Kazimi, M. Impact of SiC cladding on plutonium burning in a thorium fueled PWR. In Proc. ICAPP 2014, Charlotte, USA (2014).

[13]   Pint, B. A., Terrani, K. A., Yamamoto, Y. & Snead, L. L. Material selection for accident tolerant fuel cladding. Metallurgical and Materials Transactions E 2, 190-196 (2015).

[14] Lee, Y. et al. Oxidation behavior of sintered tubular silicon carbide in pure steam I: Experiments. Ceramics International 42, 1916–1925 (2016).

[15] Lee, Y., McKrell, T. J. & Kazimi, M. S. Oxidation behavior of sintered tubular silicon carbide in pure steam II: Weight-loss correlation developments. Ceramics International 42, 4679–4689 (2016).

[16] Sukjai, Y. Silicon carbide performance as cladding for advanced uranium and thorium fuels for light water reactors. Ph.D. thesis, Massachusetts Institute of Technology (2014).

[17] Li, S. et al. Microstructural evolution of coating-modified 3D C/SiC composites after annealing in wet oxygen at different temperatures. Corrosion Science 52, 2837–2845 (2010).

[18] Qiang, X. et al. A modified dual-layer SiC oxidation protective coating for carbon/carbon composites prepared by one-step pack cementation. Corrosion Science 53, 523–527 (2011).

[19] Hou, X.-m. & Chou, K.-C. A simple model for the oxidation of carbon-containing composites. Corrosion Science 52, 1093–1097 (2010).

[20] Yao, R., Feng, Z., Chen, L., Zhang, Y. & Zhang, B. Oxidation behavior of hi-nicalon SiC monofilament fibres in air and o2–h2o–ar atmospheres. Corrosion Science 57, 182–191 (2012).

[21] Yang, X. et al. Resistance to oxidation and ablation of SiC coating on graphite prepared by chemical vapor reaction. Corrosion Science 75, 16–27 (2013).

[22] Charpentier, L., Dawi, K., Balat-Pichelin, M., B^eche, E. & Audubert, F. Chemical degradation of SiC/SiC composite for the cladding of gas-cooled fast reactor in case of severe accident scenarios. Corrosion Science 59, 127–135 (2012).

[23] Narushima, T., Goto, T., Hirai, T. & Iguchi, Y. High-temperature oxidation of silicon carbide and silicon nitride. Materials transactions, JIM 38, 821–835 (1997).

[24] Tortorelli, P. F. & More, K. L. Effects of high water-vapor pressure on oxidation of silicon carbide at 1200Âř c. Journal of the American Ceramic Society 86, 1249–1255 (2003).

[25]   Opila, E. J. & Hann Jr, R. E. Paralinear oxidation of CVD SiC in water vapor. Journal of the American Ceramic Society 80, 197–205 (1997).

[26]   Opila, E. J. Volatility of common protective oxides in high-temperature water vapor: current understanding and unanswered questions. In Materials Science Forum, vol. 461, 765–774 (Trans Tech Publ, 2004).

[27]   Terrani, K. A. et al. Silicon carbide oxidation in steam up to 2 MPa. Journal of the American Ceramic Society 97, 2331–2352 (2014).

[28]   MacDonald, P. & Lee, C. Use of thoria-urania fuels in PWRs: A general review of a NERI project to assess feasible core designs, economics, fabrication methods, in-pile thermal/mechanical behavior, and waste form characteristics. Nucl. Technol. 147, 1–7 (2004).

[29]   Alam, S. B. et al. Small modular reactor core design for civil marine propulsion using micro-heterogeneous duplex fuel. Part I: Assembly-level analysis. Nucl Eng Des. 346, 157–175 (2019).

[30]   Alam, S. B. et al. Small modular reactor core design for civil marine propulsion using micro-heterogeneous duplex fuel. Part II: Whole-core analysis. Nucl Eng Des. 346, 176–191 (2019).

[31]   Peakman, A., Owen, H. & Abram, T. The core design of a small modular pressurised water reactor for commercial marine propulsion. Progress in Nuclear Energy 113, 175–185 (2019).

[32]   Alam, S. B. The Design of Reactor Cores for Civil Nuclear Marine Propulsion. Ph.D. thesis, University of Cambridge, Cambridge, UK (2018).

VITA

Bader Almutairi was born in the State of Kuwait. He received, in 2017, his Bachelor of Science in Environmental Science from California State University, Fresno, CA, USA. In 2012, he received his master's degree in Biomedical Engineering from Rheinisch-Westfälische Technische Hochschule Aachen, Germany. In 2013, Bader started working at the Kuwait Institute of Scientific Research (KISR) for two and a half years as a Research Associate. In 2015, his employer offered him a scholarship to pursue a higher degree in the USA. Since August 2015, Bader Almutairi has been enrolled in the Ph.D. program at Missouri University of Science and Technology.

In 2017, Bader earned his master's degree in Nuclear Engineering from Missouri University of Science and Technology. While enrolled in the Ph.D. in nuclear engineering in Summer of 2017, Bader earned a graduate fellowship award for Nuclear Non-Proliferation Education and Research Center at the Korea Advanced Institute of Science and Technology, Daejeon, South Korea, that took place from July 2017 to August 2017 (Awarded out of 30 Graduate Fellows from 16 countries). In May 2018, Bader joined the Rhode Island Nuclear Science Center (RINSC), RI, USA, to work on his Ph.D. research, which included two areas of research: (1) deadtime experimental evaluation and SiC modeling and characterization. In summer 2018, Bader received a graduate fellowship award For MeV summer school at Argonne National Laboratory, Lemont, IL, USA. In Summer 2019, Bader received a graduate fellowship award For MeV summer school at Oak Ridge National Laboratory, Tn, USA.

In August 2020, he earned his Ph.D. in Nuclear Engineering from Missouri University of Science and Technology, Rolla, USA.